Semi-Analytical Composite Oval Fuselage Mass Estimation

M.N. Roelofs

Registration number: 082#16#MT#FPP
5 July 2016

TU Delft

Source cover image: Airbus

Semi-Analytical Composite Oval Fuselage Mass Estimation

by

M.N. Roelofs

to obtain the degree of Master of Science
at the Delft University of Technology,
to be defended publicly on Tuesday August 9, 2016 at 09:30 AM.

Student number:	4077407	
Project duration:	August 1, 2015 – July 1, 2016	
Thesis committee:	Prof. dr. ir. L. L. M. Veldhuis,	TU Delft, chair
	Dr. ir. R. Vos,	TU Delft, supervisor
	Dr. ir. C. Kassapoglou,	TU Delft

Registration number: 082#16#MT#FPP

Date: 5 July 2016

An electronic version of this thesis is available at http://repository.tudelft.nl/.

TU Delft

Summary

The goal for this thesis was to develop a semi-analytical weight estimation method for pressurized, composite, oval fuselages. This method was implemented into the FPP Initiator, written in Matlab. In doing so, the oval fuselage concept can be investigated in conceptual aircraft design of unconventional configurations, such as the blended wing body. These type of aircraft require a non-circular fuselage with an aerodynamic shape, for which the oval fuselage is one of few available concepts. With the help of this thesis work, composite oval fuselage technology may be investigated, following the current trend in aerospace industry towards composite materials.

The fuselage was modeled as a 1-dimensional beam to compute the internal loads. Application of the boom method provides the method with internal stresses and shear flow. This method was chosen not only because it can capture any beam geometry (arbitrary cross-section and taper along the beam axis), but also because it incorporates the material Young modulus, enabling both isotropic (metal) and orthotropic (fiber composite) materials.

Using the calculated loads, the structural components are sized: the skin, stringers and sandwich panels in the trapezoidal structure. An idealized structure was assumed, where the skin carries the membrane loads due to pressurization and the shear flow, while stringers carry direct stresses resulting from the bending moments. Finally, sandwich panels carry all loads in the face sheets, while the core adds bending stiffness.

By assuming initial dimensions for the structural components, consecutively computing loads and then sizing these components to get more accurate dimensions and repeating this process until it converges upon the component dimensions the weight estimation method is able to provide a consistently sized fuselage. This was done such that such a convergence loop does not have to be performed outside of the FWE.

Three separate optimization methods were developed based on previous work to size the skin panels, stringers and sandwich panels based on applied loads. This deterministic optimization approach builds a laminate stacking sequence based on a most critical failure mode. In case of the stringers, the member widths are determined using an additional optimization loop, similar to how the core thickness is optimized for sandwich panels. Even though this approach proved to be much faster than a full-blown optimization, it was found to be too computationally expensive for in-the-loop use.

As a solution to the aforementioned problem, a surrogate modeling approach was adopted. Neural networks proved to be most capable of representing the complex responses obtained from a design of experiments and offer an acceptable in-the-loop evaluation time.

One of the main challenges with non-circular fuselages like the oval fuselage is pressurization. The current method estimates pressurization loads as if each fuselage section were a straight tube, such that the analytical solution for a circular cylinder may be used in each arc. The mismatch of hoop loads is carried by the trapezoidal structure. An attempt was made to apply a finite difference method to compute the membrane loads in an arbitrary shell, but although the method was capable of computing the hoop load correctly, the longitudinal load was approximated incorrectly and therefore the method was abandoned. It still remains to be seen whether the 3-dimensional shape of the oval fuselage is capable of withstanding pressurization loads without deformation.

Validation of the panel failure analysis showed good agreement with finite element analysis or a conservative behavior of the analytical method. The Tsai-Wu failure criterion, however, was underestimated by around 20 %, but the impact of this on the overall mass estimation is small. Comparison with genetic algorithms showed the optimization methods implemented are capable of finding optimal designs, even outperforming the genetic algorithms for stringers and sandwich panels.

Finally, several case studies were performed. Moving from an aluminium design to a composite fuselage resulted in a fuselage mass reduction of on average 15 %. A composite oval fuselage was even lighter than its aluminium design by 32 %. Additionally, the effect of using stiffened panels instead of sandwich panels in the trapezoid structure was studied, which showed a significant mass penalty is associated with this.

Preface

This report is written as partial fulfillment of the Master's degree in Aerospace Engineering at Delft University of Technology. It concludes my thesis research and thereby my entire studies. Aircraft design is one of my great interests and with this thesis I hope to have contributed to the body of knowledge in novel aircraft design. Through the curriculum and extra-curricular activities like the AIAA Aircraft Design Competition and the DUT Racing Team I feel my time here in Delft has been fruitful and prepared me well for whatever lies ahead.

First and foremost, I would like to thank my supervisor dr.ir. Roelof Vos for his critical attitude towards my work and results. Answering his in-depth and to-the-point questions I often reconsidered my solutions and improved them. His ideas and advice have proven invaluable for the outcome of this project. Furthermore, I would like to thank dr.ir. Christos Kassapoglou for his advice on sizing composite structures and considerations on composite fuselage design. Additionally, I want to thank ir. Imco van Gent for helping me out with the program he wrote for his thesis work, which became a pivotal part of my own research. I would also like to thank my committee: prof.dr.ir. Leo Veldhuis, dr.ir. Roelof Vos and dr.ir. Christos Kassapoglou.

I would also like to thank my fellow students in "Kamertje 1", who made working during this period a lot more enjoyable. The discussions about the Initiator and on aircraft design in general were very interesting indeed. My final expression of gratitude is for my family and friends. Especially, I want to thank my parents, for their continuous support in all of my endeavours.

M.N. Roelofs
Delft, June 2016

Contents

List of Figures

List of Tables

Nomenclature

Abbreviations

Abbreviation	Definition
ACT	NASA Advanced Composite Technology
ALGO	Additive Lay-up Generation Optimizer
ATCAS	Boeing's Advanced Technology Composite Aircraft Structure
BWB	Blended Wing Body
CLT	Classical Lamination Theory
ELFO	Enumerative Lay-up Family Optimizer
FBD	Free Body Diagram
FEA	Finite Element Analysis
FF	Fiber Failure
FPP	Flight Performance and Propulsion
IFF	Inter Fiber Failure
MAC	Mean Aerodynamic Chord
MTOM	Maximum Take-Off Mass
MZFW	Maximum Zero Fuel Mass
NEF	No Edge Free
OEF	One Edge Free
OEI	One Engine Inoperative
OEM	Operational Empty Mass
PDE	Partial Differential Equation
RMSE	Root Mean Squared Error

Greek Symbols

Symbol	Description	Units
β	Angle of wall with vertical	rad
δ	Deflection	m
ν	Poisson ratio	-
ρ	Density	kg/m^3
σ	Direct stress	N/m^2
τ	Shear stress	N/m^2

Roman Symbols

Symbol	Description	Units
A	Area (of cross-section)	m^2
a	Length (of panel)	m
a_g	Gust decay	$\mathrm{fts}^{-1}]\mathrm{ft}^{-1}$
AR	Aspect ratio	-
B	Boom area	m^2
b	Width (of panel)	m
c	Centroid coordinate	m
c	Chord length	m
C_{L_α}	Lift curve slope	rad^{-1}
E	Young's modulus	N/m^2
G	Shear modulus	N/m^2
g	Gravitational acceleration	m/s
h	Height	m
I	Second moment of area	m^4
I'	Weighted second moment of area	$N\ m^2$
L	Length	m
M	Bending moment	N m
N	Line load	N/m
n	Load factor	-
P	Boom load	N
p	Pressure	N/m^2
q	Shear flow	N/m
r	Radius	m
S	Shear force	N
S	Shear strength	N/m^2
S	Surface area	m^2
t	Thickness	m
V_g	Gust velocity	$\mathrm{ft/s}$
W	Weight	N
w	Width	m
X	Longitudinal strength	N/m^2
Y	Transverse strength	N/m^2

Subscripts & Superscripts

Symbol	Definition
°	Middle surface of laminate
B	Boom
c	Compression
c	Core
f	Facing
t	Tension
1,2,3	Top arc (1), side arc (2) and bottom arc (3)
buck	Buckling
crimp	Crimping
crit	Critical
crp	Crippling
c	Ceiling (of trapezoid)
eq	Equivalent
fr	Frame
f	Floor (of trapezoid)
g	Gust
hoop	Hoop direction
long	Longitudinal direction
mat	Material
pan	Panel
req	Required
s	Symmetric
ult	Ultimate
wr	Wrinkling

1 Introduction

The Blended Wing Body (BWB), aims to reduce fuel consumption and improve aerodynamic performance [1]. The concept is one of many novel aircraft configurations devised to compete with and replace the current conventional tube-and-wing configuration. Decades of improving the latter concept have exhausted the possibilities for further major improvements and thus the aircraft industry is looking for new options.
One of the challenges in designing a BWB aircraft is the fuselage, which becomes very wide and often has an airfoil-like shape in the symmetry plane cross-section. The fuselage has to resist internal pressure and spheres are the most optimal shape to resist the pressurization loads. Cylinders, as used in conventional aircraft, are also very efficient pressure vessels. The reason for this is that a circular shape is able to carry the pressure load in tension entirely; it acts as a membrane. A non-circular shape will, in addition to the tensile internal loads, develop internal bending moments due to the pressurization and as such will need more material to cope with these loads. Obviously, such a pressure vessel will be much heavier. All loads acting on a shell element are shown in Figure 1.1. Membrane loads are shown in red: N_x, N_y and N_{xy}. For a non-membrane element, the out of plane loads V_x and V_y develop, shown in blue. Additionally, bending moments develop to resist out-of-plane loads, shown in green.

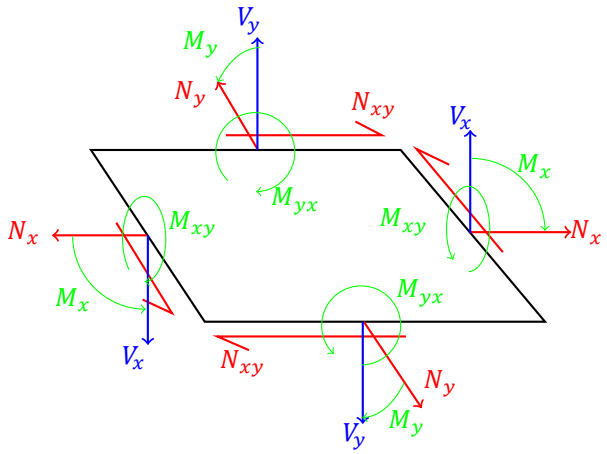

Figure 1.1: Membrane and shell loads

Several solutions have been proposed to deal with the problem of a non-cylindrical pressurized fuselage. Most commonly, the multi-bubble (see Figure 1.2a) and stiffened-shell (see Figure 1.2b) concepts are proposed [1–5]. However, a new concept was proposed at the TU Delft: the oval fuselage (see Figure 1.2c). This concept, unlike the others, does not rely on members that have to be placed in the cabin to carry the out-of-plane loads and thus results in an unobstructed cabin space. The idea of this concept is that a cross-section is composed of four circular arcs, which are tangent at the connections. To carry the difference in membrane forces in these arcs, a trapezoidal structure connects the four intersections.

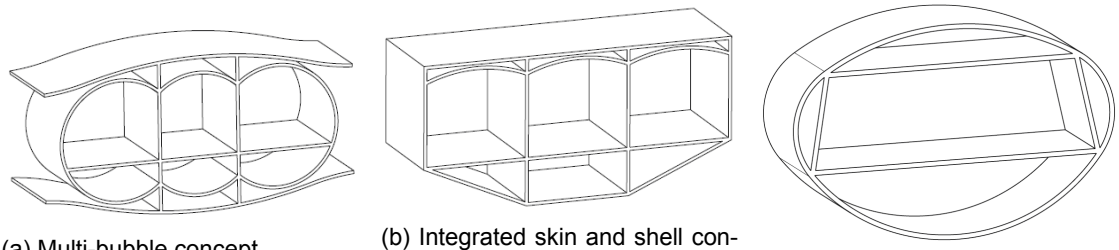

(a) Multi-bubble concept

(b) Integrated skin and shell concept

(c) Oval fuselage concept

Figure 1.2: Three concepts for non-circular, pressurized fuselages

Multi-bubble The multi-bubble concept, see Figure 1.2a, uses multiple cylindrical elements which are linked together in either an open- or closed-cell configuration. Therefore, pressurization loads are carried in hoop-tension and no bending loads due to pressurization occur [6]. According to Mukhopadhyay [3], the multi-bubble configuration appears to be twice as inefficient compared to a cylindrical configuration, but it could reduce overall weight by about 20% to 30% compared to using flat surfaces. Extensive research has been conducted by NASA on non-cylindrical fuselages, including composite ones, and the multi-bubble appears in many of these studies, reinforcing its feasibility [3–5].

Skin and Shell The integrated skin and shell concept, see Figure 1.2b, uses either a deep honeycomb or stiffened frame construction, following the outer aerodynamic contour of the aircraft, and was chosen for the BWB study by Liebeck [1], but NASA has also given it attention in several studies into structural concepts for non-circular fuselages [2, 7, 8]. Walls are present to carry part of the pressurization loads. Flat shells as used in this concept are not suitable for carrying pressurization, but the simplicity of the concept makes it attractive nonetheless. One could also replace the honeycomb with stiffening ribs, which could decrease weight. The lightest configuration would be a double-skin vaulted ribbed-shell concept [2].

Oval fuselage The oval fuselage, see Figure 1.2c, features an outer skin made from four circular arcs, which are connected tangentially: a top arc, a bottom arc and two identical side arcs. The cabin is defined by a trapezoidal structure of straight panels, and the corner points coincide with the arc joints. As such, the outer skin carries the pressure loads in membrane action, while the trapezoidal structure carries the remaining loads resulting from pressurization.
The oval fuselage concept was first presented by Hoogreef and Vos [9]. A weight estimation methodology was developed that determines the structural members' thicknesses, depending on pressurization and wing-bending loads. The longitudinal stresses from pressurization, axial acceleration and fuselage bending are checked to be below tensile and compressive fatigue limits. The method is combined with the Torenbeek class II.5 weight estimation for other structural components and wings. It is concluded that the oval fuselage has the advantage over the previously mentioned two concepts that the cabin space is unobstructed. A 400 passenger oval-fuselage BWB was shown to have 13% lower OEM and 6% better fuel consumption in comparison to conventional airliners.
This research was carried on by Schmidt [10], where the parameterization was extended to allow for a non-symmetrical airfoil shape along the fuselage centerline. The weight estimation developed uses the plane stress assumption and sizes the fuselage based on several load conditions. The outer shell was modeled as a stiffened skin, while the trapezoidal structure consisted of sandwich panels. Dimpling, crimping, wrinkling and global buckling of these sandwich beams were taken into account. Inertial and aerodynamic loads are obtained at each cross-section by representing the fuselage as a 1-dimensional beam.
In order to validate the above weight estimation method, a finite element analysis was developed using a knowledge-based engineering approach by De Smedt [11]. It was shown there was good correspondence in lateral and hoop stresses, while longitudinal and shear loads showed significant differences.

Composite Fuselage In addition to the trend towards unconventional configurations, the aircraft industry is also moving towards new materials. The first, mostly composite, aircraft have already taken

flight; the Airbus A350 and Boeing 787. Composites may increase lifetime and safety, while reducing cost and weight, but companies are hesitant to apply them, since the advantages can not be guaranteed [12] and production facilities have to be completely modified [13]. Nonetheless, aircraft industry is applying more and more composite parts in aircraft and it is not unlikely that novel aircraft will feature major components made from fiber composites. It is therefore the main focus of the present work.

1.1. Thesis Goal and Research Question

Former research was conducted focusing on the weight estimation of the oval fuselage concept, made with metals (usually aluminium). This semi-analytical method uses simple beam theory to compute loads and analytical expressions for failure criteria of structural components in an effort to size these. Building upon that research, this research will focus on a similar weight estimation method, but using fiber composite material for the entire fuselage structure. To analyze the oval fuselage concept in unconventional aircraft, the method is implemented in the Initiator, a preliminary aircraft design tool in development at the TU Delft. Concluding, the research goal can be defined as:

Develop a semi-analytical weight estimation method for a pressurized, composite, oval fuselage to be implemented in the FPP Initiator by writing a physics based program in Matlab

The research itself focuses on how this goal can be achieved, i.e. what such a method requires and which methods it needs to estimate relevant parameters. Moreover, the structural design of an oval fuselage has a large influence on both the methods to be used and the eventual feasibility of the concept. Hence, the research question is:

How can the weight of an oval, composite, pressurized fuselage be estimated in the conceptual design phase of unconventional aircraft?

This research question is quite broad and has to be split into several sub-questions, listed below. Obviously, more questions could have been made, because many different aspects come into play for the weight estimation of a fuselage (load cases, crashworthiness and splicing, to name a few). However, the three questions below are most important and are the focus of the present research.

- *Which failure modes and corresponding equations should be used to size a composite stiffened skin structure and sandwich structure depending on applied loads?*
- *How can the skin thickness, stacking sequence and number of layers be determined for a composite laminate, within a time suitable for conceptual design?*
- *What is the effect of the oval fuselage shape in 3 dimensions on the pressurization loads?*

1.2. Description of Oval Fuselage

One of the advantages of an oval fuselage over the multi-bubble or integrated skin and shell is an unobstructed cabin space. This allows for more freedom in designing the cabin interior, which increases the flexibility of such a fuselage.

1.2.1. Inside-out Approach for Sizing Oval Fuselage Outer Geometry

An oval cross-section as depicted in Figure 1.3 can be defined by four parameters: h_1, h_2, h_3 and w_f. All other parameters can be derived from these four. From a specification of cabin layout (seating configuration, class distribution and number of passengers), the floor contour can be defined. Secondly, from cargo requirements an amount of cargo volume (and dimensions if containers are used) can be deduced. Assuming the cargo hold is below the passenger floor, h_3 is defined in this way. The cabin height h_2 is a designer's choice, with a minimum specified by regulations. What remains to be defined is h_1. Using an optimization method, h_1 may be found that minimizes the cross-sectional area, while having the cross-section passing through or around points that define the minimal cabin (floor width, cabin height, seat height, etc.).

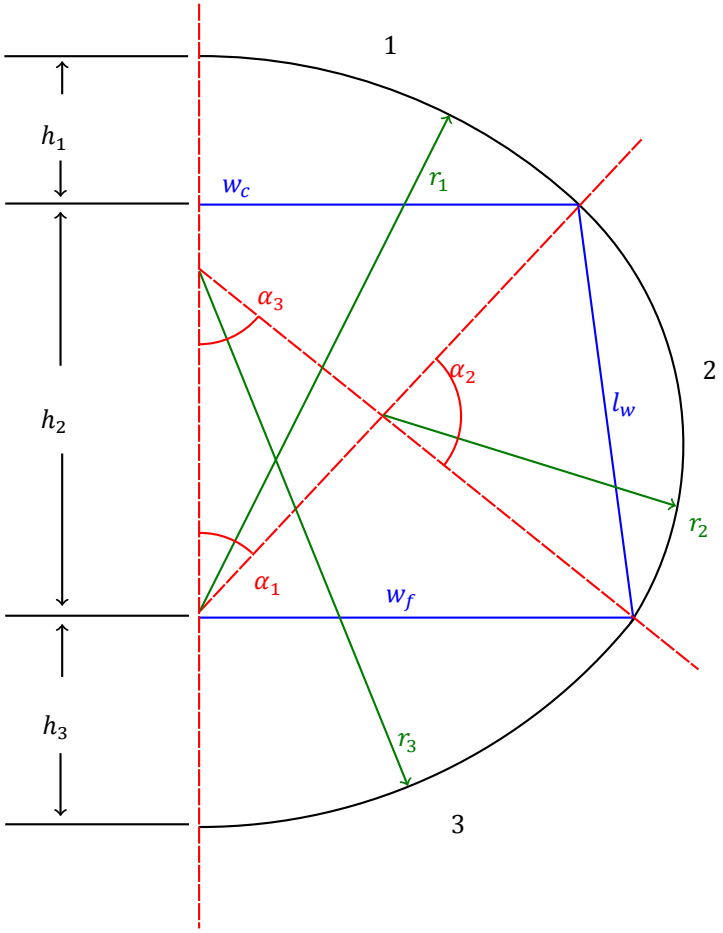

Figure 1.3: Parametric description of oval cross-section

Defining:

$$a = w_f$$
$$b = h_1 \cdot h_3 + h_2 \cdot h_3 - w_f^2$$
$$c = -h_1 \cdot w_f \cdot (h_2 + h_3)$$

the ceiling width w_c is obtained using the quadratic formula:

$$w_c = \frac{-b \pm \sqrt{b^2 - 4ac}}{2a} \tag{1.1}$$

One of the two solutions is either negative or close to zero, leaving only one possible value for w_c. By defining:

$$\theta_1 = \tan^{-1} \frac{w_c}{h_1}$$
$$\theta_3 = \tan^{-1} \frac{w_f}{h_3}$$
$$\beta = \tan^{-1} \frac{w_f - w_c}{h_2}$$
$$\gamma = \pi - 2\theta_3 - \beta$$

the radii of the circular arcs (and the length of the wall) may be determined as follows:

$$r_1 = \frac{w_c}{2 \sin\theta_1 \cos\theta_1} \tag{1.2}$$

$$l_w = \frac{h_2}{\cos\beta} \tag{1.3}$$

$$r_2 = \frac{l_w}{2 \cos\gamma} \tag{1.4}$$

$$r_3 = \frac{w_f}{2 \sin\theta_3 \cos\theta_3} \tag{1.5}$$

Now the angles that each of the circular arcs span can be computed as follows:

$$\alpha_1 = \sin^{-1}\frac{w_c}{r_1} \tag{1.6}$$

$$\alpha_3 = \sin^{-1}\frac{w_f}{r_3} \tag{1.7}$$

$$\alpha_2 = \pi - \alpha_1 - \alpha_3 \tag{1.8}$$

Finally, the locations of the centers of the circular arcs need to be determined. Logically, the lateral positions of the centers of the top and bottom arc lie on the symmetry axis.

$$\begin{aligned} c_{1,y} &= 0 \\ c_{1,z} &= h_1 + h_2 - r_1 \\ c_{2,y} &= w_c - r_2 \sin(\gamma - \beta) \\ c_{2,z} &= h_2 - r_2 \cos(\gamma - \beta) \\ c_{3,y} &= 0 \\ c_{3,z} &= r_3 - h_3 \end{aligned}$$

1.3. Outline

The structure of this report is as follows: chapter 2 discusses the structural analysis and gives an overview of the entire weight estimation method. The sizing of composite structural components is elaborated upon in chapter 3. Because the methods outlined in chapter 3 require too long an in-the-loop computation time, surrogate modeling was employed, which is explained in chapter 4. Regarding the third sub-question, chapter 5 focusses on the problem of pressurization in an oval fuselage. chapter 6 presents the verification and validation procedures and results. Since both composite and oval fuselage designs are hard to validate (no data is available), results from the presented method are not included in the verification and validation chapter, but rather in the separate chapter 7 as case studies. Finally, in chapter 8 the research question is answered and conclusions are drawn with respect to the applicability and feasibility of the presented approach. Moreover, recommendations for further research and improvements on the current work are given. Several appendices are included in this report, being the operational manuals and other information required to run the developed weight estimation method.

2

Structural Design and Analysis

Mass estimation is in the strict sense only an analysis of a certain structure or geometry in general. However, in the current work, only an outline of the fuselage shape is available, but the structural dimensions have yet to be determined. Therefore, the mass estimation method also needs to size the fuselage structure.
In this chapter an outline is provided for the entire mass estimation method developed in this thesis work. First, its role in the Initiator aircraft design tool is described. Secondly, the program flow of the mass estimation method itself is discussed. The components of this process are subject of later sections and chapters. Thirdly, the methods to determine applied and internal loads are elaborated upon. Finally, the mass estimation of secondary structure and non-structural components is described.

2.1. Initiator

As was specified in the thesis goal, the weight estimation method developed during this thesis should be implemented in the FPP Initiator. The Initiator is a conceptual and preliminary aircraft design tool, which aims to size and analyze conventional and unconventional aircraft based on a user specified set of top level requirements and settings. The process flow of a design convergence loop is shown in Figure 2.1, where it can be seen that the Initiator's design process can be divided into three major blocks: Class I, Class II and Class II.5. The former two are based on Roskam's design process [14], but the third aims to analyze components of the aircraft using physics and geometry based methods, rather than empirical relations. As such, the present fuselage weight estimation method fits in the Class II.5 block of the Initiator.

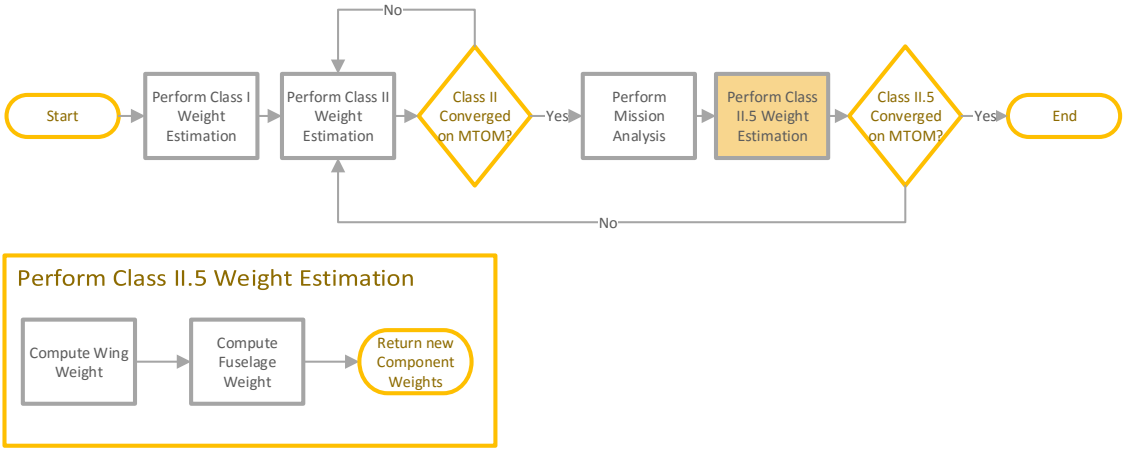

Figure 2.1: Initiator process flow

2.2. Program Flow

Figure 2.2 shows the flowchart of the weight estimation method. It should be noted that this method itself is part of a larger convergence loop built into the Initiator, which ensures all aircraft weights become consistent between all methods implemented, as was shown in Figure 2.1.

The fuselage weight estimation method starts by retrieving the aerodynamic and weight data from the Class II methods implemented in the Initiator. Moreover, it checks whether a design vector exists from a previous fuselage weight estimation run. If that is the case, this design will be used as the initial guess for the convergence loop of the current run. Otherwise, a new design vector is built using predefined initial values. This design vector describes all structural dimensions and other properties required to perform the structural analysis and compute the mass. The parameters that are estimated and converged upon, as well as the initial values, are given in Table 2.1.

Table 2.1: Design vector for weight estimation method

Parameter	Unit	Type	Initial Value
Skin Thickness	m	$N_{sections} \times 3$ Matrix	$(\Delta p)_{\text{cruise}} \cdot r_i^{\text{arc}} / X^t$
Stringer Smeared Thickness	m	$N_{\text{sections}} \times 3$ Matrix	$\eta_{\text{stringer}} \cdot t_{\text{skin}}$
Frame Smeared Thickness	m	$N_{\text{sections}} \times 3$ Matrix	$\eta_{\text{frame}} \cdot t_{\text{skin}}$
Ceiling Face Thickness	m	N_{sections} Column Vector	8e-3
Wall Face Thickness	m	N_{sections} Column Vector	1e-3
Floor Face Thickness	m	N_{sections} Column Vector	8e-3
Ceiling, Wall and Floor Core Thickness	m	N_{sections} Column Vectors	8e-3
Stringer Pitch p	m	$N_{\text{sections}} \times 3$ Matrix	0.15
Stringer Width w	m	$N_{\text{sections}} \times 3$ Matrix	0.02
Skin Young's Modulus	Pa	$N_{\text{sections}} \times 3$ Matrix	Material Setting
Stringer Young's Modulus	Pa	$N_{\text{sections}} \times 3$ Matrix	Material Setting
Sandwich Face Young's Modulus	Pa	$N_{\text{sections}} \times 3$ Matrix	Material Setting

It should be noted that in Table 2.1 the stringer width parameter is not used by the composite weight estimation, whereas the metal weight estimation does not use the last three parameters, i.e. the Young's modulus parameters. The first three parameters have computed initial values, where r_i^{arc} is the radius of an arc ($i = 1, 2, 3$), X^t is the material strength in tension and η_{stringer} and η_{frame} are the stringer-to-skin and frame-to-skin ratio (in terms of smeared thickness), respectively. These ratios are assumed to be 0.2, but are only used here as a first guess, so do not have an influence on the final result.

Using the weight and aerodynamic forces from Class II, beam theory is employed to compute the shear and moment distributions, as is explained in section 2.3. Consecutively, also using Class II data, the lateral and transverse loads acting on the trapezoidal structure are computed. Finally, the pressurization loads are computed. With these loads and the load cases from Table 2.3, the loads corresponding to each load case are computed.

All computations done so far by the fuselage weight estimation will not change during the convergence loop. In reality, with the changes in thickness each iteration, the structural weight would change and as such the aerodynamic and other properties of the aircraft would change. However, to recompute all of these each iteration would be cumbersome and computationally expensive. Moreover, the fuselage weight estimation itself is part of a convergence loop which makes sure that effects as the ones described here are taken into account.

Each iteration of the fuselage weight estimation, the boom method described in section 2.5 is employed to determine the shear flow and boom stresses in the fuselage skin. Additionally, the stresses in the trapezoidal structure are computed. With these stresses, the skin panels, stringers and trapezoidal members (floor, wall and ceiling) are sized for each section the fuselage is divided into. At the end of each iteration, the loop checks whether the changes made with respect to the previous design are within a certain tolerance, in which case the procedure stops. A mathematical description of the convergence criterion is:

$$\bar{X}_{(k)} / \bar{X}_{(k-1)} - 1 \leq \epsilon \tag{2.1}$$

where ϵ is the tolerance set to 1 %. Finally, the mass of the obtained design is computed, complemented by adding empirical weights (see section 2.8) for those components that were not sized by the analytical model.

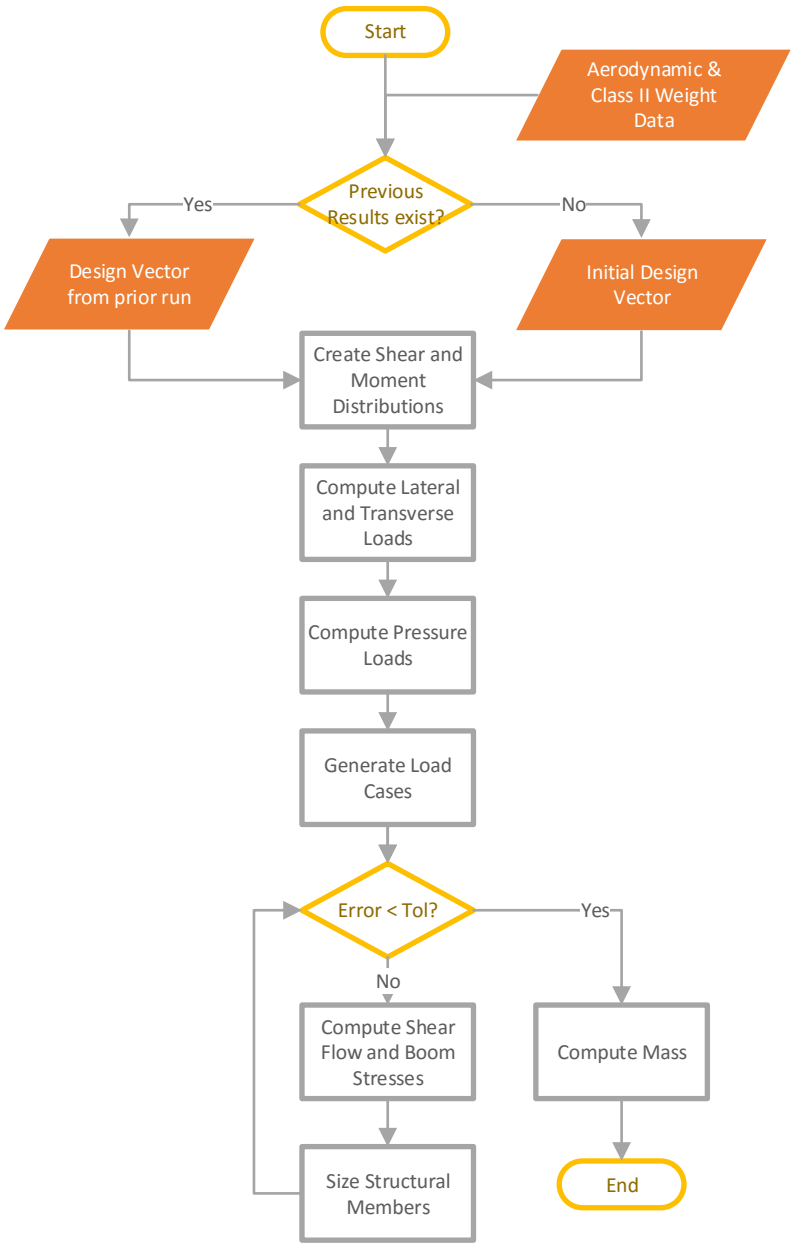

Figure 2.2: Fuselage weight estimation process flow

Table 2.2: Load types per component

Inertial		
Component	Attached to	Load type
Engine	Wing	Point Force + Moment
	Fuselage	Point Force
Landing Gear	Wing	Point Force + Moment
	Fuselage	Point Force
Wing	Fuselage	Point Force + Moment
Fuel Tank	Wing	Point Force + Moment
	Fuselage	Point Force
Furnishing	Fuselage	Non-linearly Distributed Force
Fuselage	-	Non-linearly Distributed Force
Systems	Fuselage	Non-linearly Distributed Force
Operational Items	Fuselage	Non-linearly Distributed Force
Bulk Cargo	Fuselage	Non-linearly Distributed Force
ULD	Fuselage	Point Force
Passenger	Fuselage	Point Force
Aerodynamic		
Component	Load type	
Fuselage	Non-linearly Distributed Force + Moment	
Wing	Point Force + Moment	
Engine	Point Force + Moment	

2.3. Shear Force and Bending Moment Distribution

Detailed calculation of the internal loads in a fuselage is usually only possible using finite element analysis or similar techniques. For a conceptual weight estimation method it suffices to model the fuselage as a cantilever beam. All weights and aerodynamic forces can be projected onto this beam and statics is used to determine the resulting shear force and moment distributions.
The loads that are projected onto the cantilever beam can be divided into point loads, linearly distributed loads and nonlinear distributed loads. Passengers are point loads and systems are nonlinear distributed loads, for example. For a complete overview of the components and types of loads, refer to Table 2.2.

2.4. Load Cases

Several load cases are considered to obtain the critical loads for the structure. The current weight estimation method makes use of a tentative set of load cases, which are listed in Table 2.3. Each structural component is sized for all load cases, and the thickest/heaviest design is taken as the final design for that component.

Table 2.3: Load cases for fuselage structure

Load Case	Load Factor	Mass	Wing Loads	Pressure	OEI
1	2.5	MTOM	$W_{F,\max}$, Aero	Cruise	No
2	2.5	MZFW	$W_{F,\min}$, Aero	Cruise	No
3	-1.5	MTOM	$W_{F,\max}$, Aero	Cruise	No
4	-1.5	MZFW	$W_{F,\min}$, Aero	Cruise	No
5	2.5	MTOM	$W_{F,\max}$, Aero	0	No
6	2.5	MZFW	$W_{F,\min}$, Aero	0	No
7	-1.5	MTOM	$W_{F,\max}$, Aero	0	No
8	-1.5	MZFW	$W_{F,\min}$, Aero	0	No
9	2.5	MLM	$W_{F,\min}$	Landing	No
10	2.5	MLM	$W_{F,\min}$	0	No
11	Gust up	MZFW	$W_{F,\min}$, Aero	Cruise	No
12	Gust down	MZFW	$W_{F,\min}$, Aero	Cruise	No
13	1.0	MTOM	$W_{F,\max}$, Aero	Cruise	Yes

The Mass column in Table 2.3 defines the total weight the aircraft flies with in a specific load case. The Wing Loads column defines the wing bending, which influences the lateral loads imposed on the trapezoidal structure. $W_{F,\max}$ is maximum fuel weight in the wings, while $W_{F,\min}$ is only the minimum fuel fraction remaining (trapped fuel). Moreover, Aero indicates that aerodynamic bending loads are present.
In the Pressure column the cabin pressure is defined. Cruise means the differential pressure when the cabin is at its cruise cabin altitude and the outside pressure at the cruise altitude. Landing is defined by a setting for the minimum cabin differential pressure. Both landing and cruise cabin pressures are multiplied by a safety factor of 1.5 and a factor of 1.15 stipulated by regulations [15].
The last column indicates whether a one engine inoperative (OEI) condition is present in the load case, i.e. whether the vertical tail induces a sideways shear force and the operative engines a moment around the yaw axis.
The load factor due to gusts is explained in the following. Both gusts induce a certain load factor on the aircraft, and since these can be more sizing than the other load factors present, they are included separately. To compute the gust load factors, the so called gust decay in altitude is computed as follows:

$$a_g = \frac{25 - 50}{30000} \quad \mathrm{fts^{-1}ft^{-1}} \tag{2.2}$$

Then using this decay and the cruise altitude of the aircraft in feet, the gust velocity is:

$$V_g = a_g(h - 20000) + 50 \quad \mathrm{ft/s} \tag{2.3}$$

Now the gust factor is computed with the following two equations:

$$\mu = \frac{2W}{S\rho g C_{L_\alpha} c} \tag{2.4}$$

$$k_g = \frac{0.88\mu}{5.3 + \mu} \tag{2.5}$$

where W is the aircraft weight, S the main wing surface area, C_{L_α} the main wing lift curve slope and c it's mean aerodynamic chord (MAC). Finally, the change in load factor due to a gust is:

$$\Delta n_g = \frac{k_g \cdot C_{L_\alpha} \cdot 0.5 \cdot \rho \cdot V \cdot V_g}{W/S} \tag{2.6}$$

and the two gusts impose a load factor being either $1 + \Delta n_g$ (gust up) or $1 - \Delta n_g$ (gust down).

2.5. Boom Method

To compute the internal direct stresses due to the bending moment and shearflow due to shear forces, a boom method is applied. An important reason for this decision is that the boom method allows for a different stiffness of each skin panel and boom, which makes the method very useful for analyzing anisotropic composite structures. Moreover, using Megson [16] as a guideline, the boom method was adapted to account for tapering of the fuselage, such that the complex geometry of a BWB fuselage can be analyzed. It is assumed that skin panels only carry shear and stringers (booms) only take direct stress. Furthermore, the oval section is analyzed as a single-cell section as can be seen in Figure 2.3, with the wall thickness added to the side arc thickness. Through this assumption, the ceiling and floor members carry no shear flow, while the wall member shares the shear flow with the side arc.
The second moments of area including the Young's modulus of each panel and stringer are defined as:

$$I'_{xx} = \int_A E_{z_i} y^2 \mathrm{d}A \tag{2.7}$$

$$I'_{yy} = \int_A E_{z_i} x^2 \mathrm{d}A \tag{2.8}$$

$$I'_{xy} = \int_A E_{z_i} xy \mathrm{d}A \tag{2.9}$$

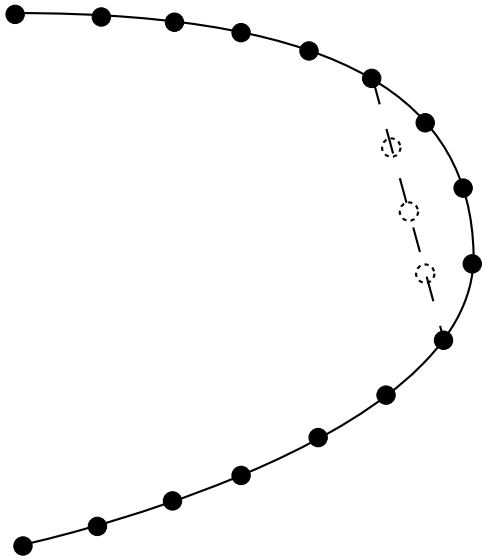

Figure 2.3: Structural idealization of oval fuselage

where x is the section horizontal coordinate and y the section vertical coordinate. Additionally, E is the Young's modulus, with the subscript z indicating it is the modulus in the fuselage longitudinal direction. Finally, A is the cross-section area and the subscript i refers to each member over which the integral is taken.

In each member, the direct stress due to bending moment can then be computed using:

$$\sigma_z = E_{z_i}\left[\left(\frac{M_y I'_{xx} - M_x I'_{xy}}{I'_{xx} I'_{yy} - {I'_{xy}}^2}\right)x + \left(\frac{M_x I'_{yy} - M_y I'_{xy}}{I'_{xx} I'_{yy} - {I'_{xy}}^2}\right)y\right] \tag{2.10}$$

Here the subscript i again refers to the member under consideration. M_x is the vertical bending moment (around the section horizontal axis) and M_y is the horizontal bending moment (around the section vertical axis).

Using the stresses computed with Equation 2.10, the boom areas can be computed using:

$$B = A_{str} + \frac{t_1 \cdot b_1}{6}\left(2 + \frac{\sigma_1}{\sigma_B}\right) + \frac{t_2 \cdot b_2}{6}\left(2 + \frac{\sigma_2}{\sigma_B}\right) \tag{2.11}$$

where the numeric subscripts refer to the skins attached to the boom under consideration, denoted by subscript B.

Knowing the boom stresses and areas, the three components of the internal boom loads can be computed as follows:

$$P_{z,r} = \sigma_{z,r} \cdot B_r \tag{2.12}$$

$$P_{y,r} = P_{z,r}\frac{\mathrm{d}y}{\mathrm{d}z} \tag{2.13}$$

$$P_{x,r} = P_{z,r}\frac{\mathrm{d}x}{\mathrm{d}z} \tag{2.14}$$

In these equations, $\mathrm{d}x$, $\mathrm{d}y$ and $\mathrm{d}z$ are the change in the respective coordinates along the boom (endpoint minus start point).

Using these loads, the boom shear forces are computed using:

$$S_{x,w} = S_x - \sum_{r=1}^{m} P_{x,r} \tag{2.15}$$

$$S_{y,w} = S_y - \sum_{r=1}^{m} P_{y,r} \tag{2.16}$$

where S_x and S_y are the applied shear forces.
The shear flow is computed as follows:

$$q_s = q_b + q_{s,0} \tag{2.17}$$

The first component of the shear flow is given by:

$$q_b = -E_{z,i}\left(\frac{S_{x,w}I'_{xx} - S_{y,w}I'_{xy}}{I'_{xx}I'_{yy} - {I'_{xy}}^2}\right)\sum_{r=1}^{n} B_r x_r - E_{z,i}\left(\frac{S_{y,w}I'_{yy} - S_{x,w}I'_{xy}}{I'_{xx}I'_{yy} - {I'_{xy}}^2}\right)\sum_{r=1}^{n} B_r y_r \tag{2.18}$$

and represents the open section shear flow. For the closed section shear flow, a constant shear flow $q_{s,0}$ is added, which is obtained by equating:

$$S_x\eta_0 - S_y\xi_0 = \oint q_b p \mathrm{d}s + 2Aq_{s,0} - \sum_{r=1}^{m} P_{x,r}\eta_r + \sum_{r=1}^{m} P_{y,r}\xi_r \tag{2.19}$$

The variable p is the distance from the shear center to a point on the cross-section where the integral is evaluated. Moreover, as can be seen in Figure 2.4, $\mathrm{d}s$ is a differential distance along the beam section, η_0 and ξ_0 are the moment arms of the applied shear forces to the shear center and q is the shear flow.

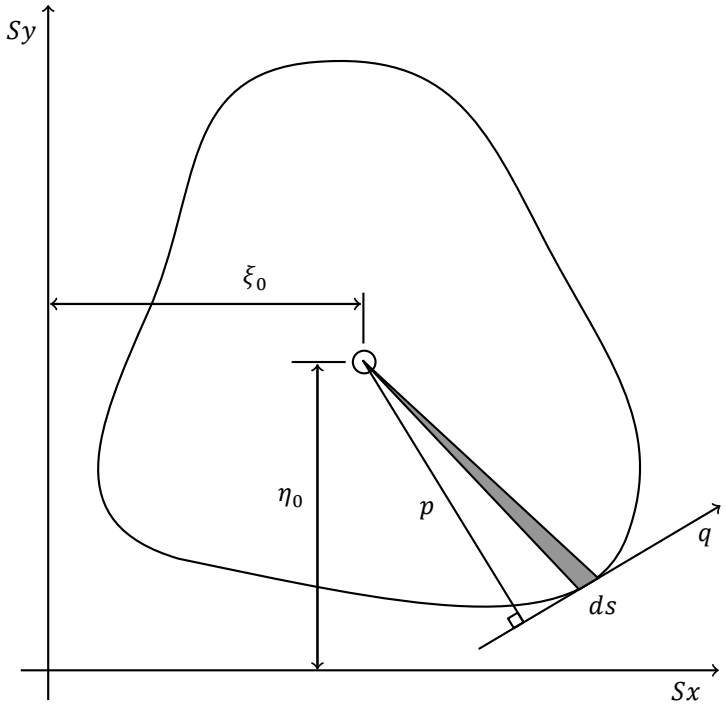

Figure 2.4: Closed beam section for determining $q_{s,0}$

2.6. Pressurization Loads

In the 2D case of the oval fuselage, the pressure stresses in hoop direction in the circular arcs can be determined by:

$$\sigma_{\text{hoop}} = \frac{pr}{t} \tag{2.20}$$

and in the longitudinal direction by:

$$\sigma_{\text{long}} = \frac{pr}{2t} \tag{2.21}$$

Because the arcs have different radii, a mismatch in loads exists at the junctions, which have to be carried by the trapezoidal structure (otherwise these result in bending moments in the skin, requiring large thicknesses to cope with that). Suppose the line loads (N/m) in the circular arcs are called N_1, N_2 and N_3 and the loads in the trapezoid N_c, N_f and N_w, which denote the ceiling, floor and wall, respectively. In Figure 2.5 a free-body-diagram (FBD) of these forces is shown. These loads are positive for a member in tension and negative for compression. First the following angles are defined:

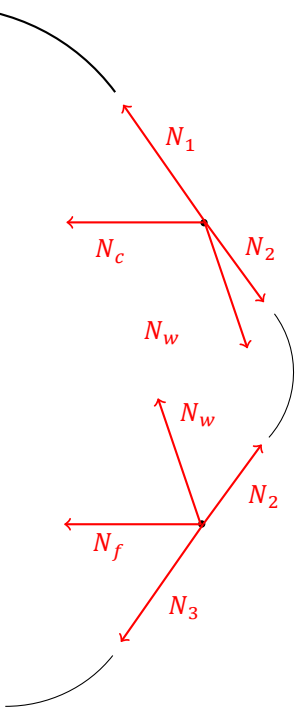

Figure 2.5: Pressurization forces FBD

$$\psi = \cos^{-1}\frac{w_c}{r_1}$$
$$\phi = \pi/2 - \psi$$
$$\gamma = \cos^{-1}\frac{w_f}{r_3}$$
$$\chi = \pi/2 - \gamma$$

Then the horizontal and vertical components of the member line loads are (note that N_c and N_f only have a horizontal component):

$$
\begin{aligned}
N_{1,x} &= N_1 \cos\phi \\
N_{1,y} &= N_1 \sin\phi \\
N_{2,x,\text{upper}} &= N_2 \cos\phi \\
N_{2,y,\text{upper}} &= N_2 \sin\phi \\
N_{2,x,\text{lower}} &= N_2 \cos\chi \\
N_{2,y,\text{lower}} &= N_2 \sin\chi \\
N_{3,x} &= N_3 \cos\chi \\
N_{3,y} &= N_3 \sin\chi \\
N_{w,x,\text{upper}} &= N_w \sin\beta \\
N_{w,y,\text{upper}} &= N_w \cos\beta \\
N_{w,x,\text{lower}} &= -N_{w,x,\text{upper}} \\
N_{w,y,\text{lower}} &= -N_{w,y,\text{upper}}
\end{aligned}
$$

The components of the side arc load have different magnitudes at the upper and lower junctions. The wall components do not, because the direction of the wall is the same at both junctions. However, the signs of the wall load components at the upper junction are logically opposite of those at the lower junction.
Then at the junction of arc 1 and 2 and the ceiling and wall, the following force equilibrium equations hold:

$$N_{2,x,\text{upper}} + N_{w,x,\text{upper}} - N_c - N_{1,x} = 0 \tag{2.22}$$

$$N_{1,y} - N_{w,y,\text{upper}} - N_{2,y,\text{upper}} = 0 \tag{2.23}$$

The second equilibrium equation can be solved directly for $N_{w,y}$, from which N_w follows by geometry. At the lower junction, the following equilibrium equations hold:

$$N_{2,x,\text{lower}} - N_{w,x,\text{lower}} - N_f - N_{3,x} = 0 \tag{2.24}$$

$$N_{2,y,\text{lower}} + N_{w,y,\text{lower}} - N_{3,y} = 0 \tag{2.25}$$

The second of these equations is not needed, since all those terms are already known. From the first equation then follows N_f.

2.7. Structure Sizing

Based on the material defined by the user to be used for the different components of the fuselage, either a metal sizing routine or a composite sizing routine is used. The metal sizing routines were developed in Ref. [10] and will not be discussed here. The sizing routines for composite members (flat skin panels, stringers and sandwich panels) are discussed in chapter 3.
The main purpose of the sizing procedure is to determine the dimensions of all structural members, such that the weight may be computed. However, for composite structures, the laminate stacking sequences also need to be determined. These result in the axial and bending stiffness of each member, which are used by the boom method.

2.8. Mass Estimation

For all metal secondary structure and non-structural masses, empirical relations from Howe [17] are used [9].
For the composite structural masses, trends from the NASA Advanced Composite Technology (ACT) program [18] and Boeing's Advanced Technology Composite Aircraft Structure (ATCAS) [19] are used. The skin, stringer and frame masses are predicted by the presented method and the masses for splicing, assembly, cargo floor and reinforcements around cutouts are estimated as a fraction of these.

From the side-panel study [18], the weight breakdown in Figure 2.6a is obtained. For the keel panels [19] the weight breakdown in Figure 2.6b is obtained.

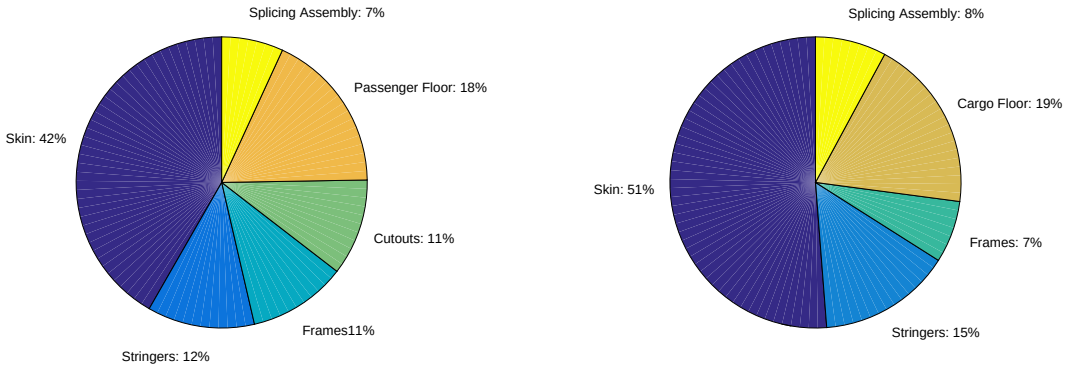

(a) Side panels

(b) Keel panels

Figure 2.6: Weight breakdowns for side and keel panels

From these breakdowns it can be estimated that skin/panel mass should lie around 42-52 % of the structural mass, stiffeners form around 12-15 % and frames between 7 and 11 %. For the side panels, these three items combined form 65 % of the mass. With that in mind, the window belt, skin panel assembly and door reinforcements may be sized as a fraction of the side panel primary structure mass. This fraction becomes 0.17 for the three items combined, from Figure 2.6a. The cargo floor is sized similarly, but now the keel panel primary structure (skin + stringers + frames) mass is used. Thus, from Figure 2.6b, the cargo floor fraction is 0.26. Finally, the splicing and assembly mass is taken as a fraction of the total primary structure mass with a value of 0.11.
Finally, the nose and aft shell (structure in front of and aft of the passenger cabin) masses are estimated by taking the average total smeared thickness in the side panels and multiplying this by the surface area of these shells, which are sized elsewhere in the Initiator. Multiplication with the composite material density consecutively gives the mass.

3

Sizing Methods for Composite Structure

Using the internal loads computed from the boom method and load cases, each structural element can be sized to carry the applied loads. In order to do this, just like for metal, the fuselage is divided into sections in the longitudinal direction, where each section is in between two frames. A frame spacing of 0.5 m is assumed (or another value specified by the user), then it is computed how many frames that would give (rounding to the nearest lower integer value) and finally, the frame spacing is recomputed using the integer amount of frames.

Each section comprises of a top arc, side arc and bottom arc, as well as the ceiling, wall and floor members of the trapezoid structure. Each of these will be sized separately using the methods outlined in this chapter.

First, a review of Classical Lamination Theory (CLT) is given, which is used to represent the material properties of a fiber composite laminate. Consecutively, the sizing criteria used for the (flat) skin panels, stringers and sandwich plates are given in that order. Following that, the routines for programmatically determining the stacking sequence and dimensions of each of these three members is discussed. Finally, a frame sizing routine is discussed.

3.1. Classical Lamination Theory

Prediction of the structural behavior of composites can be divided into two areas: stiffness response and strength response. Unlike metals, fiber composites exhibit orthotropic or even anisotropic behavior. Therefore, prediction of the strength is rather complicated, while the stiffness can be fairly accurately be predicted using Classical Lamination Theory (CLT).

3.1.1. Stiffness

A laminate is constructed by bonding several laminae on top of each other, with a certain stacking sequence, i.e. different fiber orientation for each ply (lamina) in a certain order. Classical Lamination Theory can be used to determine the stress-strain relation for a lamina and laminate, as described by Jones [20].

For an orthotropic material under plane stress, the stress-strain relations in principal material coordinates is given by:

$$\begin{bmatrix} \sigma_1 \\ \sigma_2 \\ \tau_{12} \end{bmatrix} = \begin{bmatrix} Q_{11} & Q_{12} & 0 \\ Q_{12} & Q_{22} & 0 \\ 0 & 0 & Q_{66} \end{bmatrix} \begin{bmatrix} \epsilon_1 \\ \epsilon_2 \\ \gamma_{12} \end{bmatrix} \tag{3.1}$$

where the constants are given by:

$$\begin{aligned} Q_{11} &= \frac{E_1}{1-\nu_{12}\nu_{21}} \\ Q_{22} &= \frac{E_2}{1-\nu_{12}\nu_{21}} \\ Q_{12} &= \frac{\nu 12 E_2}{1-\nu_{12}\nu_{21}} = \frac{\nu_{21}E_1}{1-\nu_{12}\nu_{21}} \\ Q_{66} &= G_{12} \end{aligned} \tag{3.2}$$

When describing the stresses in any other axis system, rotated with an angle θ from the principal axes, Equation 3.1 changes into:

$$\begin{bmatrix} \sigma_x \\ \sigma_y \\ \tau_{xy} \end{bmatrix} = \begin{bmatrix} \bar{Q}_{11} & \bar{Q}_{12} & \bar{Q}_{16} \\ \bar{Q}_{12} & \bar{Q}_{22} & \bar{Q}_{26} \\ \bar{Q}_{16} & \bar{Q}_{26} & \bar{Q}_{66} \end{bmatrix} \begin{bmatrix} \epsilon_x \\ \epsilon_y \\ \gamma_{xy} \end{bmatrix} \tag{3.3}$$

which can be rewritten in a short notation for ply k:

$$\{\sigma\}_k = \left[\bar{Q}\right]_k \{\epsilon\}_k \tag{3.4}$$

Before continuing, several statements have to be made regarding the following derivations:

- The laminae are presumed to be perfectly bonded, which is not necessarily an assumption but can be achieved in practice. This implies that the laminae can not slip relative to each other
- The normal to the middle surface remains straight and perpendicular to the middle surface, such that $\gamma_{xz} = \gamma_{yz} = 0$
- The aforementioned normal is of constant length, such that $\epsilon_z = 0$

The forces and moments on a laminate can be described by Equation 3.5 and Equation 3.6, respectively:

$$\begin{bmatrix} N_x \\ N_y \\ N_{xy} \end{bmatrix} = \sum_{k=1}^{N} \int_{z_{k-1}}^{z_k} \begin{bmatrix} \sigma_x \\ \sigma_y \\ \tau_{xy} \end{bmatrix}_k dz \tag{3.5}$$

$$\begin{bmatrix} M_x \\ M_y \\ M_{xy} \end{bmatrix} = \sum_{k=1}^{N} \int_{z_{k-1}}^{z_k} \begin{bmatrix} \sigma_x \\ \sigma_y \\ \tau_{xy} \end{bmatrix}_k z dz \tag{3.6}$$

Finally, these equations can be combined with Equation 3.3 to obtain the final stiffness equations for laminates:

$$\begin{bmatrix} N_x \\ N_y \\ N_{xy} \end{bmatrix} = [A] \begin{bmatrix} \epsilon_x^\circ \\ \epsilon_y^\circ \\ \gamma_{xy}^\circ \end{bmatrix} + [B] \begin{bmatrix} \kappa_x \\ \kappa_y \\ \kappa_{xy} \end{bmatrix} \tag{3.7}$$

$$\begin{bmatrix} M_x \\ M_y \\ M_{xy} \end{bmatrix} = [B] \begin{bmatrix} \epsilon_x^\circ \\ \epsilon_y^\circ \\ \gamma_{xy}^\circ \end{bmatrix} + [D] \begin{bmatrix} \kappa_x \\ \kappa_y \\ \kappa_{xy} \end{bmatrix} \tag{3.8}$$

where

$$\begin{aligned} A_{ij} &= \sum_{k=1}^{N} (\bar{Q}_{ij})_k (z_k - z_{k-1}) \\ B_{ij} &= \frac{1}{2} \sum_{k=1}^{N} (\bar{Q}_{ij})_k (z_k^2 - z_{k-1}^2) \\ D_{ij} &= \frac{1}{3} \sum_{k=1}^{N} (\bar{Q}_{ij})_k (z_k^3 - z_{k-1}^3) \end{aligned} \tag{3.9}$$

In Equation 3.9, $i, j = 1, 2, 6$ and A_{ij} are the extensional stiffnesses, B_{ij} are bending-extension coupling stiffnesses and D_{ij} are bending stiffnesses. When $[B]$ is nonzero, a laminate under tension would also bend and/or twist. A symmetric laminate, where both geometry and material properties are symmetric about the middle surface, $[B]$ is zero and hence no such coupling exists.

3.1.2. Strength

First-ply failure is analyzed using the Tsai-Wu failure criterion:

$$\frac{\sigma_x^2}{X^t X^c} + \frac{\sigma_y^2}{Y^t Y^c} - \sqrt{\frac{1}{X^t X^c Y^t Y^c}}\sigma_x \sigma_y + \left(\frac{1}{X^t} - \frac{1}{X^c}\right)\sigma_x + \left(\frac{1}{Y^t} - \frac{1}{Y^c}\right)\sigma_y + \frac{\tau_{xy}^2}{S^2} = 1 \tag{3.10}$$

Here, X^t, X^c, Y^t and Y^c denote the longitudinal and transverse ply strengths in tension and compression and S is the in-plane shear strength (all strengths should be provided in magnitude only, i.e. positive values). All of these strengths are decreased by three knockdown factors: elevated temperature wet, barely visible impact damage and material scatter [21]. The values for these knockdown factors are 0.8, 0.65 and 0.8, respectively [21].

The stresses are obtained by first using Equation 3.7 and Equation 3.8, rewritten in terms of the strains and curvature, with the applied loads as inputs. Then using the computed strains in Equation 3.3, the stresses in each ply can be computed.

As will become apparent later, laminates in the current study are subjected to N_x, N_y and N_{xy}. To compute the material failure loads when all three are applied simultaneously, a Newton-Raphson iterative method is applied. The three loads, N_x, N_y and N_{xy} are divided by the maximum of these three, giving ratios from 0 to 1. Thus, with F_{max} being the maximum (magnitude) of N_x, N_y and N_{xy}:

$$\begin{bmatrix} N_x & N_y & N_{xy} & M_x & M_y & M_{xy} \end{bmatrix}^T \cdot \frac{1}{F_{max}} = \begin{bmatrix} R_N \end{bmatrix}^T \tag{3.11}$$

where $[R_N]$ denotes the ratios of the loads to F_{max}. Note that M_x, M_y and M_{xy} are zero.

The Newton-Raphson method starts with an initial guess N_0, which is multiplied by $[R_N]$ to get a new load vector. Then the Tsai-Wu failure criterion is used to compute first-ply failure as described earlier. Now a residue is computed:

$$r_0 = R_{TW} - 1 \tag{3.12}$$

where R_{TW} is the Tsai-Wu failure criterion. A second load vector is computed using $N_0 + \delta_N$, which is a little offset from the original load. Now a residue r_δ is computed analogous to r_0. Now the derivative between these two residues can be computed:

$$\partial r = \frac{r_\delta - r_0}{\delta_N} \tag{3.13}$$

which provides a new guess for the next iteration:

$$N_i = N_0 - \frac{r_0}{\partial r} \tag{3.14}$$

This process repeats until r_0 is (close to) zero, which means the Tsai-Wu failure criterion was satisfied. The value for N_i obtained this way is now multiplied with $[R_N]$ to give a vector describing the critical loads for material failure.

3.2. Skin Panels

Skin panels are assumed to carry shear forces and a transverse pressure load. Under shear, no failure or buckling may occur. Under pressure, a maximum deflection is constraining. Moreover, a transverse pressure in a pressure vessel such as a fuselage results in hoop and longitudinal tensile stresses. Failure is checked with first-ply failure using the Tsai-Wu criterion as explained above. A panel with all possible loads acting on it is shown in Figure 3.1.

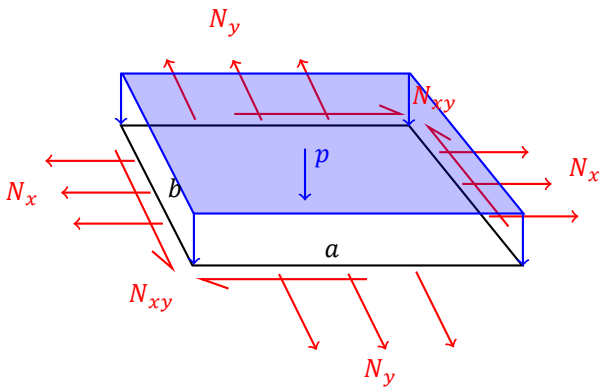

Figure 3.1: Forces acting on a panel

3.2.1. Shear Buckling

An approximate method to obtain the critical shear buckling load is presented in Ref. [21] and repeated here:

$$N_{xy,\text{crit}} = \frac{\frac{\pi^4 b}{a^3}}{\sqrt{\frac{14.28}{D1^2} + \frac{40.96}{D1D2} + \frac{40.96}{D1D3}}} \tag{3.15}$$

This equation holds when $0.5 \leq a/b < 1$, where a is the panel length and b the panel width. Moreover:

$$D1 = D_{11} + D_{22}\left(\frac{a}{b}\right)^4 + 2\left(D_{12} + 2D_{66}\right)\left(\frac{a}{b}\right)^2 \tag{3.16}$$

$$D2 = D_{11} + 81D_{22}\left(\frac{a}{b}\right)^4 + 18\left(D_{12} + 2D_{66}\right)\left(\frac{a}{b}\right)^2 \tag{3.17}$$

$$D3 = 81D_{11} + D_{22}\left(\frac{a}{b}\right)^4 + 18\left(D_{12} + 2D_{66}\right)\left(\frac{a}{b}\right)^2 \tag{3.18}$$

When $a/b = 0$ a different approach should be used, which will be explained directly hereafter. When $0 \leq a/b < 0.5$, the result should be linearly interpolated between the values for $a/b = 0$ and $a/b = 0.5$. Note that $a/b = 0$ is never achieved in practice and no threshold was set after which panels were deemed long, so the linear interpolation is executed for all panels with $a/b < 0.5$.
For long plates under shear ($a/b = 0$), a different approach is used. Now, $AR = a/L$ where L is, instead of b the length over which the buckling pattern is confined. Then the critical buckling load is given by:

$$\begin{aligned} N_{xy,\text{crit}} = \frac{\pi^2}{2AR^2a^2\tan\alpha}\Big[&D_{11}\left(1 + 6\tan^2\alpha AR^2 + \tan^4\alpha AR^4\right) \\ &+2\left(D_{12} + 2D_{66}\right)\left(AR^2 + AR^4\tan^2\alpha\right) + D_{22}AR^4\Big] \end{aligned} \tag{3.19}$$

This equation cannot be solved directly, because the parameters $\tan\alpha$ and L are not known. Taking the partial derivative with respect to the two unknowns and setting these equal to zero allows to solve for the critical buckling load:

$$\frac{\partial N_{xy,\text{crit}}}{\partial AR} = 0 \Rightarrow AR = \left[\frac{D_{11}}{D_{11}\tan^4\alpha + 2\left(D_{12} + 2D_{66}\right)\tan^2\alpha + D_{22}}\right]^{1/4} \tag{3.20}$$

$$\begin{aligned} \frac{\partial N_{xy,\text{crit}}}{\partial \tan\alpha} = 0 \Rightarrow\ &3D_{11}AR^4\tan^4\alpha + \left(6D_{11}AR^2 + 2\left(D_{12} + 2D_{66}\right)AR^4\right)\tan^2\alpha \\ &-\left(D_{11} + 2\left(D_{12} + 2D_{66}\right)AR^2 + D_{22}AR^4\right) = 0 \end{aligned} \tag{3.21}$$

3.2.2. Pressure

Under internal pressure, a hoop load and longitudinal load develop in the fuselage skin. Conventional fuselages are approximately circular cylinders, and analytical solutions for the developed stresses can

be obtained. Equation 2.20 gives the hoop stress, and the longitudinal stress is half that, as in Equation 2.21. In the present study, it is assumed that when looking at the individual skin panels, they are approximately elements in a circular cylinder and as such the same tensile stresses develop due to pressurization. Therefore, a tensile load is applied in both hoop and longitudinal direction and first-ply failure is computed. It should be remarked that this assumption leads to an underestimation of pressurization loads and as such a lighter structure is obtained. In fact, through this assumption, panels would not line up with each other entirely and the gaps would have to be modeled as flat pressure bulkheads to compensate for the mass reduction obtained otherwise.
As an additional failure mode, a maximum deflection of the skin panel is imposed when under pressure loading. Again, the methodology from Ref. [21] is used and summarized here. It is important to note that this theory is applicable to flat, rectangular panels, whereas the fuselage in reality consists of curved panels. However, each time a panel between two stringers and two frames is considered, such that the curvature may be small. Additionally, it is expected that flat panels under transverse pressure exhibit a larger deflection than curved panels and as such, the current approach is conservative.
Writing the out-of-plane deflection of a plate and the applied pressure load as a Fourier series, Equation 3.22 is obtained, which describes the center deflection of a monolithic panel under pressure p_0. Using an iterative method, m and n are increased until the computed deflection in the current iteration is within a certain margin of the previously computed deflection. It is assumed that $m = n$.

$$\delta = \sum\sum \frac{\frac{16p_0}{\pi^2 mn}}{D_{11}\left(\frac{m\pi}{a}\right)^4 + 2\left(D_{12} + 2D_{66}\right)\left(\frac{mn\pi^2}{ab}\right)^2 + D_{22}\left(\frac{n\pi}{b}\right)^4} \sin\frac{m\pi}{2}\sin\frac{n\pi}{2} \tag{3.22}$$

3.3. Stringers

Stringers are analyzed using the exact same procedure as described in Ref. [22]. Only C-stringers have been modeled in the present study. However, any other shape of stringer is also possible with slight modifications to the code.
Figure 3.2 shows that all three flanges can have different widths, thicknesses and layups. However, properties of the entire cross-section are required to perform the structural analysis. The Young's modulus E_i of flange i can be computed using:

$$E_i = \frac{1}{(a_{11})_i t_i} \tag{3.23}$$

The bending stiffness of the entire stringer then can be computed as follows:

$$EI_{\text{eq}} = \sum_i (EI)_i = \sum_i E_i \left[\frac{(\text{width})_i (\text{height})_i^3}{12} + A_i d_i^2\right] \tag{3.24}$$

The equivalent axial stiffness can simply be computed using:

$$EA_{\text{eq}} = \sum_i (EA)_i = \sum_i E_i A_i \tag{3.25}$$

As will become clear later, the current weight estimation method only takes into account bonded stringers. Therefore, the inter-rivet buckling failure is not discussed here. It should be noted, though, that inter-rivet buckling is taken into account in the computer program and therefore fastened stringers are also a possibility if the designer/researcher wants to analyze these.

3.3.1. Crippling

Flanges of a stringer feature a local stability failure mode, called crippling, where the flange buckles locally under compression. A semi-empirical approach is used, based on Ref. [21]. As can be seen in Figure 3.2, the web is analyzed as a no-edge-free (NEF) member, while the top and bottom flanges are analyzed as one-edge-free (OEF) members.

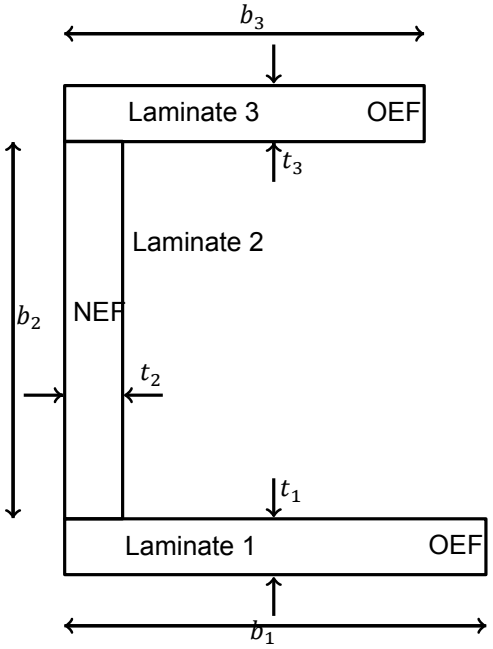

Figure 3.2: Stringer cross-section

For OEF members, the following equation can be used to compute the critical crippling load.

$$N_{x,i}^{\text{crit,crp}} = \frac{2.151 N_{x,i}^{\text{crit,mat}}}{\left(\frac{b_i^{\text{crp}}}{t_i}\right)^{0.717}} \tag{3.26}$$

Failure only occurs when $b_i^{\text{crp}} \leq 2.91 t_i$, otherwise failure is dictated by material failure.
Similarly, the following equation gives the critical crippling load for NEF members, where a flange is only crippling sensitive when $b_i^{\text{crp}} \leq 11.07 t_i$.

$$N_{x,i}^{\text{crit,crp}} = \frac{14.92 N_{x,i}^{\text{crit,mat}}}{\left(\frac{b_i^{\text{crp}}}{t_i}\right)^{1.124}} \tag{3.27}$$

3.3.2. Column Buckling

Column buckling load under compression is given by:

$$P_{\text{crit}} = \frac{c\pi^2 EI}{L^2} \tag{3.28}$$

where the buckling constant c can attain different values depending on the boundary conditions of the beam. For the present study, a value of 1.0 was used, which corresponds to pinned boundary condition on both beam ends.

3.4. Sandwich Panels

A sandwich panel consists of two facesheets and a core of, for example, honeycomb material. The ABD matrices of the facesheets can be determined using CLT, since these are just normal laminates. However, the sandwich in its entirety has a different *D* matrix, which can be computed using the following equation:

$$D_{ij} = 2D_{ij,f} + 2A_{ij,f}\left(\frac{t_c + t_f}{2}\right)^2 \tag{3.29}$$

With this new *D* matrix, the failure modes of a sandwich panel can be computed. First of all, there is global buckling under compression. Secondly, shear buckling and buckling under the combined

load case. Thirdly, sandwich wrinkling under compression and shear is taken into account. Sandwich crimping is the final failure mode. The loads applied to sandwich panels are the same as for monolithic panels, so refer to Figure 3.1 for visualization of these loads. Do note that only half of the applied N_x, N_y and N_{xy} need to be carried by the separate face sheets.
Since sandwich panels are most likely to be used for the trapezoidal structure, a transverse load due to passenger weight needs to be accounted for. The same analysis is used as for monolithic panels, i.e. Equation 3.22 is used to compute the panel deflection, which is constrained by a user-defined maximum.

3.4.1. Buckling

Buckling of the entire sandwich panel is computed using:

$$N_{x,\text{crit}} = \frac{N_{E,\text{crit}}}{1 + \frac{N_{E,\text{crit}}}{t_c G_c}} \tag{3.30}$$

where $N_{E,\text{crit}}$ is given by:

$$N_{E,\text{crit}} = \frac{\pi^2}{a^2}\left[D_{11}m^2 + 2\left(D_{12} + 2D_{66}\right)AR^2 + D_{22}\frac{AR^4}{m^2}\right] \tag{3.31}$$

Here, m is an integer value that minimizes the right hand side of the equation. Equation 3.31 is therefore computed for a range of values for m, and the minimum resulting $N_{E,\text{crit}}$ is used. For shear buckling, the following equation is used:

$$N_{xy,\text{crit}} = \frac{(G_{xz} + G_{yz})t_c}{2 + \frac{(G_{xz}+G_{yz})t_c}{N_{xy,\text{crit,pan}}}} \tag{3.32}$$

where $N_{xy,\text{crit,pan}}$ is computed as was done for monolithic panels in Equation 3.15 and Equation 3.19. When both a compressive load and a shear load are applied, the following interaction curve is used:

$$R_{\text{buck}} = \frac{N_x}{N_{x,\text{crit}}} + \left(\frac{N_{xy}}{N_{xy,\text{crit}}}\right)^2 \tag{3.33}$$

which indicates buckling failure when the right hand side becomes larger than 1.

3.4.2. Wrinkling

Three wrinkling modes are possible: symmetric, asymmetric and mixed mode wrinkling. In the present analysis, only the first two are taken into account. One can either take into account waviness (which leads to wrinkling at a lower load) or not. Logically, the first approach is more conservative. Therefore, this approach was used in the present work. However, this approach may also be too conservative, so the method that does not take into account waviness is also discussed here.

Without Waviness For symmetric wrinkling, when the following holds:

$$t_c \geq 1.817 t_f \left(\frac{E_f E_c}{G_{xz}^2}\right)^{1/3} \tag{3.34}$$

the critical wrinkling load is:

$$N_{x,\text{wr}} = 0.91 t_f (E_f E_c G_{xz})^{1/3} \tag{3.35}$$

and otherwise the critical wrinkling load is given by:

$$N_{x,\text{wr}} = 0.816\sqrt{\frac{E_f E_c t_f^3}{t_c}} + G_{xz}\frac{t_c}{6} \tag{3.36}$$

For asymmetric wrinkling, when:

$$t_c \geq 3 t_f \left(\frac{E_f E_c}{G_{xz}^2}\right)^{1/3} \tag{3.37}$$

the critical wrinkling load is:

$$N_{x,\mathrm{wr}} = 0.51 t_f (E_f E_c G_{xz})^{1/3} + \frac{G_{xz} t_c}{3} \tag{3.38}$$

and otherwise:

$$N_{x,\mathrm{wr}} = 0.59 t_f^{3/2} \sqrt{\frac{E_f E_c}{t_c}} + 0.378 G_{xz} t_c \tag{3.39}$$

With Waviness For symmetric wrinkling the critical load is given by:

$$N_{x,\mathrm{wr}} = 0.43 t_f (E_f E_c G_{xz})^{1/3} \tag{3.40}$$

and for asymmetric wrinkling by:

$$N_{x,\mathrm{wr}} = 0.33 t_f (E_f E_c G_{xz})^{1/3} + \frac{G_{xz} t_c}{3} \tag{3.41}$$

Although only for thin cores asymmetric wrinkling occurs [21], both modes are used in the current analysis, since very thin cores may lead to an optimal design for certain panels in the fuselage structure. Therefore, the lowest critical load (either symmetric or asymmetric) is used as critical wrinkling load.
Wrinkling under shear load can be analyzed analogous to the presented wrinkling analysis, because a shear load can be decomposed into a compressive and tensile load. Only the core shear stiffnesses and face Young's modulus should be computed as if the panel were rotated by 45°. The core shear stiffnesses can be computed as:

$$G_{\bar{x}z} = \frac{G_{yz} + G_{xz}}{2} \tag{3.42}$$

$$G_{\bar{y}z} = \frac{G_{yz} + G_{xz}}{2} \tag{3.43}$$

For wrinkling under combined compression and shear, again an interaction curve similar to Equation 3.33 is used.

3.4.3. Crimping

Crimping is similar to asymmetric wrinkling and under compression can be shown to give a critical load as given by:

$$N_{x,\mathrm{crimp}} = t_c G_c \tag{3.44}$$

Under shear load, the critical crimping load is given by:

$$N_{xy,\mathrm{crimp}} = t_c \sqrt{G_{xz} G_{yz}} \tag{3.45}$$

3.5. Sizing Routines

The equations presented in the previous sections need to be implemented into routines that determine the laminate(s) of the structural components, depending on applied loads. Figure 3.3 shows what inputs should lead to what outcome for the three structural components considered in the present work.
Evidently from Figure 3.3, monolithic (skin) panels take shear, line and pressurization loads, stringers take longitudinal loads and sandwich panels have to resist all of these. Sizing processes for the monolithic panels and stringers were developed in Ref. [22], but several modifications were made to these processes. Therefore, an explanation of these processes is presented here. The first and most important modification is the addition of the sandwich panel. Moreover, sizing of the monolithic panels was modified to include a transverse pressure load.

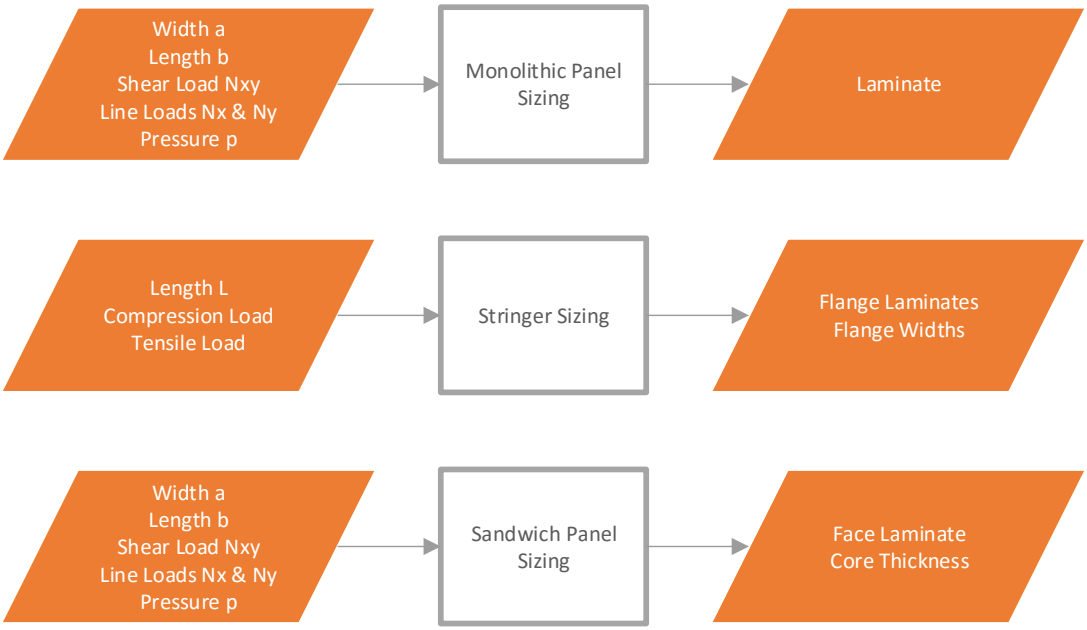

Figure 3.3: Input and output for sizing procedures

3.5.1. Monolithic Plate Optimization

Optimization of monolithic plates is performed almost identically to the Additive Lay-up Generation Optimizer (ALGO) routine developed in Ref. [22]. However, the pressurization loads as discussed earlier were added to the process. Figure 3.4 shows the optimization process. Reference A points to the flowchart in Figure 3.5, which in turn references back to B in Figure 3.4.

As a start, a $[\pm 45/0/90]_s$ laminate is used. Then this laminate is analyzed, which means all failure modes are checked. If no failure is found, the laminate is valid and the optimization ends. If not, Figure 3.5 shows how a ply is selected which should be added to the laminate. Additionally, in the second and later iterations, four alternatives for the main laminate are created: one with a midply (if the main laminate has none), or one without a midply if the main laminate has one, the main laminate with an additional ply (in the symmetric part) and as a fourth alternative the main laminate with an additional ply in the symmetric part and a midply. These alternatives may result in a more efficient laminate than the main laminate, simply because they add some thickness. All five (including the main laminate) designs are analysed and the main laminate is replaced with the thinnest option capable of withstanding the loads. If no designs can handle the loads, the main laminate is modified again as depicted in Figure 3.5. When the plate is found to be shear buckling critical, it is not directly evident what ply should be added. Therefore, each *D*-term is perturbed by 1% and the shear buckling calculation is performed for each perturbation separately. The term that gives the largest increase in critical shear buckling load determines the ply that should be added in the next iteration.

Finally, as can be seen in Figure 3.4, when a suitable laminate has been found, an iterative technique starts that tries to remove as many plies from the laminate without making it fail. Since the optimization may jump from one critical failure mode to another, some redundancy may develop in the laminate. This process aims to minimize the weight penalty associated with that.

3.5.2. Stringer Optimization

The Enumerative Lay-up Family Optimizer (ELFO) from Ref. [22] was used to optimize a stringer for a maximum tensile and maximum compression load simultaneously, without any modifications to this method. ELFO aims to include as many 0 plies as possible, since only axial loads are considered for stringers. Furthermore, basic laminate design rules are used, including but not limited to: balanced and symmetric laminates, 10% rule and maximum ply stack rule.

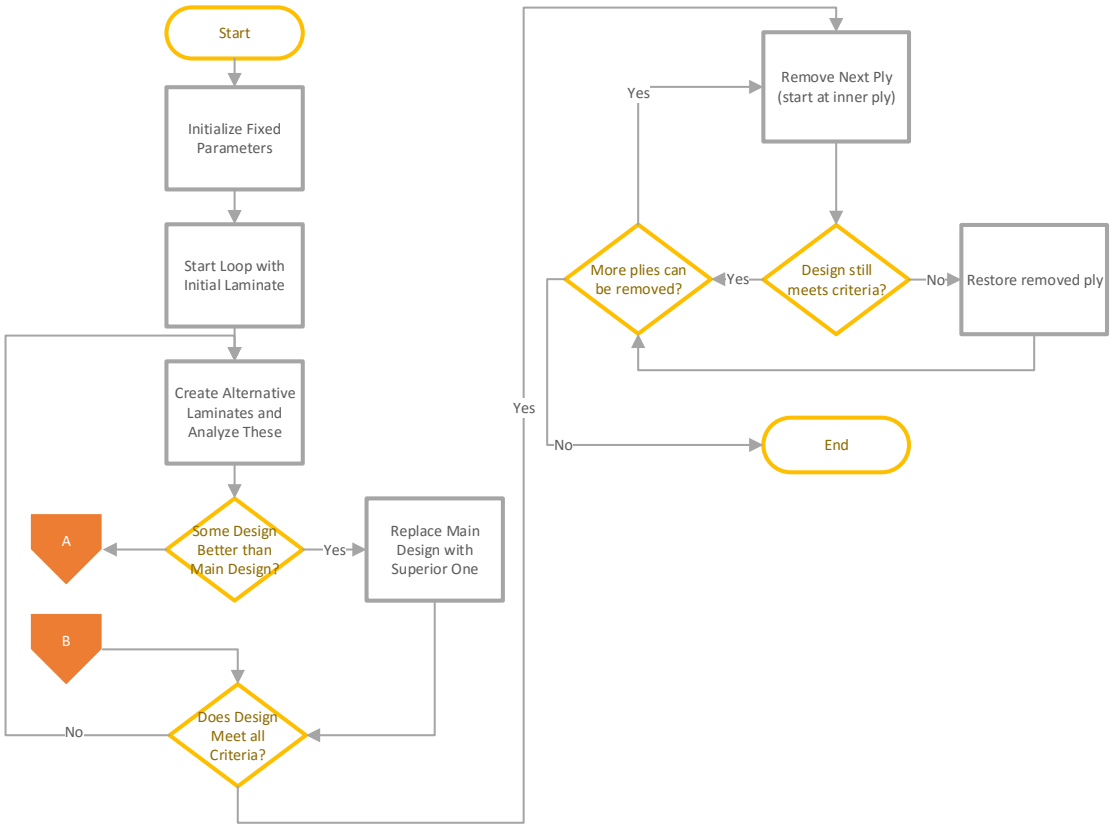

Figure 3.4: Optimization process for composite panels

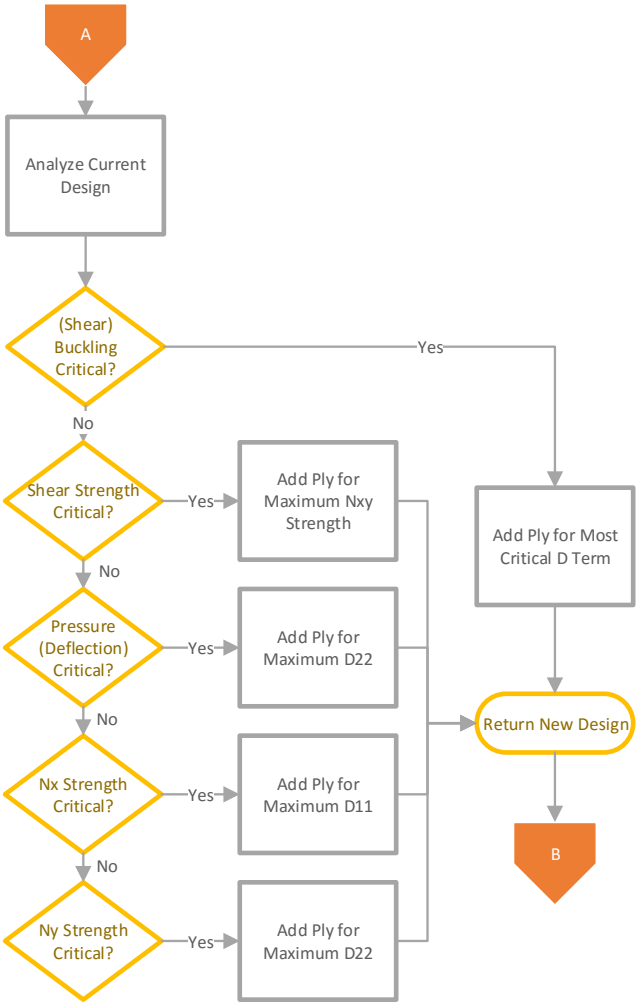

Figure 3.5: Ply addition for composite panels

ELFO generates a family of laminates, which are subsequently applied to each member (flange or web) of the stringer under consideration. Each member can have a different laminate, and a maximum difference in amount of plies is set, such that excessive ply-drops from one member to another are prevented. With the laminates fixed, ELFO starts a gradient based optimization routine to determine the optimal flange widths (i.e. minimum weight, while satisfying failure constraints). When all different combinations of layups have been analyzed, the lightest design meeting the criteria is chosen, concluding the procedure. A flowchart of the described process can be seen in Figure 3.6.

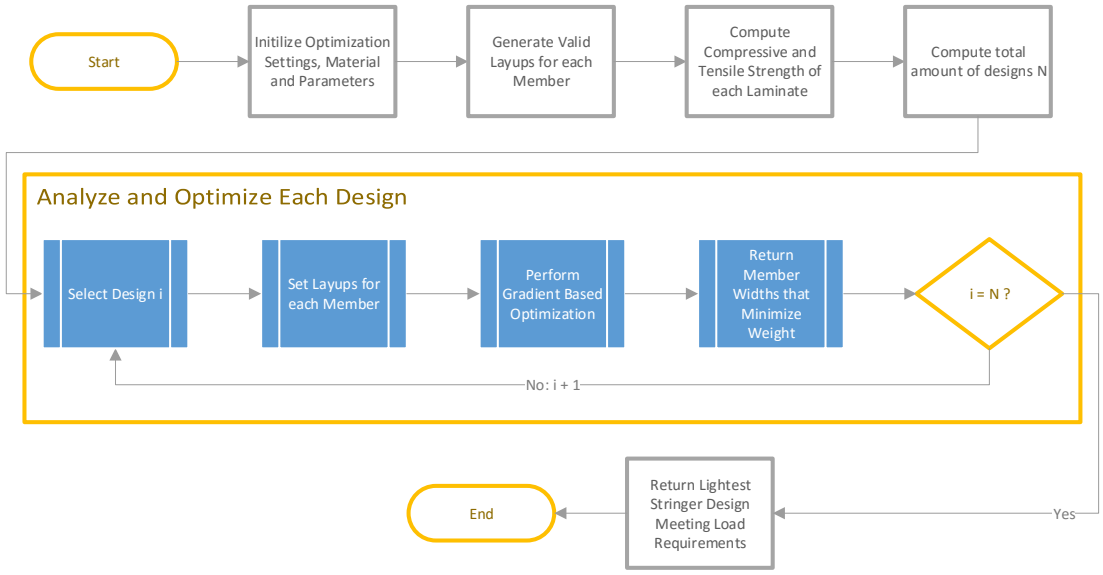

Figure 3.6: Optimization process for composite stringers

3.5.3. Sandwich Panel Optimization

The optimization process for sandwich panels (see Figure 3.4 again) is identical to the Additive Lay-up Generation Optimizer (ALGO) routine as presented for panels. However, Reference A now points to Figure 3.7. The process for determining the failure criteria is shown in Figure 3.7 and is different from Figure 3.5. Logically, different failure modes are present. Moreover, analysis of a sandwich panel is not simply computing the failure criteria as was done for monolithic panels. For sandwich panels, a core thickness optimization loop is performed each time the face laminate is analyzed. This loop increases the core thickness from a set minimum (0.1 mm) to a set maximum (200 mm), or until all failure criteria are met.

3.6. Frames

Frames transfer loads from attached components to the fuselage skin and prevent global instability of the fuselage. Furthermore, they prevent expansion of the fuselage skin under pressurization loads. Frames are statically indeterminate structures and the multitude of loads make their analysis and sizing difficult. Finally, the unconventional shape of the oval frames rule out use of simple empirical solutions. The elastic center method as presented by Bruhn [23] was used for sizing of the fuselage frames. As such, the shear forces from the boom method can be taken into account to compute the internal bending moment in a frame. This moment then is used to size a cross-section that minimizes the weight while preventing material failure and crippling. Finally, a minimum cross-sectional area moment of inertia results from the Shanley criterion, in order to prevent global buckling of the fuselage structure. This section presents this shortly described procedure in more detail.

The elastic center method is a method to analyze a statically indeterminate structure. For a closed section like a frame, a virtual cut is made, and one edge is assumed to be attached to a rigid arm connecting it to the so-called elastic center. The other end (of the section, where the cut was made) is

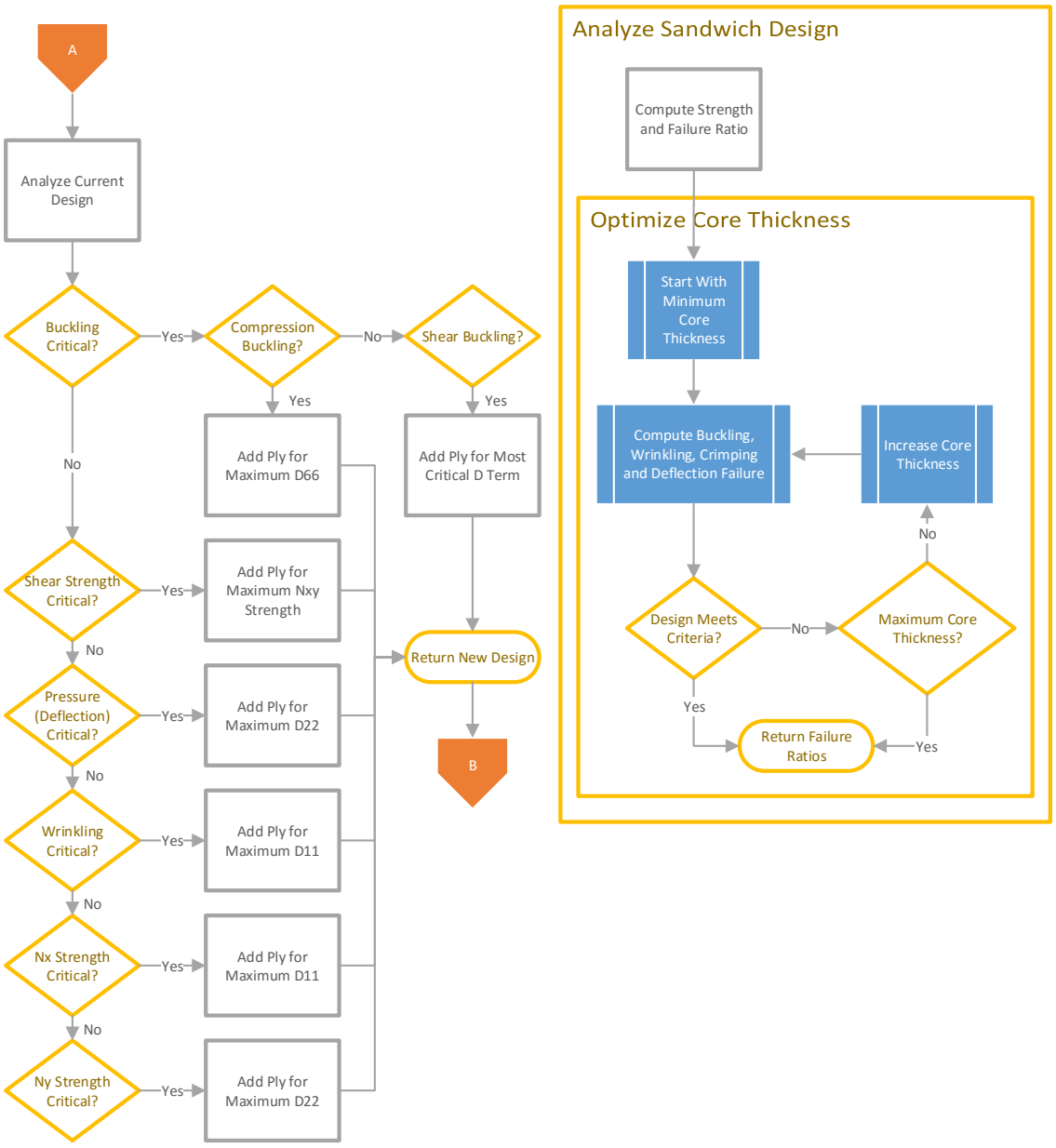

Figure 3.7: Ply addition and core thickness for composite sandwich panels

assumed to be clamped.

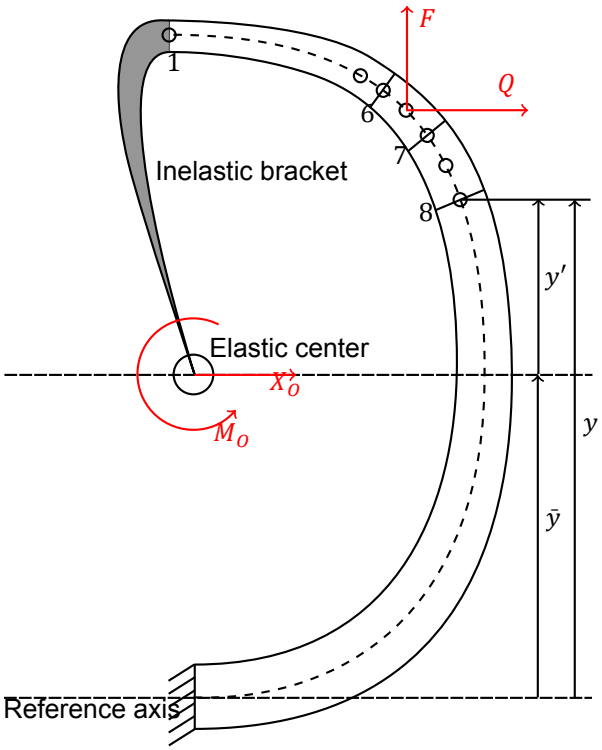

Figure 3.8: Frame section for elastic center method

Since the frames considered here are symmetrical around the vertical axis, only half of the section is considered, which is analyzed as a curved beam. The cut in the cross-section is made exactly at the top of the cross-section. Considering a section of this curved beam, as shown in Figure 3.8, Q and F are the applied forces and V, H and M are the internal forces and bending moment. Starting from the free end and working towards the clamped end, Equation 3.46, Equation 3.47 and Equation 3.48 relate the internal forces to the external forces.

$$V_2 = V_1 + F \tag{3.46}$$
$$H_2 = H_1 + Q \tag{3.47}$$
$$M_2 = M_1 + V_1 d - H_1 h + Fa - Qb \tag{3.48}$$

The horizontal and vertical forces applied are the components of the shear force acting on the frame, which is computed by taking the difference in shear flow of the two adjacent sections of skin, analogous to Megson [16].
Now the assumption of the rigid arm connected to the free end of the beam comes into play, which introduces an additional horizontal and vertical force to the entire beam, as well as a bending moment. However, first the position of the elastic center has to be found. Since the cross-section is symmetrical around the vertical axis, the elastic center lies on the vertical axis and only the vertical location of the elastic center should be found. This is done by assuming a reference axis ($y = 0$ in this case) and computing the product of elastic weight w with the arm of a section to the reference axis y', where $w = \mathrm{d}s/I$ and $\mathrm{d}s$ the length of a section. Then the location of the elastic center $\bar{y}$ is given by:

$$\bar{y} = \frac{\sum w y'}{\sum w} \tag{3.49}$$

Then the elastic moment of inertia (called I_x for convenience) is given by:

$$I_x = \sum \frac{y^2 \mathrm{d}s}{EI} \tag{3.50}$$

where y is the arm from a section on the cross-section to the elastic center location $\bar{y}$, see Figure 3.8. Calling the internal bending moments computed from Equation 3.48 M_S, the concept of elastic moments Φ_S are introduced, which are computed as follows:

$$\Phi_S = \frac{M_S \mathrm{d}s}{EI} \tag{3.51}$$

Now the moment and horizontal force in the elastic center can be computed. Note that a vertical force is absent there due to symmetry.

$$M_O = \frac{-\sum \Phi_S}{\sum \mathrm{d}s/EI} \tag{3.52}$$

$$X_O = \frac{\sum \Phi_S \cdot y}{I_x} \tag{3.53}$$

Finally, the internal bending moments in the frame are given as:

$$M = M_S + M_O - X_O \cdot y \tag{3.54}$$

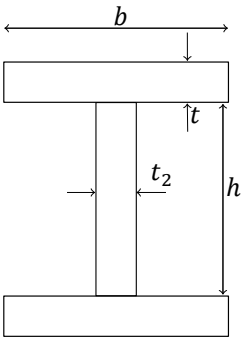

Figure 3.9: Frame cross-section

A gradient-based optimization routine is used to optimize the cross-section for each section of each frame. As a constraint on the minimum cross-sectional area moment of inertia, the Shanley criterion is used:

$$EI_{\mathrm{req}} = \frac{C_f R M}{8 h L_{\mathrm{fr}}} \tag{3.55}$$

The frame is checked for both material failure and crippling considerations. For metal frames, the Von Mises yield criterion is used to predict material failure:

$$\frac{\sqrt{\sigma_x^2 - \sigma_x \sigma_y + \sigma_y^2 + 3\sigma_{xy}^2}}{\sigma_{\mathrm{ult}}} < 1 \tag{3.56}$$

For composites the Tsai-Wu failure criterion is used as was presented in subsection 3.1.2.
For crippling in a metallic cross-section, the top flange (attached to the fuselage skin) is assumed to be a no-edge-free (NEF) flange with both sides clamped. The web is also assumed to be NEF, but with one side clamped and the other simply supported. Finally, the lower flange is approximated as a one-edge-free member with one edge simply supported. The general crippling formula for a metallic flange is given by:

$$\sigma_{\mathrm{crp}} = k\pi^2 \frac{E}{12(1-\nu^2)} \left(\frac{t}{b}\right)^2 \tag{3.57}$$

[23] where the constant k depends on the constraints of the flange. For the top flange $k = 6.98$, for the web $k = 5.42$ and for the lower flange $k = 0.43$.
Crippling failure occurs when:

$$\frac{\sigma_c}{\sigma_{\mathrm{crp}}} > 1 \tag{3.58}$$

where σ_c is the compressive stress acting on the flange.
Crippling failure for composite frames is determined exactly as was shown in subsection 3.3.1, with both the top flange and web being NEF members and the lower flange an OEF member.

3.7. Stiffened Trapezoid

Not always are sandwich panels desirable to build the trapezoidal structure. When cutouts need to be made in the trapezoid, for windows, doors and possibly overhead bins (on top of the ceiling member), stiffened panels may be more beneficial than sandwich panels. The same sizing methods can be used for a stiffened panel trapezoid as for the stiffened skin panels. However, a lateral compression force may act on certain members of the trapezoid, and since these are not aligned with the stringers, an additional beam is required that carries these loads. Such beams are connected to the frames and prevent buckling of the stiffened trapezoid panels. Sizing of these beams is done analogous to the stringer sizing outlined in this chapter.

4

Regression Analysis

Use of the procedure outlined in the previous chapter directly in the weight estimation method is prohibitive due to its computational time. Even though the method is much faster than a full-blown optimization, such as a genetic algorithm, a single panel or stringer may take from 0.1 s to little under a minute. Obviously, when several hundreds or even thousands of panels and stringers are sized this way, total computation time amounts to hours.

In order to use the results from the composite analysis, a surrogate modeling approach was adopted. This allows the relevant results (weight, axial and bending stiffness, thickness and/or cross-sectional area) to be modeled as function of the relevant parameters (panel dimensions, axial and/or transverse load and shear load, for example). Since such a model only maps input to output, the expensive detailed calculation does not have to be executed and the in-the-loop calculation time of the weight estimation method remains acceptable.

Neural networks are used in the current mass estimation method as surrogate models. Neural networks proved to be very capable of capturing the behavior of this specific problem. However, additionally, linear regression models were created as well, since these can be easily distributed using a mathematical description. This chapter discusses the results of both these approaches. Table 4.1 shows the ranges of inputs used to create the models as shown in Figure 3.3. It should be noted in advance that in order to use the following models, only values within these ranges should be used if an accurate result is to be expected. Even neural networks have difficulty in extrapolating their data.

The bounds for a and b were deduced from what seem to be logical sizes for panels in between frames and stringers. According to Kassapoglou [21], a minimum stringer pitch of 0.12 m provides a good weight/cost trade-off. The upper bound is somewhat arbitrary. The panel length depends on the frame spacing, which is assumed not to exceed 0.8 m. Since composite panels are used in the trapezoidal structure, and there the x-direction is along the pitch axis of the aircraft, the panel length is defined by the floor width and as such a length of 10 m was chosen.

The N_x and N_y bounds were selected based on loads applied by Ambur and Rouse [24], who dictate an ultimate load of 430 kN/m. In order to have some margin, a maximum load of 500 kN/m was chosen for these two loads. Even though this is already higher than the ultimate found in literature, this load is multiplied by the safety factor in the composite sizing routines, providing even more tolerance.

Table 4.1: Input values for structural components

Monolithic panel		
Input	Start	End
a [m]	0.25	0.8
b [m]	0.1	0.5
N_{xy} [kN/m]	0	1500
p [kPa]	0	100
N_y [kN/m]	0	500
N_x [kN/m]	$= N_y/2$	

Stringer		
Input	Start	End
L [m]	0.3	0.6
$N_{x,c}$ [kN]	0	2000
$N_{x,t}$ [kN]	0	2000

Sandwich panel		
Input	Start	End
a [m]	0.1	5.0
b [m]	0.1	0.8
N_x [kN/m]	0	500
N_y [kN/m]	0	500
N_{xy} [kN/m]	0	1500
p [kPa]	0	100

Additionally, shear load bounds were defined based on values encountered in the load calculations for several aircraft.
For an A320, the minimum cabin pressure (maximum cabin altitude) is at 2,400 m, corresponding to 75.2 kPa atmospheric pressure according to the ISA. The service ceiling is 12.5 km, where the outside pressure is 17.9 kPa. Therefore a differential pressure of 57.3 kPa acts on the fuselage skin. In terms of ultimate load, this differential pressure reaches 86 kPa and therefore a slightly higher upper limit was selected at 100 kPa. It should be noted that this is valid for most if not all aircraft, because the maximum cabin altitude is defined by regulations and the service ceiling will likely not be much higher than the 12.5 km used here.
Dividing each parameter range into a certain number of values, and optimizing for each possible combination of these values results in a huge set of designs that need to be analyzed. Reducing this amount of designs by limiting the range or increasing the step size reduces the fidelity of the modeling space and may exclude certain important effects. Therefore, Latin Hypercube Sampling is used to obtain an evenly spaced set of input values for which the structural sizing is performed.
Additionally, before the regression techniques presented in the next two sections were performed, the data was scaled. Since the values of data vary widely (thicknesses in the order of 10^{-3} and Young's modulus in the order of 10^{12}), this ensures that the relative importance of each predictor is appropriately taken into account and is not dominated by the absolute value a predictor or response has. The scaling technique used is called feature scaling and as Equation 4.1 shows, it scales each value to a [0,1] domain, referring to the ratio of the value to the range of the parameter (x' is the normalized value).

$$x' = \frac{x - \min(x)}{\max(x) - \min(x)} \tag{4.1}$$

For the neural networks, this scaling is not necessary, but it may make it easier to train. Conversely, for the linear regression and especially interpretation of the coefficients, scaling is of paramount importance.
The material properties used for the surrogate models are listed in Table 4.2. If different materials are to be used in the weight estimation method, one has to modify these values and create new surrogate models with these materials. How that works is explained in detail in Appendix A.

Table 4.2: Material properties used for surrogate models

UD material		
Property	Value	Unit
E_x	137.9	GPa
E_y	11.7	GPa
ν_{xy}	0.29	-
G_{xy}	4.82	GPa
t_{ply}	0.1524	mm
X^t	2068	MPa
X^c	1723	MPa
Y^t	96.5	MPa
Y^c	338	MPa
S	124	MPa
ρ	1609	kg/m^3

Core material		
Property	Value	Unit
E_c	131	MPa
G_{xz}	41.4	MPa
G_{yz}	20.7	MPa
ρ	48.2	kg/m^3

4.1. Linear Least Squares Regression

Linear regression uses least-squares to fit the model to data. It assumes a linear relationship between the dependent variable and the coefficients of the function describing that variable (usually a polynomial). A linear model can be written as:

$$\bar{y} = \bar{X}\bar{\beta} + \bar{\epsilon} \tag{4.2}$$

where:

$$\bar{y} = \begin{pmatrix} y_1 \\ \vdots \\ y_n \end{pmatrix} \tag{4.3}$$

$$\bar{X} = \begin{pmatrix} x_{11} & \cdots & x_{1p} \\ \vdots & \ddots & \vdots \\ x_{n1} & \cdots & x_{np} \end{pmatrix} \tag{4.4}$$

$$\bar{\beta} = \begin{pmatrix} \beta_1 \\ \vdots \\ \beta_p \end{pmatrix} \tag{4.5}$$

$$\bar{\epsilon} = \begin{pmatrix} \epsilon 1 \\ \vdots \\ \epsilon_n \end{pmatrix} \tag{4.6}$$

In the above equations, n is the number of data points and p is the amount of independent variables or predictors.
The least-squares solution to this problem is a vector $\bar{b}$, which is an estimation of the vector $\bar{\beta}$. It can be computed using:

$$\bar{b} = \left(\bar{X}^T \bar{X}\right)^{-1} \bar{X}^T \bar{y} \tag{4.7}$$

Predicting values of $\bar{y}$ then simply becomes:

$$\hat{y} = \bar{X}\bar{b} \tag{4.8}$$

where $\hat{y}$ denotes that it is a prediction from the model.
Important to note is that linear regression does not necessarily mean that the model is linear in the predictor variables. Any (polynomial) function can be used with this type of regression, since the term linear refers to that the model is linear with respect to the coefficients $\bar{\beta}$ of the model.
For each response, an initial model was assumed based on engineering sense and the failure criteria as outlined in chapter 3. Using that model, linear regression is performed using a Matlab routine called `fitlm`. A stepwise linear regression procedure was executed for each of these models, using the Matlab routine `step`, to improve the prediction. Based on the p-value of each predictor, which indicates the significance of a certain predictor, terms are added or removed from the model to improve the fit. These modified linear regression models generally produce a better prediction of the response variable than the original model.
In order to understand the results presented in the following three sections, the Wilkinson notation is shortly discussed. Wilkinson notation describes the factors in models, with Aˆk (with k a positive integer) meaning a factor to the power k, A*B meaning the product of A and B, but also the terms A and B separately and, finally, A:B meaning the product of A and B only. With a - sign, the following term is excluded from the model (for example, A*B*C - A:B:C would include the terms A, B, C, A:B, A:C and B:C).

4.1.1. Skin Panels

For the monolithic skin panels, three responses have to be predicted: weight, thickness and the Young's modulus (in the length direction, which is aligned with the fuselage longitudinal axis). The independent variables are the length and width of the panel, the applied shear load, transverse pressure and the hoop line load. The axial line load is not included, since this is exactly half the hoop line load, based on the analytical formula for membrane loads in a circular cylinder. The resulting linear regression coefficients are shown in Table 4.3.
Inspecting Table 4.3, it can be concluded that all loads have a more or less equal effect on weight, thickness and Young's modulus. However, for the weight, it is evident that the panel area ($L : W$) and pressure times the panel area ($L : W : p$) are the most sizing parameters. In terms of thickness, the shear load (N_{xy} and related terms) has a significant influence and again the term $L : W : p$ appears sizing. The Young modulus is mainly determined by its intercept value, which indicates there is little deviation in the Young's modulus response. Additionally, the model performs rather poorly, with a high root-mean-squared error and low R-squared. This is attributed to the discrete response of the Young's modulus.
The performance of the linear regression models in Table 4.3 can be compared to the neural networks modeling the same data in Figure 4.1 and Figure 4.2. The residuals are the predicted response minus the actual response value for that design. Frequency is the amount of times a certain residual is

Table 4.3: Regression models for monolithic panel

Weight	
Predictor	Coefficient
(Intercept)	-0.005651
L	0.012173
W	-0.19099
N_{xy}	0.05416
p	0.12869
N_y	0.015108
$L:W$	0.28119
$L:N_{xy}$	0.072602
$L:p$	-0.11328
$L:N_y$	0.024681
$W:p$	0.065117
$N_{xy}:p$	-0.10847
$p:N_y$	-0.040007
L^2	-0.033441
W^2	0.27371
N_{xy}^2	0.02327
p^2	-0.061339
$L:W:N_{xy}$	-0.031432
$L:W:p$	0.59799
RMSE	0.0247
R-squared	0.977

Thickness	
Predictor	Coefficient
(Intercept)	-0.080721
L	0.14307
W	0.041909
N_{xy}	0.50351
p	0.2528
N_y	0.10449
$L:W$	0.14214
$L:p$	-0.10001
$W:N_{xy}$	-0.3556
$W:p$	0.36016
$W:N_y$	-0.074105
$N_{xy}:p$	-0.26575
$p:N_y$	-0.065339
L^2	-0.1476
W^2	0.216
N_{xy}^2	-0.15517
p^2	-0.096116
$L:W:N_{xy}$	-0.072308
$L:W:p$	0.46325
N_{xy}^3	0.19727
RMSE	0.0397
R-squared	0.951

E-modulus	
Predictor	Coefficient
(Intercept)	0.47881
L	-0.094144
W	-0.14212
N_{xy}	-0.13604
p	-0.44394
N_y	-0.061836
$L:W$	-0.012931
$L:p$	0.031517
$L:N_y$	-0.077556
$W:N_{xy}$	0.33761
$W:p$	-0.24639
$N_{xy}:p$	0.307
$N_{xy}:N_y$	0.096899
$p:N_y$	0.10574
L^2	0.14127
N_{xy}^2	-0.11578
p^2	0.25078
$L:W:p$	-0.18054
RMSE	0.101
R-squared	0.439

observed in the entire data set. Moreover, the residuals are taken on the non-dimensional responses, such that they can be interpreted as a percentage (when multiplied by 100). The neural networks have smaller residuals and can therefore predict the data better, but the linear regression models also have satisfactory performance.

4.1.2. Stringers

The main failure criteria for the stringers are the crippling criteria, which are linear in the applied compression load. However, material failure produces a quadratic term. Moreover, the stringer length appears as a quadratic term in the column buckling equation. Therefore, the initial model for the stringers is taken as a quadratic function in all three predictor variables. The resulting models are presented in Table 4.4.

Table 4.4: Regression models for C-shape stringer

Weight	
Predictor	Coefficient
(Intercept)	0.012449
L	0.0237
$N_{x,t}$	0.22002
$N_{x,c}$	0.22122
$L:N_{x,t}$	0.11853
$L:N_{x,c}$	0.35877
$N_{x,t}:N_{x,c}$	-0.54752
L^2	0.022379
$N_{x,t}^2$	0.1366
$N_{x,c}^2$	0.43064
RMSE	0.0282
R-squared	0.98

Axial stiffness EA	
Predictor	Coefficient
(Intercept)	0.041409
$N_{x,t}$	0.37273
$N_{x,c}$	0.54427
$N_{x,t}:N_{x,c}$	-0.73508
$N_{x,t}^2$	0.18761
$N_{x,c}^2$	0.5652
RMSE	0.0349
R-squared	0.979

Cross-sectional area A	
Predictor	Coefficient
(Intercept)	0.043999
$N_{x,t}$	0.36518
$N_{x,c}$	0.5292
$N_{x,t}:N_{x,c}$	-0.72362
$N_{x,t}^2$	0.1865
$N_{x,c}^2$	0.57527
RMSE	0.034
R-squared	0.98

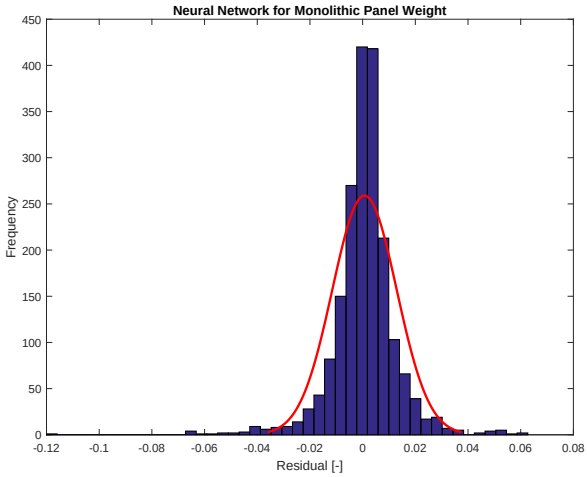

(a) Neural network

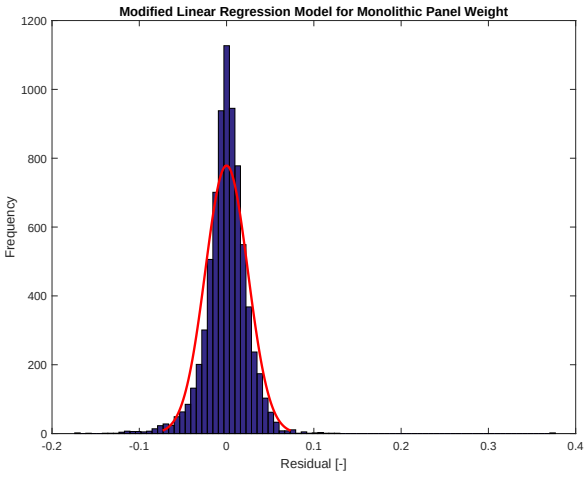

(b) Linear regression model

Figure 4.1: Models predicting weight of monolithic panel

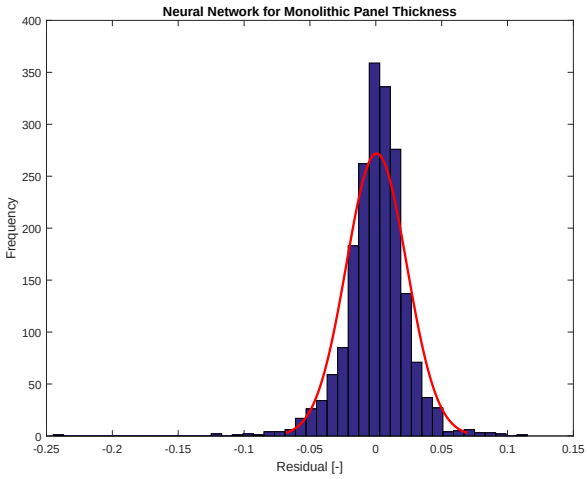

(a) Neural network

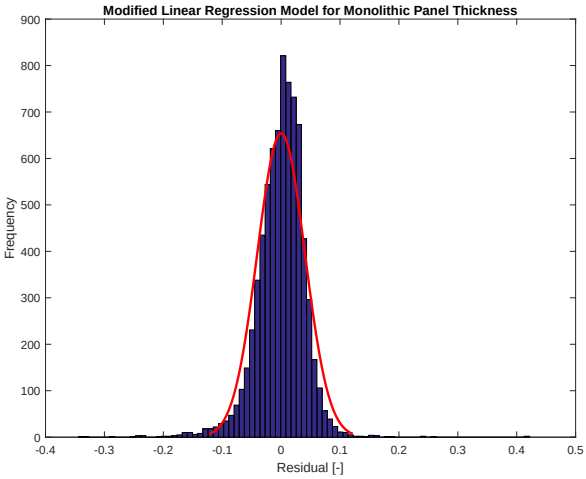

(b) Linear regression model

Figure 4.2: Models predicting thickness of monolithic panel

What becomes immediately apparent from Table 4.4 is that the stringer length does not play a role for the axial stiffness and cross-sectional area of the stringer. This would mean that indeed crippling is the constraining failure mode, which does not depend on the stringer length, but only on its cross-sectional properties.

Another interesting observation is that the product $N_{x,t}$:$N_{x,c}$ for all three models has a negative coefficient. From a physical point of view, it does not make much sense for this term to exist, since the tensile and compression load never occur simultaneously in the same stringer. However, the stringer is sized for both these loads. One would expect that sizing for both tension and compression would actually lead to a less efficient design and, therefore, a heavier design. As such, the product term may be interpreted as a compensation for the compression and tension loads existing simultaneously in the model.

Finally, the magnitude of coefficients including $N_{x,c}$ are generally higher than those including $N_{x,t}$, which indicates a stronger correlation between failure and compression load than failure due to tension. This makes perfect sense, since buckling failure occurs earlier than material failure, generally.

From Figure 4.4, Figure 4.5 and Figure 4.6 it can be seen that the linear regression models perform much worse than the neural networks modeling the same data. Not only are the residuals for the latter at least 10 times smaller, but also the shape of the histogram resembles a normal distribution (the red lines) better, which indicates that the residuals are evenly distributed around zero. However, the linear

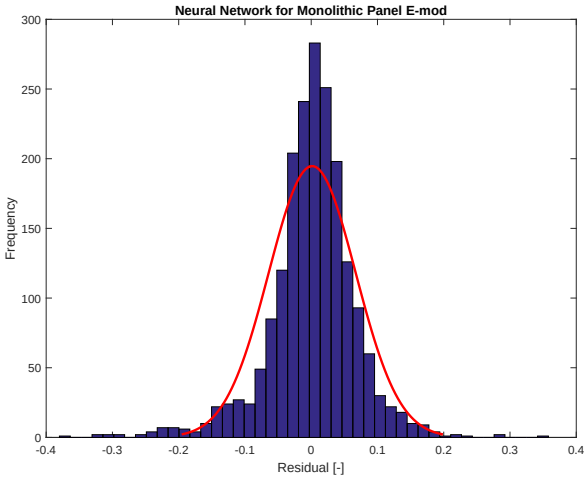

(a) Neural network

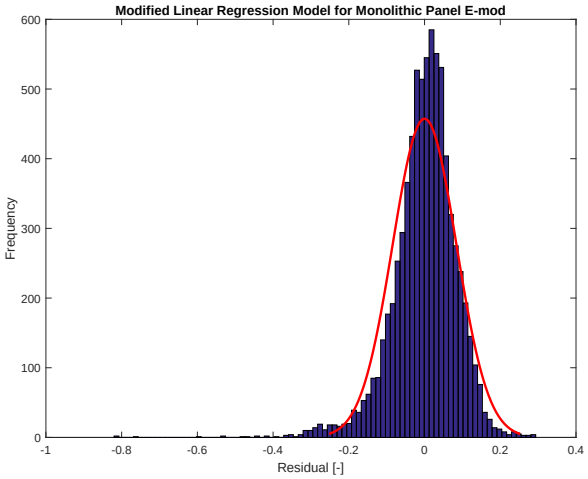

(b) Linear regression model

Figure 4.3: Models predicting E-modulus of monolithic panel

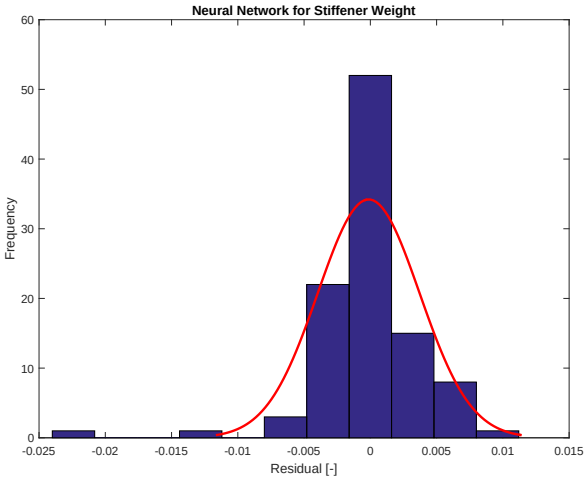

(a) Neural network

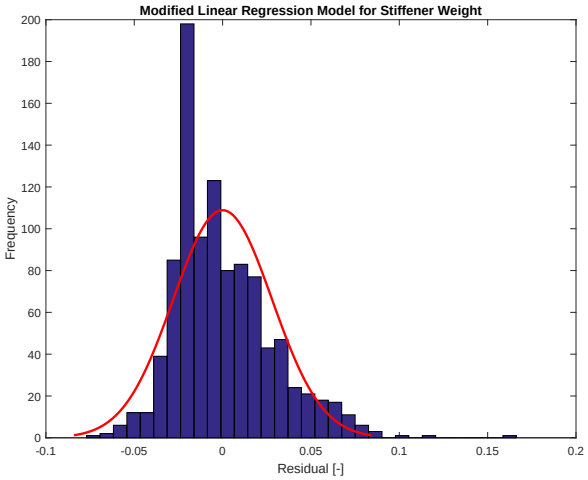

(b) Linear regression model

Figure 4.4: Models predicting weight of C-shape stringer

regression models still perform well from an absolute point of view, so the results presented may be used with good accuracy.

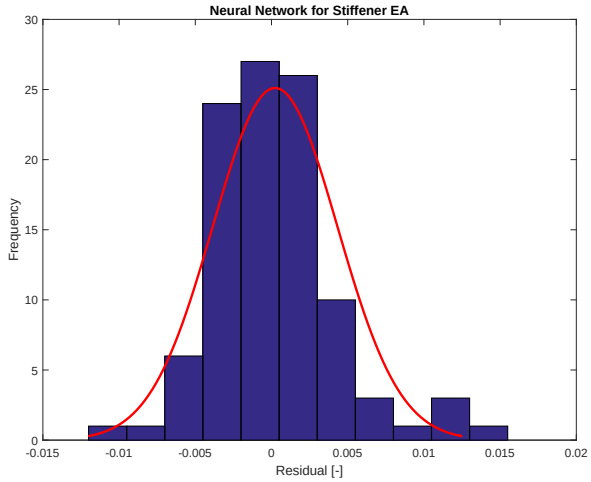

(a) Neural network

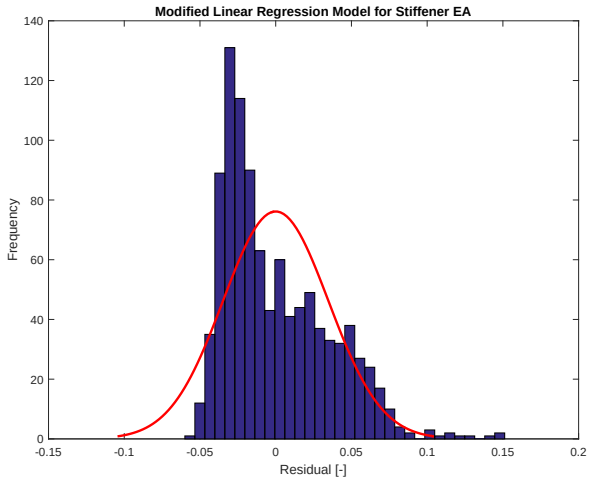

(b) Linear regression model

Figure 4.5: Models predicting axial stiffness of C-shape stringer

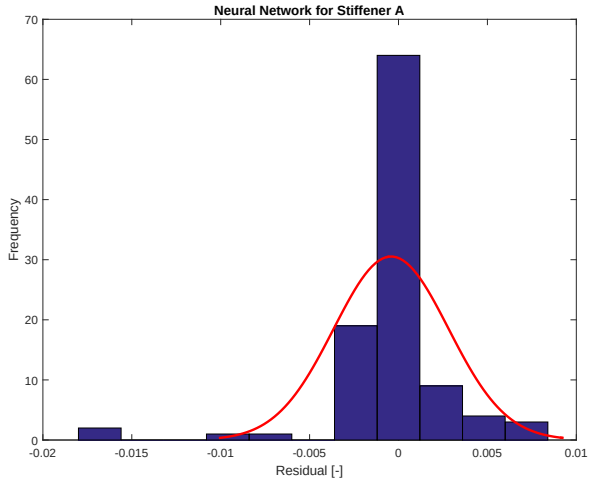

(a) Neural network

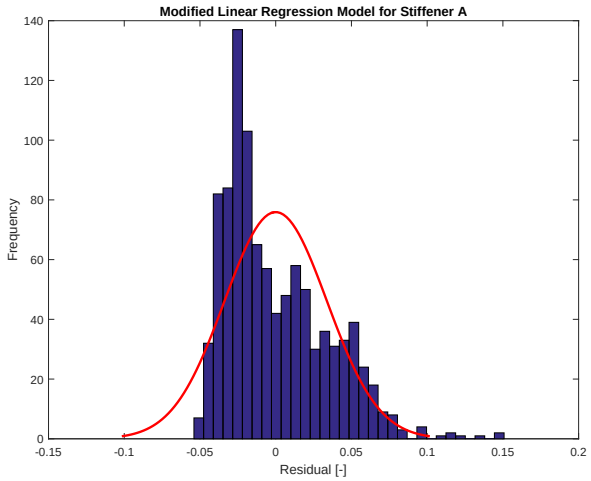

(b) Linear regression model

Figure 4.6: Models predicting cross-sectional area of C-shape stringer

4.2. Sandwich panels

Surrogate models for sandwich panels were made predicting weight, face thickness, core thickness and face Young modulus in the panel length direction. As with the previous models, the neural networks in Figure 4.7a, Figure 4.8a, Figure 4.9a and Figure 4.10a perform well, with a small residual and evenly distributed around zero.

The least-squares regression model in Figure 4.7b for the sandwich panel weight performs slightly worse than the neural network, with a larger spread, but still evenly around zero. The model predicting face thickness performs almost identical to its neural network counterpart, see Figure 4.8b. The core thickness, on the other hand, is best approximated by the neural network. Finally, Figure 4.10b shows an almost identical performance as Figure 4.10a for the facing Young's modulus.

The linear regression models obtained for sandwich panels are shown in Table 4.5. Several interesting observations can be made from the coefficients. It is again noted that although the predictors and responses are non-dimensional, the original ranges of the predictor variables have an influence on the magnitude of the corresponding coefficients. With that in mind, N_{xy} can be seen as the most sizing load. For the weight, its products with length and width form the largest coefficients. In the thickness model its first and second order terms are the most influential coefficients. For the core thickness and Young's modulus models these effects are observed again. Secondly, the area $L : W$ plays an important role

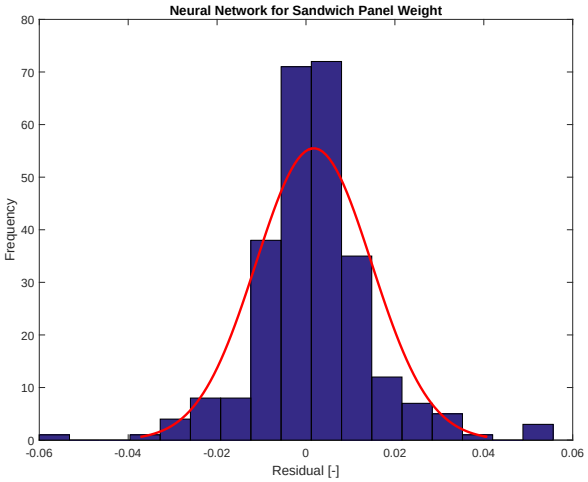

(a) Neural network

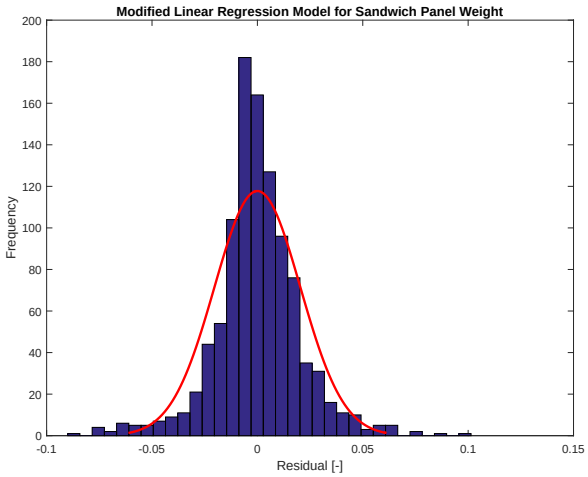

(b) Linear regression model

Figure 4.7: Models predicting weight of sandwich panel

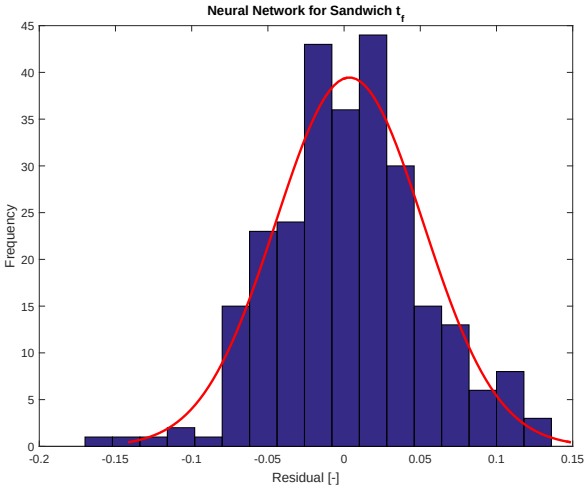

(a) Neural network

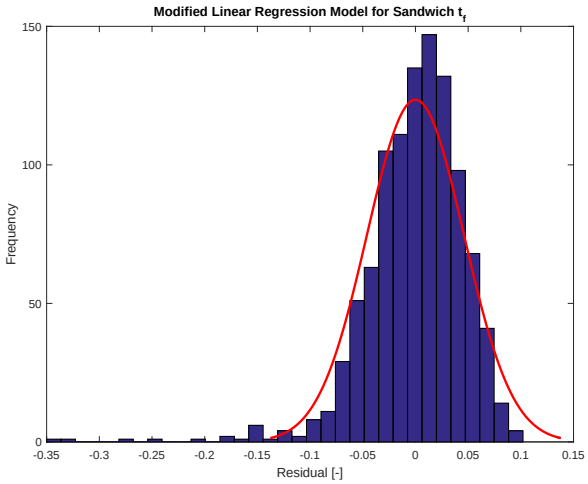

(b) Linear regression model

Figure 4.8: Models predicting t_f of sandwich panel

in the panel weight and core thickness. Thirdly, especially for core thickness, width seems more sizing than length. This is surprising when considering the actual values for length are much larger than the width (see Table 4.1). Apparently, changing the length of a long panel does not have a large effect on the weight and dimensions, but widening such a panel leads to early failure, driving the weight and thickness.

Table 4.5: Regression models for sandwich panel

Weight	
Predictor	Coefficient
(Intercept)	0.098285
L	-0.14894
W	-0.21669
N_x	-0.049661
N_{xy}	-0.15907
N_y	-0.026317
p	-0.021847
$L : W$	0.49268
$L : N_x$	0.065658
$L : N_{xy}$	0.30703
$L : N_y$	0.035387
$L : p$	0.043546
$W : N_x$	0.047226
$W : N_{xy}$	0.22087
$W : N_y$	0.035151
$W : p$	0.054924
$N_x : N_{xy}$	0.01512
$N_x : N_y$	-0.024174
$N_{xy} : N_y$	0.024123
$N_y : p$	-0.019371
W^2	0.059175
N_x^2	0.027342
N_{xy}^2	0.045483
N_y^2	0.016449
RMSE	0.0206
R-squared	0.98

Face Thickness	
Predictor	Coefficient
(Intercept)	-0.032381
W	-0.021734
N_x	0.015829
N_{xy}	0.45328
N_y	-0.017122
$W : N_{xy}$	0.036574
$N_x : N_y$	-0.12726
$N_{xy} : N_y$	0.078797
N_x^2	0.17519
N_{xy}^2	0.24541
N_y^2	0.1198
RMSE	0.0462
R-squared	0.962

Core Thickness	
Predictor	Coefficient
(Intercept)	-0.032037
L	0.19221
W	-0.30578
N_x	0.13566
N_{xy}	0.27082
N_y	0.073194
p	0.071702
$L : W$	0.18115
$L : N_x$	-0.052638
$L : N_{xy}$	-0.074424
$L : p$	0.087353
$W : N_{xy}$	-0.39912
$W : p$	0.54994
$N_x : N_{xy}$	-0.060692
$N_{xy} : p$	-0.22727
L^2	-0.2216
W^2	0.46685
N_x^2	-0.053974
N_{xy}^2	0.087076
N_y^2	-0.091354
p^2	-0.10567
RMSE	0.0622
R-squared	0.832

E-modulus	
Predictor	Coefficient
(Intercept)	0.70905
L	-0.037006
W	0.062763
N_x	0.021223
N_{xy}	-1.2989
N_y	-0.30791
$L : N_y$	0.070033
$N_x : N_y$	-0.062684
$N_{xy} : N_y$	0.4013
W^2	-0.058873
N_{xy}^2	0.74196
RMSE	0.0876
R-squared	0.713

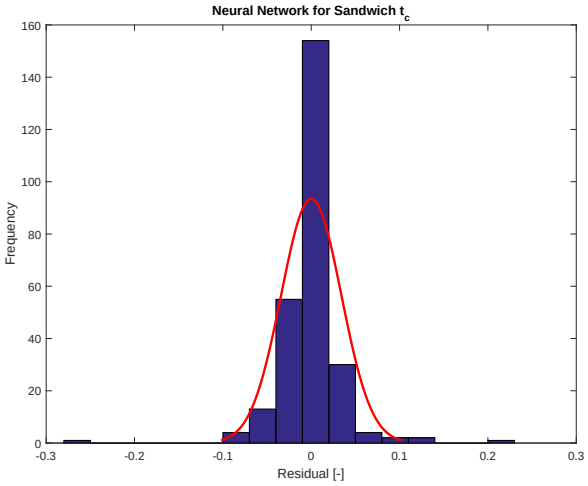

(a) Neural network

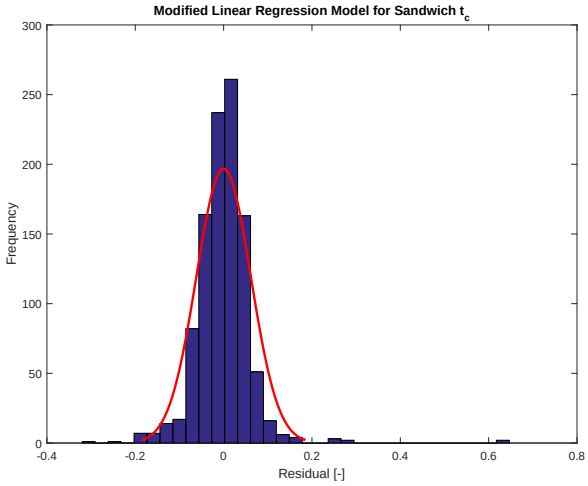

(b) Linear regression model

Figure 4.9: Models predicting t_c of sandwich panel

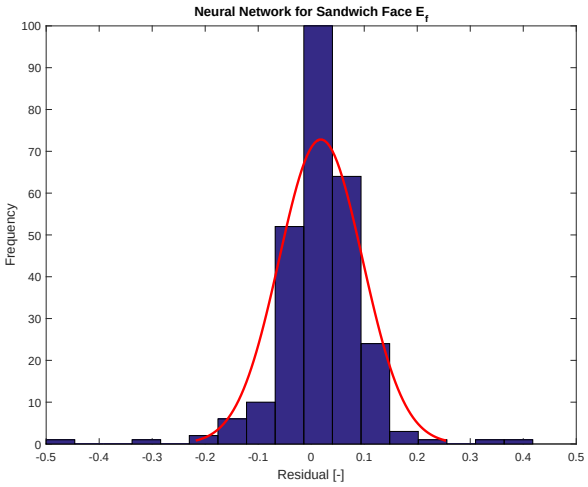

(a) Neural network

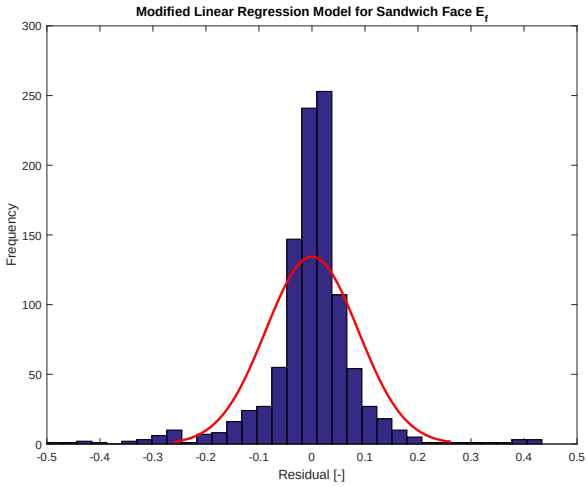

(b) Linear regression model

Figure 4.10: Models predicting E_f of sandwich panel

5

Pressure Loading

One of the reasons for the oval fuselage concept is the challenge of dealing with internal pressure in a non-cylindrical fuselage. For the 2D cross-section, the assumption that each arc carries the pressure load in membrane forces seems valid. The trapezoid structure can take on any difference in membrane forces between arcs and retain the section's shape. However, when considering a 3D geometry with the oval cross-section, it gets complicated, because the radii of the arcs can change in the longitudinal direction, which makes the shape in that direction non-circular nor straight. The aim of this chapter is to investigate the validity of the 2D assumption in the 3D case.

5.1. Shell of Arbitrary Shape

Flügge discusses in the book "Stresses in Shells" [25] how loads are distributed in shells. Not only shells of revolution are discussed, which generally have an analytical solution for the stresses due to internal pressure, but also a method is derived for determining the stresses in a shell of arbitrary shape.

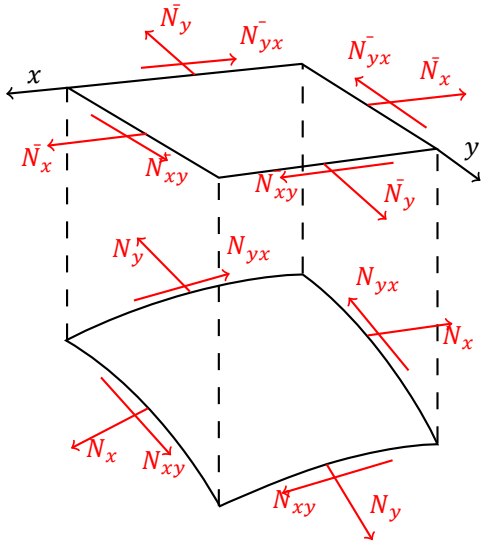

Figure 5.1: Arbitrary shell element

Consider an element of any shell, as depicted in Figure 5.1. The element is obtained by cutting the shell in the longitudinal and transverse directions. Hence, when projecting the element on the x-y plane, a rectangular element is obtained. On this transformed domain, a stress function Φ is defined which is described as follows:

$$\frac{\partial^2\Phi}{\partial x^2}\frac{\partial^2 z}{\partial y^2} - 2\frac{\partial^2\Phi}{\partial x\partial y}\frac{\partial^2 z}{\partial x\partial y} + \frac{\partial^2\Phi}{\partial y^2}\frac{\partial^2 z}{\partial x^2} = -\bar{p}_z + \bar{p}_x\frac{\partial z}{\partial x} + \bar{p}_y\frac{\partial z}{\partial y} + \frac{\partial^2 z}{\partial x^2}\int \bar{p}_x dx + \frac{\partial^2 z}{\partial y^2}\int \bar{p}_y dy \qquad (5.1)$$

Furthermore:

$$\bar{N}_x = \frac{\partial^2 \Phi}{\partial y^2} - \int \bar{p}_x \mathrm{d}x \tag{5.2}$$

$$\bar{N}_y = \frac{\partial^2 \Phi}{\partial x^2} - \int \bar{p}_y \mathrm{d}y \tag{5.3}$$

$$\bar{N}_{xy} = -\frac{\partial^2 \Phi}{\partial x \partial y} \tag{5.4}$$

Transforming the projected values (with a bar) to the real values in the shell, the following transformations are used:

$$N_x = \bar{N}_x \frac{\cos\theta}{\cos\chi} \tag{5.5}$$

$$N_y = \bar{N}_y \frac{\cos\chi}{\cos\theta} \tag{5.6}$$

$$N_{xy} = \bar{N}_{xy} \tag{5.7}$$

Finally, for the transformed applied loads the following holds:

$$\frac{\bar{p}_x}{p_x} = \frac{\bar{p}_y}{p_y} = \frac{\bar{p}_z}{p_z} = \frac{\mathrm{d}A}{\mathrm{d}x\mathrm{d}y} = \frac{\sqrt{1 - \sin^2\chi \sin^2\theta}}{\cos\chi\cos\theta} \tag{5.8}$$

5.2. Discretization

Obviously, Equation 5.1 is a partial differential equation (PDE) in two variables, and therefore obtaining an exact solution is complicated if not impossible. However, numerical techniques can be used to solve such an equation.

The PDE in Equation 5.1 is differentiable in two variables: x and y. Consider an $m \times n$ grid of coordinates as shown in Figure 5.2, formed by x-y pairs, and on each coordinate both a z position is defined (the geometry) and the N and p loads. Then the derivatives of all relevant parameters can be determined using finite differences and Equation 5.1 becomes:

$$\begin{aligned}
&\frac{1}{d^2}\left(\Phi_{m-1,n} - 2\Phi_{m,n} + \Phi_{m+1,n}\right)\left(\frac{\partial^2 z}{\partial y^2}\right)_{m,n} - \\
&\frac{1}{2de}\left(\Phi_{m+1,n+1} - \Phi_{m+1,n-1} - \Phi_{m-1,n+1} + \Phi_{m-1,n-1}\right)\left(\frac{\partial^2 z}{\partial x \partial y}\right)_{m,n} + \\
&\frac{1}{e^2}\left(\Phi_{m,n-1} - 2\Phi_{m,n} + \Phi_{m,n+1}\right)\left(\frac{\partial^2 z}{\partial x^2}\right)_{m,n} = \\
&-(\bar{p}_z)_{m,n} + (\bar{p}_x)_{m,n}\left(\frac{\partial z}{\partial x}\right)_{m,n} + (\bar{p}_y)_{m,n}\left(\frac{\partial z}{\partial y}\right)_{m,n} + \\
&\left(\frac{\partial^2 z}{\partial x^2}\right)_{m,n} \cdot (\bar{p}_x)_{m,n} \cdot d + \left(\frac{\partial^2 z}{\partial y^2}\right)_{m,n} \cdot (\bar{p}_y)_{m,n} \cdot e
\end{aligned} \tag{5.9}$$

Equation 5.9 was derived using central differencing. On the edges and corners of the grid, however, such a finite differencing scheme can not be used, because it would refer to non-existent grid points. Figure 5.2 also shows the boundary conditions used on the grid boundaries. The stress function is put to zero at all points outside the modeled fomain. Such a boundary condition is indicated by Flügge as being valid [25], since the stress function should be constant along the boundary when the shape is symmetric in at least one direction and may attain an arbitrary value.

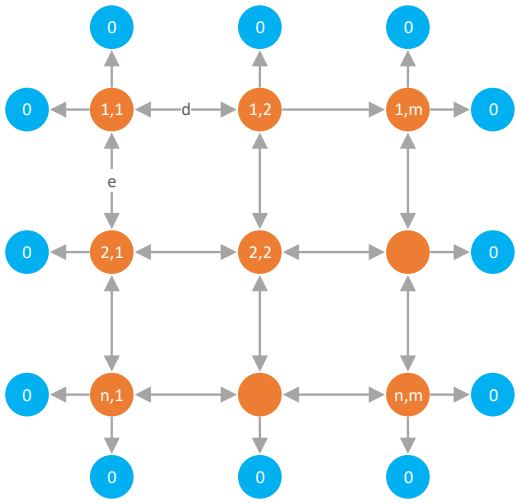

Figure 5.2: Grid for finite difference method

5.3. Solution

As was presented in the previous section, for each grid point the stress function can be expressed as a function of itself and neighboring points. By putting all function values at the grid points in a column vector, a $m \times n$,$m \times n$ matrix $\mathbf{A}$ can be constructed which contains the coefficients with which each stress value Φ is multiplied, i.e. each row in this matrix represents Equation 5.9 for one grid point. Since Equation 5.9 also contains constant terms, independent of any stress function value, these can be put in another column vector $\mathbf{C}$. Performing these operations allows Equation 5.9 to be written for all grid points as a system of linear equations:

$$\mathbf{A} \cdot \Phi = \mathbf{C} \tag{5.10}$$

This system is solved using Gaussian Elimination with pivoting.
In order to verify the implemented approach, a circular cylinder was analyzed, for which analytical solutions exist. The hoop stress in a circular cylinder is given by Equation 2.20 and the longitudinal stress by Equation 2.21. Multiplying these equations by the thickness results in a line load in N/m, which is the load that can be obtained for a membrane solution as presented above.
Modeling a cylinder with $r = 3$ m and $p = 45$ kPa, the hoop line load should be 135 kN/m, and the longitudinal line load 77.5 kN/m. As can be seen in Figure 5.3b, the hoop load indeed approaches the analytical value, but the longitudinal load (Figure 5.3a) is not constant and does not approach the analytical value. Performing the analysis with a longer cylinder (but same grid size) does not improve the situation: the longitudinal load increases, while retaining a nonlinear, symmetrical distribution along the cylinder.
With a coarse grid, the hoop load is close to the analytical value, but with a finer grid the value is better approximated. Similarly, the longitudinal load does not change greatly when refining the grid. On the contrary, computation time increases drastically with a finer grid.

5.4. Effect of Oval Shape in Three Dimensions

Even though the longitudinal load is incorrectly determined by the finite difference method when compared to the analytical result for a circular cylinder, it might be interesting to see the effects of curvature in the longitudinal direction as well. Figure 5.4a and Figure 5.4b show the longitudinal and hoop loads, respectively. At the pinched location much larger loads are observed than in the rest of the section, and larger than the circular cylinder in Figure 5.3a and Figure 5.3b. However, these results are of little significance because the longitudinal loads are possibly incorrect, but nonetheless point out that the effect of curvature in all directions may affect pressurization loads significantly. It is therefore an important subject for further study.

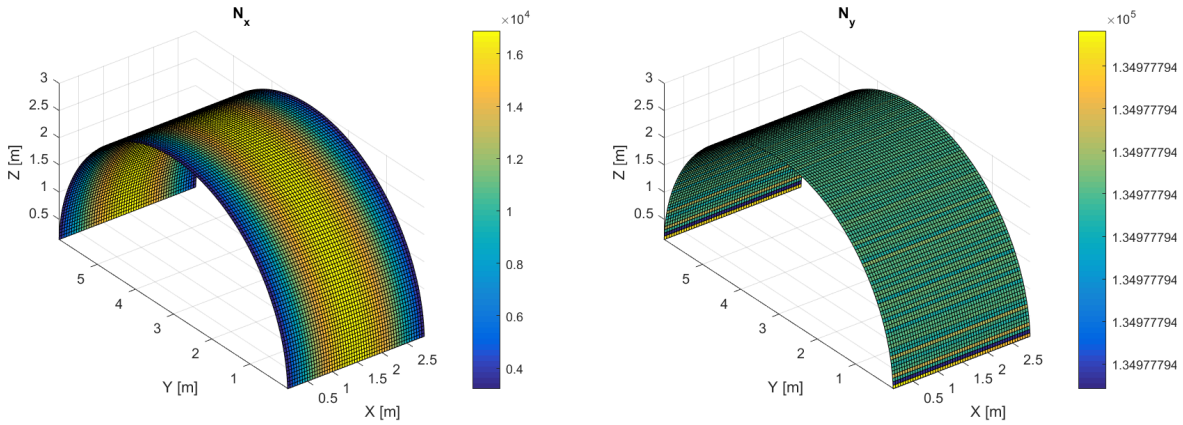

(a) Longitudinal load (b) Circumferential load

Figure 5.3: Pressure loads in circular cylinder

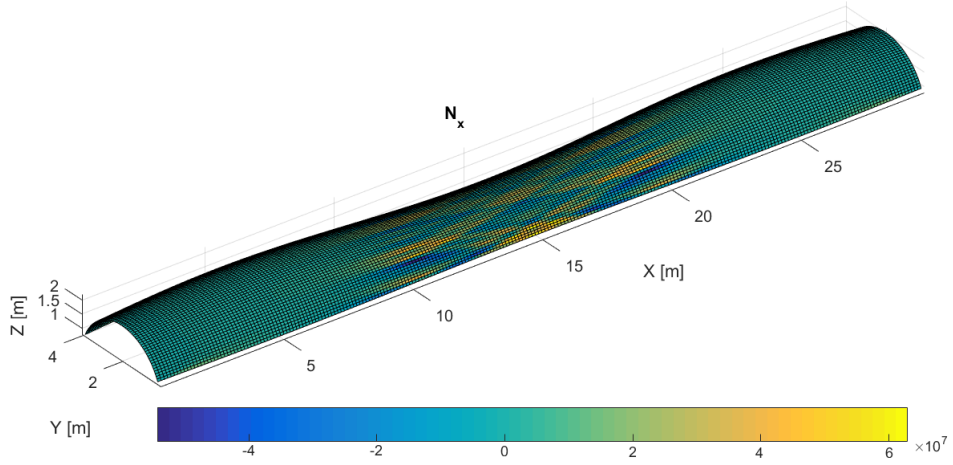

(a) Longitudinal load

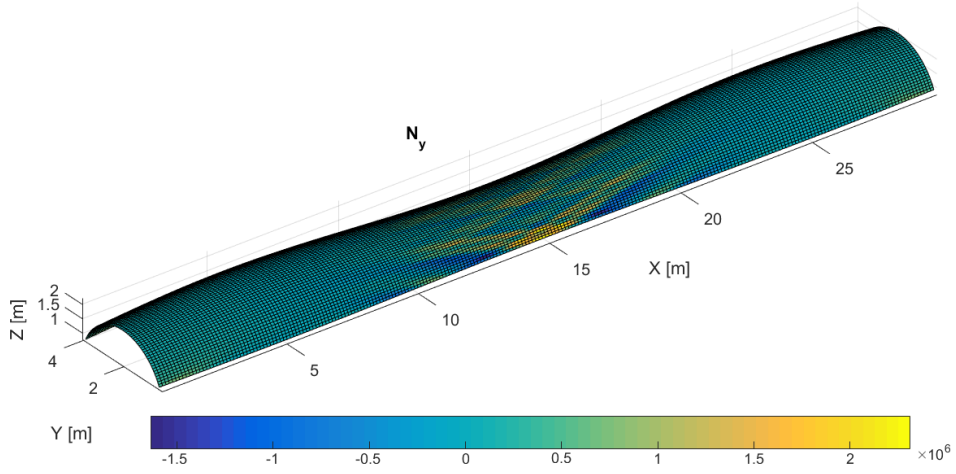

(b) Circumferential load

Figure 5.4: Pressure loads in tapered cylinder

6

Verification & Validation

Verification and validation of a fuselage weight estimation is not straightforward: many intermediate calculations are performed and all their outcomes should be checked, because it may occur that the final predicted weight is within an acceptable margin from the real weight, while the skin is sized too thin, the stringers too large and the empirical estimation for bulkheads compensates for the two, for example. However, detailed information of the actual fuselage structure dimensions are hard to obtain, which also holds true for the loads acting on the structure. As such, those aspects of the presented method that could be verified and/or validated are discussed in this chapter, but it is noted beforehand that this excludes some parts of the method.

In the order of procedures performed by the weight estimation method, first the shear and moment distribution calculations are verified for an Airbus A320-200. Consecutively, the boom method is verified. Sizing of the monolithic panels and stringers was verified in Ref. [22] to produce the same result as a computationally more expensive genetic optimization algorithm. However, since a pressure load was added for the present study, and sandwich panels were implemented, FEA analyses have been performed on these to validate the correct failure point. Finally, the weight estimation itself is verified.

6.1. Applied Loads Verification

For an Airbus A320-200, the shear forces and bending moments acting on the fuselage are shown in Figure 6.1a and Figure 6.1b from Van Tooren [13], respectively. Running the Initiator with an input file resembling the A320 gives a shear force and moment distribution similar to those presented by Van Tooren, as can be seen in Figure 6.2a and Figure 6.2b. Please note that these latter two distributions only include the portion of the fuselage acting as passenger cabin, and therefore the nose and tail sections are not shown. The shear force magnitude is similar for both plots, but the shape differs quite significantly. Conversely, the bending moment diagram shape is similar between both distributions (except the Initiator features a larger jump at the wing root), but the magnitude is several orders of magnitude off. It is unknown what the original source of Figure 6.1a and Figure 6.1b is, and therefore care should be taken to draw conclusions from these results. Nonetheless, the load cases implemented in the Initiator may need revision.

6.2. Pressure Load Validation

FEA of an oval section with internal pressurization was performed using Abaqus. In order to model the pressure loads, symmetry boundary conditions were applied to the front and rear edges of the section, as well as the edges in the symmetry plane. A pressure of 45 kPa was applied and the Poisson's ratio of the material was set to 0.5, modeling a perfectly incompressible material. This way no load alleviation takes place due to contraction of the section in the longitudinal direction.

The pressure loads in longitudinal and hoop direction are shown in Figure 6.3a and Figure 6.3b, respectively. The exact values from the analytical method and an approximate average of the FEA results are shown in Table 6.1. It can be seen that both the hoop and longitudinal stresses are approximated accurately. On a critical note, though, the presented section is straight, i.e. the cross-section does not

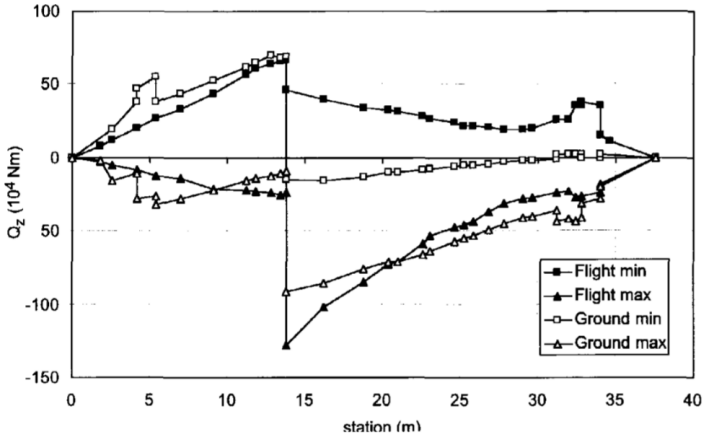

(a) Shear force envelope in A320-200 [13]

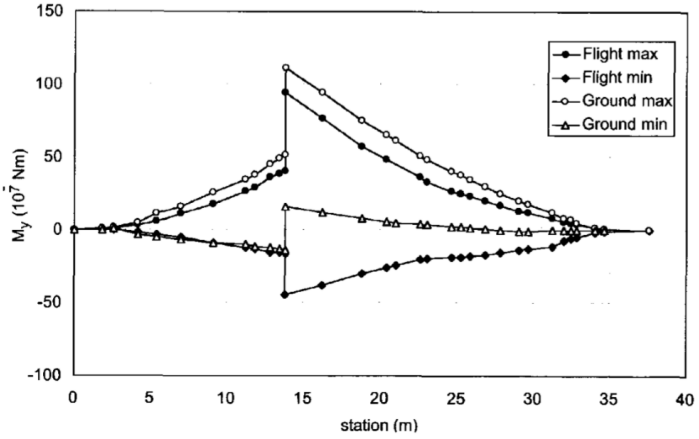

(b) Bending moment envelope in A320-200 [13]

Figure 6.1: A320 internal loads from literature

change in longitudinal direction. Therefore the analytical solution for pressurization stress holds. Further research has to point out whether such good agreement is maintained when the fuselage shape is more complex (i.e. changes in longitudinal direction).

Table 6.1: Comparison of FEA and analytical hoop pressure stress

Member	FEA [MPa]	Analytical [MPa]	Error
Arc 1	35.4	35.3	-0.28%
Arc 2	10.5	10.5	0%
Arc 3	26.8	26.7	-0.37%
Ceiling	-10.9	-11.0	-0.92%
Wall	8.00	8.05	0.63%
Floor	-7.2	-7.17	0.42%

6.3. Boom Method Verification and Validation

The implementation of the boom method is verified by examining the direct stress resulting from the applied bending moment and the shear flow resulting from the applied shear forces. Because a symmetrical cross-section was assumed and all loads are applied in the axis of symmetry, it is expected that both the stress and shearflow distributions along the cross-section are symmetrical (for stress exactly equal, for shear flow equal magnitude, opposite sign). Moreover, the shear flow becomes zero at exactly the top and bottom of the cross-section and has a maximum in between. The direct stress is

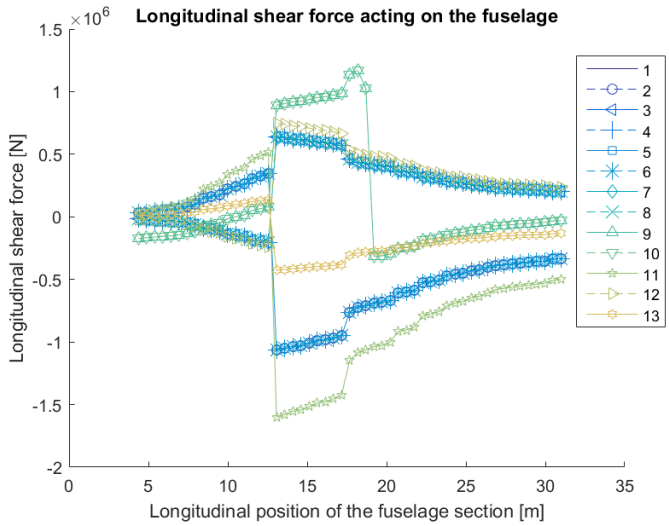

(a) Shear force envelope in A320-200 from Initiator

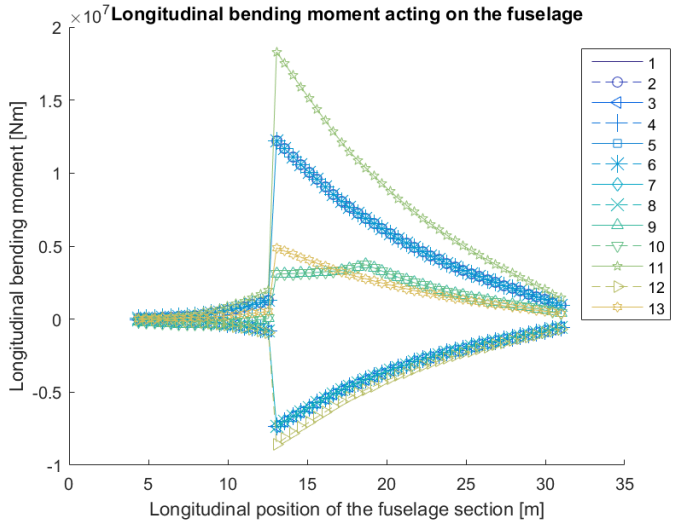

(b) Bending moment envelope in A320-200 from Initiator

Figure 6.2: A320 internal loads from Initiator

maximum at the top or bottom of the fuselage.

To test above statements, an arbitrary oval cross-section was created and a fuselage section of approximately 5 m was created. A constant shear force of 998,800 N and constant bending moment of 9,537,600 Nm were applied, where the bending moment is oriented such that the upper side of the fuselage is in compression (which is not necessarily an actual load case). The resulting boom stresses and shear stress computed by the boom method are shown in Figure 6.4a and Figure 6.5a, respectively.

As can be seen from Figure 6.4a, the stress is indeed negative in the upper portion of the fuselage section and its positive maximum is exactly at the bottom. However, the minimum is located at the junction of the top and side arc (and ceiling and wall). The stress shown in this figure was scaled to the smeared stringer thickness (for comparison with FEA, presented hereafter), which is not equal to the boom stress. Because the boom areas include the skin and those in the side arc also the wall, the boom stress is different from the actual stress in the (smeared) stringers. This also explains the jump in direct stress observed in Figure 6.4a and why the minimum stress is not observed in the top of the section.

Figure 6.4b and Figure 6.5b show the same fuselage section as discussed earlier, but now modeled using Abaqus. No stringers were modeled; instead the smeared stringer thickness was used to model

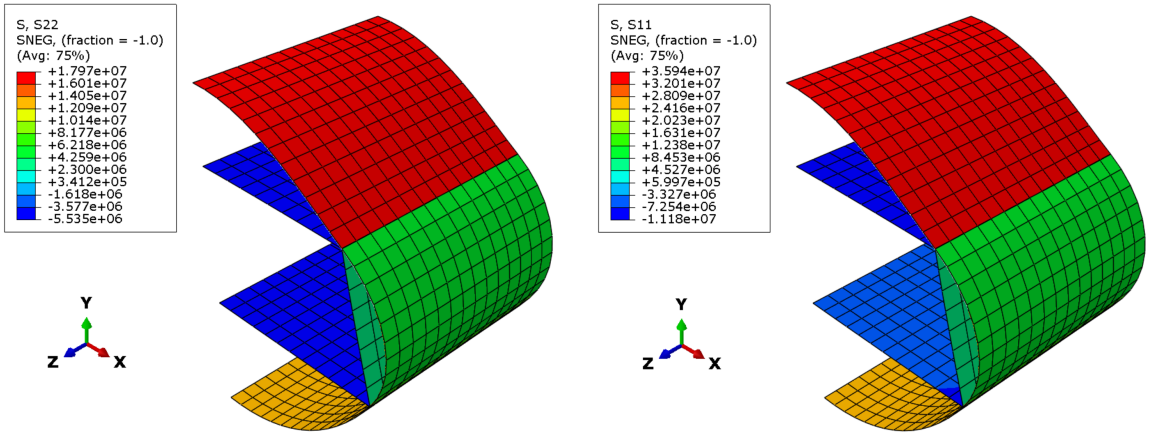

(a) Longitudinal stress in oval section

(b) Hoop stress in oval section

Figure 6.3: Pressurization loads from Abaqus

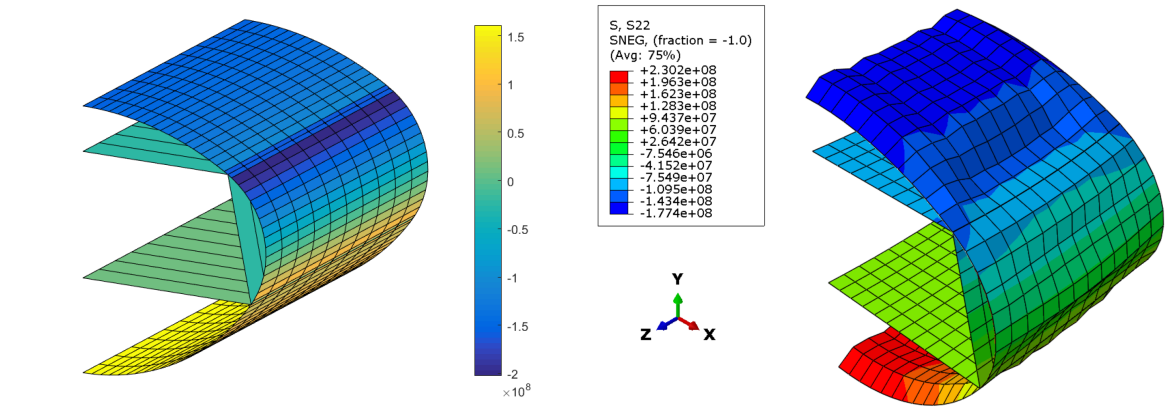

(a) Initiator

(b) Abaqus

Figure 6.4: Direct stress comparison

the stringers as a skin. Even with this approximation and the difference that in the FEA model a trapezoid structure is present, which is omitted in the boom method, good agreement is reached between the boom method and FEA. As expected, the signs of both direct and shear stress are identical for both methods. More interestingly, the magnitude of both stresses is also similar for both methods, giving confidence in the implemented boom method.

6.4. Panel Failure Validation

Of major importance are the sizing procedures implemented for stringers, panels and sandwich panels. Two aspects of the procedure needed to be verified and validated: firstly, the analytical failure criteria should be compared with FEA and secondly, the deterministic optimization should be verified using a more robust (but more computationally expensive) optimizer.

The shear buckling analysis implemented was checked with FEA results. Three different plate dimensions, representing three different aspect ratios, were used and for each multiple shear loads were applied. First the analytical method was run to optimize a certain laminate for that specific panel and load combination. Secondly, that panel with the optimized laminate was modeled in Abaqus and a buckling analysis was performed to see whether the failure modes match. The boundary conditions in Abaqus resemble a simply supported plate, which was also assumed in the analytical methods.

In Figure 6.6b and Figure 6.6c it can be seen that fairly good agreement is achieved between the analytical method and FEA. The error ranges from 5% to 20% and from 13% to 66%, respectively.

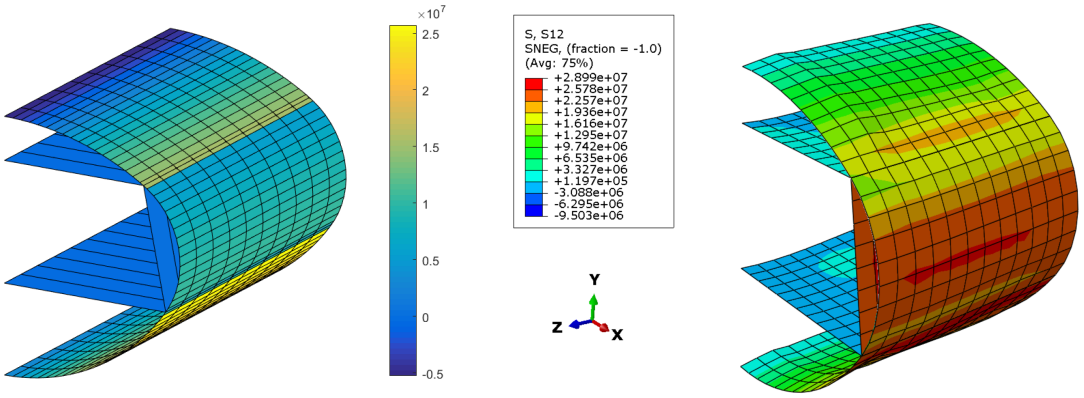

(a) Initiator

(b) Abaqus

Figure 6.5: Shear stress comparison

Table 6.2: Comparison of Tsai-Wu failure criterion

a [m]	b [m]	N_x [kN/m]	N_y [kN/m]	Layup	Analytical Tsai-Wu [-]	FEA Tsai-Wu [-]	Difference [%]
0.5	0.3	250	500	$[\pm 45/90_5/0/90_2/\pm 45/\bar{0}]_s$	0.37	0.44	-17
0.5	0.5	500	500	$[\pm 45/90_5/0/90_5/\pm 45/90_3/0/90/\pm 45/\bar{0}]_s$	0.50	0.56	-10
0.5	0.3	100	100	$[\pm 45/90/0]_s$	0.29	0.36	-20
0.3	0.3	200	200	$[\pm 45/90/0]_s$	0.66	0.72	-8.8
0.3	0.3	200	0	$[0]_s$	0.55	0.76	-29
0.3	0.3	0	200	$[90]_s$	0.55	0.76	-29
0.3	0.3	200	200	$[(\pm 45)_2]_s$	0.66	0.72	-8.8

The square panel shear buckling failure as obtained from Figure 6.6a shows a large error which is approximately constant around 55 %. Note that the analytical results in Figure 6.6a and Figure 6.6b were obtained using an empirical relation, while Figure 6.6c was computed using a semi-analytical relation, as was explained in subsection 3.2.1.

The difference in Figure 6.6a is large, but a conservative result is obtained since a lower critical load is predicted by the analytical approach. Additionally, panels of this aspect ratio are rarely found in fuselage structures. However, the results from Figure 6.6c are applicable to panels in fuselage structures and these results are non-conservative. In order to account for this, the estimated critical shear buckling load may be scaled to more closely represent the FEA data. A scaling factor obtained from Figure 6.6c is provided by:

$$R_{N_{xy}} = 0.88846 \cdot N_{xy}^{-0.16974} \tag{6.1}$$

This factor should be multiplied by the analytical result to obtain the FEA result. Note that the unit for N_{xy} is kN/m. Obviously, to obtain a more reliable scaling factor additional cases have to be run.

Additionally, the maximum deflection of panels under transverse pressure was compared with FEA. A pressure of 60 kPa was applied, with panels of length 0.8 m and varying widths. The results are shown in Figure 6.7, where good agreement is observed between the analytical routine and FEA. The maximum error is around 4%.

A final test is required to conclude this validation, namely checking whether the Tsai-Wu failure criterion as computed by the deterministic approach matches the one computed from FEA. By doing this, computation of the internal stresses is compared, albeit not directly.

Several panel size and load cases were run and the results are shown in Table 6.2. Each panel from the ALGO program was modeled using Abaqus. The first three cases were optimized by ALGO based on dimensions and applied loads, while all other laminates were pre-defined as additional test cases. The Tsai-Wu failure values were checked at each ply and the highest values present in the laminate are shown here. On a final note, $\bar{0}$ means it is a midply, i.e. is not repeated in the symmetry pattern.

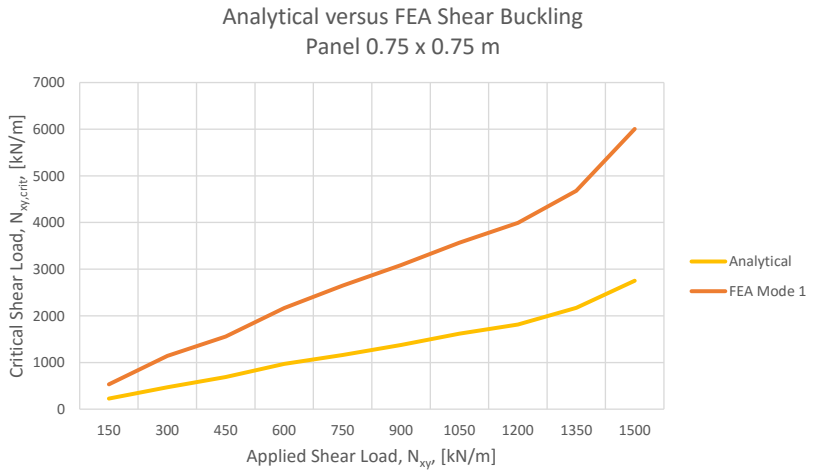

(a) Panel shear buckling failure for $a/b = 1$

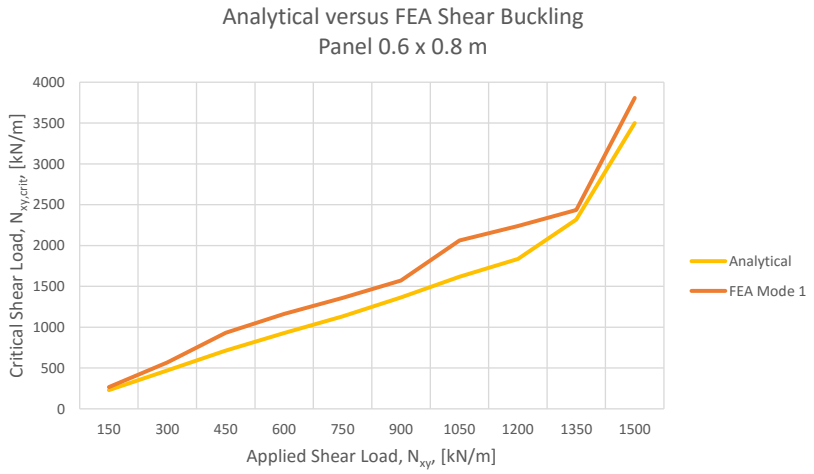

(b) Panel shear buckling failure for $a/b = 0.75$

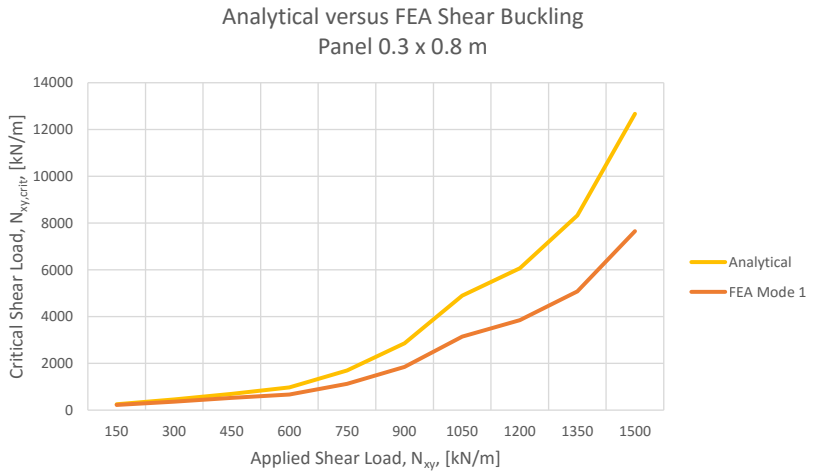

(c) Panel shear buckling failure for $a/b = 0.375$

Figure 6.6: Validation results for panel shear buckling

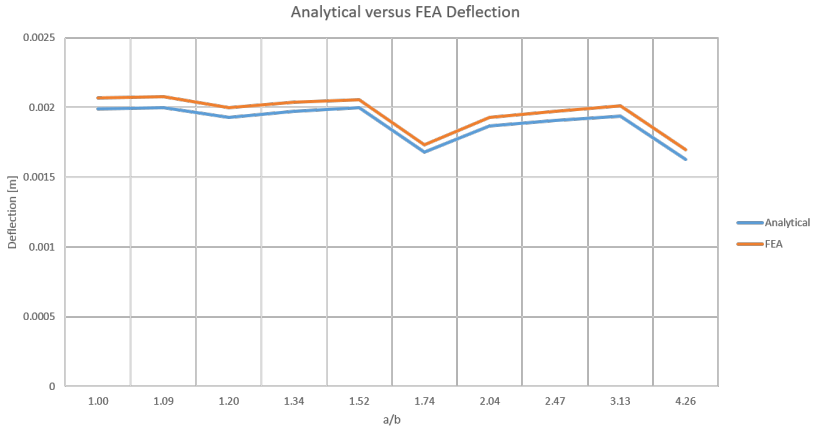

Figure 6.7: Panel pressure deflection

From Table 6.2 it is clear that the analytical calculation under-predicts material failure. This means that a non-conservative design is obtained. However, to put this error into perspective, take the third panel from Table 6.2. When a 0 ply is added (in symmetry, so 2 plies in total), the FEA shows a Tsai-Wu failure value of 0.3054, which is slightly above the value obtained with the deterministic approach for the original panel. Considering an A320 fuselage, with 335 m^2 skin area, this results in a mass penalty of 164 kg, or 1.84 % of the total fuselage mass.

6.5. Verification of Optimization using GA

In order to verify that the deterministic optimization routine arrives at the lightest panel possible for the required dimensions and applied loads, 150 random combinations of dimensions and loads were generated and both the analytical procedure and a genetic algorithm were run to find the most suitable laminate.

The genetic algorithm was set up with a design vector where the first entry denotes the ply angle of the midply, or the absence of a midply. The next n entries denote an amount of plies, where n_i can range from 0 to 5 (the maximum amount of identical, consecutive plies). The last n entries denote the ply angles. As a final note, the stacking sequence defined this way is made symmetrical around the midply. To illustrate, suppose $n = 30$ and there is a midply. Then the maximum number of plies in the laminate is 301 $(= 2 \times (30 \times 5) + 1)$. The same failure analysis is used for both GA and deterministic optimization and also a laminate validity check is performed in the GA constraint function, ensuring, among other things, the 10% rule and maximum ply stack.

For the skin panels, the weight difference between GA and ALGO is shown in Figure 6.8. The exact same histogram is obtained for the panel thickness, obviously. The difference was computed by dividing the GA weight by the ALGO result, such that a positive difference indicates that ALGO outperforms the GA and a negative difference indicates that the GA outperforms ALGO.

Most designs (90%) optimized by the GA are significantly lighter than the ALGO routine. A possible explanation is that the deterministic approach might jump from one critical failure mode to the next, adding plies in different directions every time. This might lead to a less efficient laminate than the one where all ply angles are optimized simultaneously. It should be noted, however, that the deterministic approach takes slightly more than a minute to complete 100 designs, while the GA requires approximately 10 hours.

For the stringers, just like with the deterministic approach, a family of laminates is generated beforehand and then a combination of laminates is taken and the flange widths are optimized. Therefore, the GA design vector now only contains six variables: three index variables pointing to a laminate in the family for each member and the three member widths. The results are shown in Figure 6.9, where an excellent similarity is seen between GA and ELFO. All designs have a positive difference between GA and ELFO, meaning that the GA always finds a heavier design than ELFO. This is likely a result of the fact that ELFO adopts a brute force approach (it analyzes all possible designs and chooses the lightest option).

Finally, the sandwich panel optimization was also compared to its GA counterpart. The results are

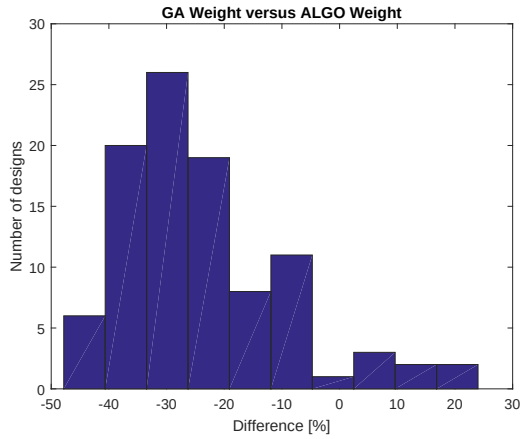

Figure 6.8: Genetic algorithm versus deterministic approach for skin panels

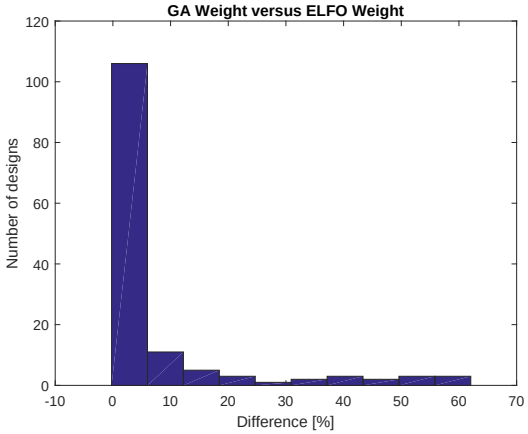

Figure 6.9: GA versus ELFO weight

shown in Figure 6.10a for the weight, Figure 6.10b for the facing thickness and Figure 6.10c for the core thickness. It becomes immediately clear that the difference is much larger between the deterministic approach and the genetic algorithm than for the monolithic panels and stringers. The exact cause for this is unclear, but the large difference happens on the positive side of the scale, meaning that there the genetic algorithm performs worse than the deterministic approach. Then, the error may arise from the amount of plies used in the design vector for the GA. With too few design variables it may be impossible to find a suitable laminate, while too many design variables make the GA optimize mainly the face laminate, while the core thickness is found to have less effect. One can see this in Figure 6.10c, where the GA has a thinner core for nearly all designs. This may partially explain the lighter designs from the deterministic approach.

6.6. Mass Estimation Verification

Combining all elements from the method presented so far, the weight estimation method should be verified as a whole. Two major problems arise though: no data is available on the weight of composite fuselages (the Airbus A350 and Boeing 787 are the only passenger aircraft currently with such a fuselage). Secondly, the oval fuselage is still a concept and has never been used in a real-life application. Therefore, verification is performed on several conventional aircraft, with metallic fuselages.

A generic weight breakdown for metallic, conventional fuselages is given in Figure 6.11 [26], which is used as a reference for the breakdowns provided by the implemented method. It should also be noted that the aircraft presented here are not the actual aircraft, but approximations, because the Initiator designs these aircraft based on a collection of settings and top-level requirements. Therefore, the

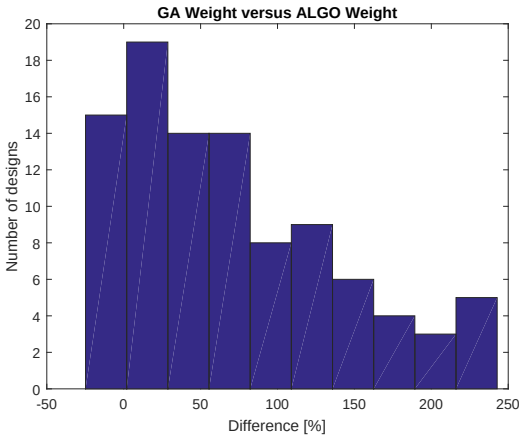

(a) GA versus ALGO weight

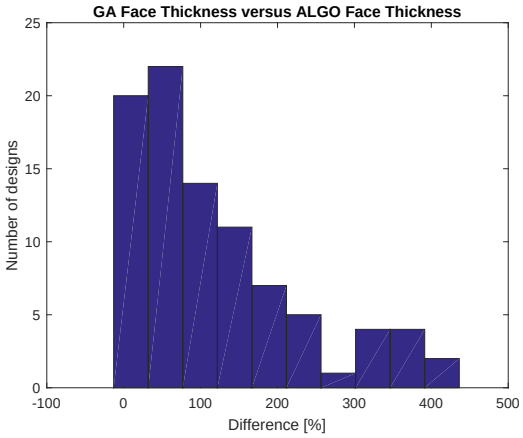

(b) GA versus ALGO face thickness

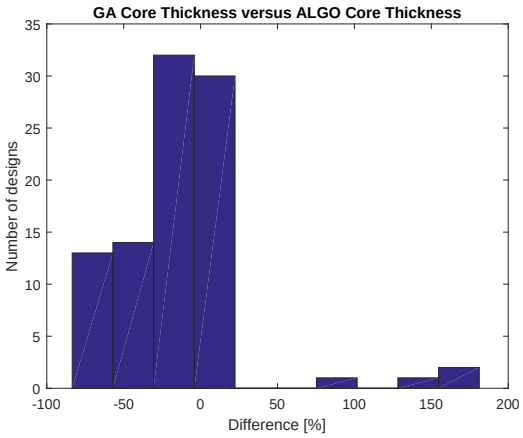

(c) GA versus ALGO core thickness

Figure 6.10: Genetic algorithm versus deterministic approach for sandwich panels

masses computed are not compared to the actual aircraft, but rather the fuselage mass fraction and difference with Torenbeek's empirical method are compared with.

Table 6.3 shows the fuselage mass as predicted by the Initiator compared to the empirical relation from Torenbeek [27]. Additionally, the MTOM from the Initiator and literature are provided. Finally, the fuselage fraction of total mass is given for both the Initiator and reality. Although several aircraft shown in Table 6.3 have a large error between the Initiator mass prediction and the empirical mass,

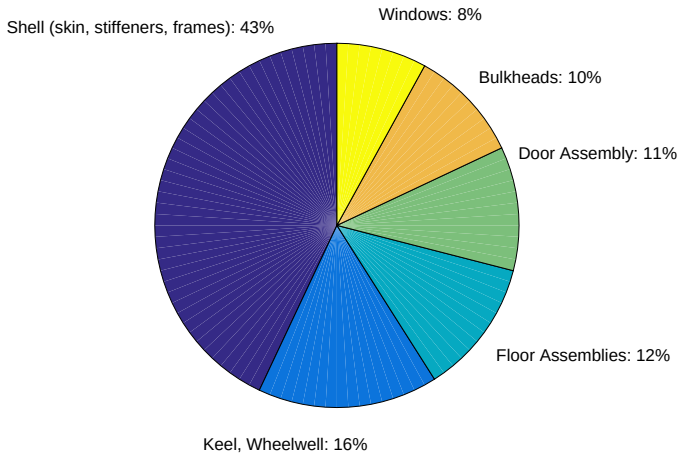

Figure 6.11: Generic weight breakdown for large passenger aircraft

Table 6.3: Estimated Fuselage Mass Comparison

Aircraft	$M_{\text{fus,Ini}}$ [kg]	$M_{\text{fus,Tor}}$ [kg]	$\frac{M_{\text{fus,Ini}}}{M_{\text{fus,Tor}}} - 1$ [%]	$M_{\text{TO,Ini}}$ [kg]	$M_{\text{TO,Act}}$ [kg]	$\frac{M_{\text{TO,Ini}}}{M_{\text{TO,Act}}} - 1$ [%]	$\frac{M_{\text{fus,Ini}}}{M_{\text{TO,Ini}}}$ [%]	$\frac{M_{\text{fus,Tor}}}{M_{\text{TO,Act}}}$ [%]
Airbus A320-200	9,655	8,798	9.74	86,435	73,500	17.60	11.17	11.97
Boeing 727-200	8,936	10,994	-18.72	62,133	83,800	-25.86	14.38	13.12
Boeing 767-300ER	28,273	19,791	42.86	261,270	186,880	39.81	10.82	10.59
Boeing 747-100	49,873	39,015	27.83	360,300	333,400	8.07	13.84	11.70
Airbus A340-300	34,989	28,570	22.47	279,520	276,500	1.09	12.52	10.33

the fuselage fraction is very similar for all aircraft considered. This means that the error may arise from other predictions performed by the Initiator (e.g. dimensions and MTOM), but that the fuselage mass estimation provides an acceptable result despite of this. The structural weight breakdowns of the Airbus A320-200 and Boeing 767-300ER are shown in Figure 6.12a and Figure 6.12b, respectively. Comparing to the generic breakdown in Figure 6.11, several observations are made. The stringer and frame mass seem to be sensitive to fuselage size. The Boeing 767-300ER has a longer fuselage with larger radius than an A320-200. The loads around the wing root increase significantly and therefore, as can be seen in Figure 6.13b, the stringer pitch reduces drastically in this area. The outlier frames were removed from the mass estimation, because the jump in shear flow in these sections results in unrealistically sized frames. However, still a large fraction of the fuselage mass consists of frames. Compared to Figure 6.11, the shell mass (skin, stringers and frames) is over-estimated by the current method (note that the nose and aft shell masses should be added as well). Another observation is that the (pressure) bulkhead mass is underestimated quite significantly, if the bulkhead mass in Figure 6.11 indeed only consists of pressure bulkheads. If also frames where the landing gear and/or wing are attached count as bulkheads, part of this mass is accounted for in the frames mass from the Initiator. The floor mass appears to be overestimated in the present method, but note that the cargo floor is included here. When the cargo floor is accounted for in the keel portion in Figure 6.11, this may again cancel each other out.

6.7. Sizing Verification

Returning to Figure 6.13a and Figure 6.13b, it may be concluded that sizing of the metal structure was done as expected. In the area where the wing is mounted and largest compression is found in the lower portion of the fuselage, the stringer pitch is small and many stringers are present. Additionally, the skin panels are thicker there and the thickest frames are observed there as well. At the same position, but in the upper portion of the fuselage, a larger stringer smeared thickness is found, which is necessary

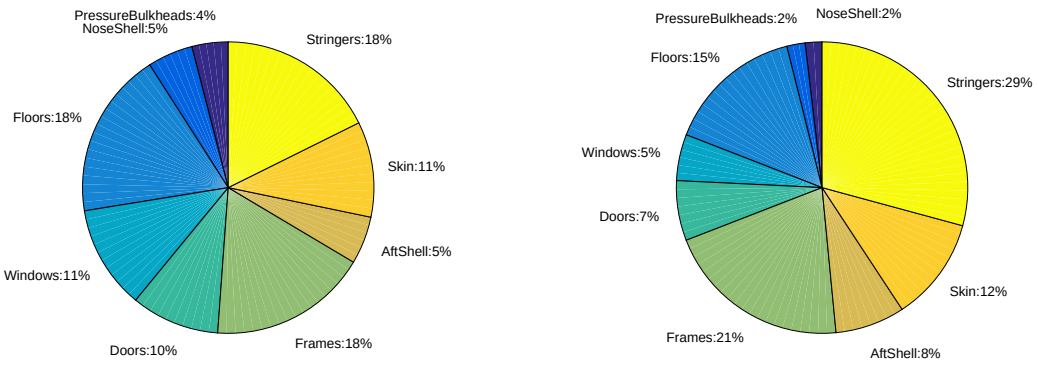

(a) Airbus A320-200 (b) Boeing 767-300ER

Figure 6.12: Weight breakdowns from Initiator for aluminium fuselage

to cope with the high tensile loads. Finally, the smallest stringers are observed in the side arc, where direct stresses are smallest (closest to the neutral axis).
The location around the wing root is heavily reinforced with thick skins and stringers. Normally, a cutout in the fuselage is present there, allowing for the wing box to carry through. It is a matter of bookkeeping whether this carry-through structure is part of the fuselage structure mass or wing structure mass. Additionally, the skins and stringers sized in this area may be seen as a replacement for a keel beam. However, further study would have to point out if this yields an acceptable prediction.

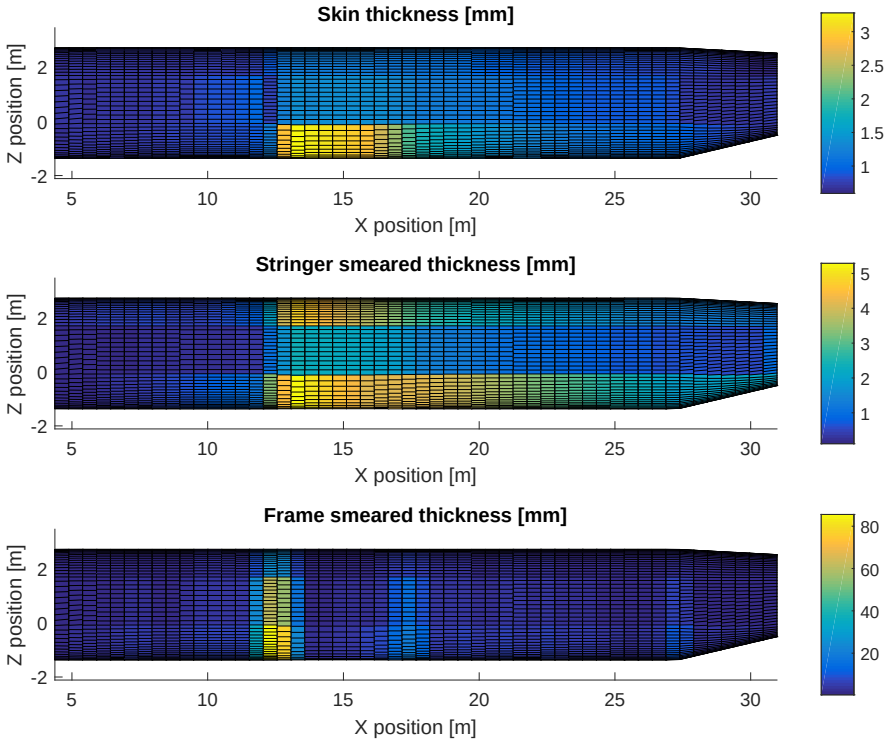

(a) Airbus A320-200

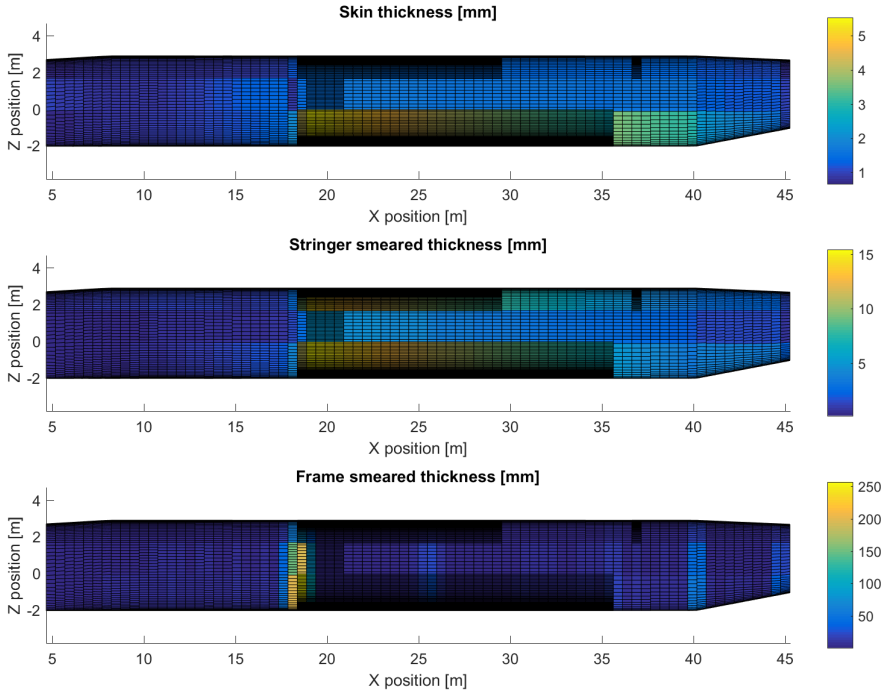

(b) Boeing 767-300ER

Figure 6.13: Thickness distributions for metal fuselages from Initiator

7

Results

This chapter focuses on showing some case studies of composite and oval fuselages, which do not exist in reality. The purpose is to get an idea of how the weight estimation method performs in these cases and if reasonable results are obtained. Moreover, it proves whether the method actually works for its intended goal.
The figures showing thickness distributions, shear flow and direct stress only cover the part of a fuselage where the passenger cabin is present. The rest of the fuselage is not modeled with the analytical methods and the mass of the front and aft shell are computed based on their wetted area and the average smeared thickness of skins, stringers and frames combined in the side arc.

7.1. Composite A320-200 and Boeing 767-300ER

Using the exact same input files as for a standard A320-200 and B767-300ER, but with aluminium replaced by the carbon fiber composite with the properties from Table 4.2, a lighter fuselage is expected. Moreover, with composites, one expects to find thicker skins and stringers.
Looking at the thicknesses in Figure 7.1 and Figure 7.2, the expectation of thicker skins and other structural components is met. The frame thickness follows the same trend as for metal fuselages, which may be expected considering the method used; only the bending moment and shear flow size the frames. The skin thickness distribution looks similar for both aircraft and also to the aluminium skin thickness distribution.
The stringer pitch distribution is also similar for both aircraft and similar to the metal distribution: in the bottom arc around the wing root the smallest stringer pitch is observed, along with the largest stringer smeared thickness. Again this is as expected, since the largest compression forces occur there. Along the side arc, least and smallest stringers are present and some thicker stringers are present in the top arc to cope with the high tensile loads there.
The weight breakdown for the composite A320 fuselage in Figure 7.3a shows the same trend as was observed in the NASA ACT papers (see section 2.8): the largest portion of the primary structure is taken up by skins and stringers and the frames form the other main portion of weight. Figure 7.3b shows approximately the same breakdown. Apparently, the stringer weight scales exponentially with the compression load (as was also observed from the linear regression coefficients) since the stringer mass becomes the main portion of fuselage mass. The large Boeing 767 fuselage has to cope with high bending loads, due to the large lift and mass of the aircraft. A remark is in order here, for actual fuselages have a cutout in this region to allow the wingbox to run through. Then it is a matter of bookkeeping whether the wingbox carry-through structure is part of the fuselage or wing mass and in case of the former option, whether the stringers, skins and frames sized in this region may account for the carry-through structure. The NASA results showed that skins form most of the primary structure, so it is likely that assuming skins take no direct stresses results in this underestimation. However, the stringer weight makes up for this, such that the weight estimation itself is not thwarted too much by this.
An interesting observation is the large cargo floor mass in Figure 7.3a and Figure 7.3b. This mass was obtained as a fraction of the bottom arc primary structure mass (skins, stringers and frames). It is likely that the bottom arc is estimated larger in the Initiator's geometry sizing than the keel panels are

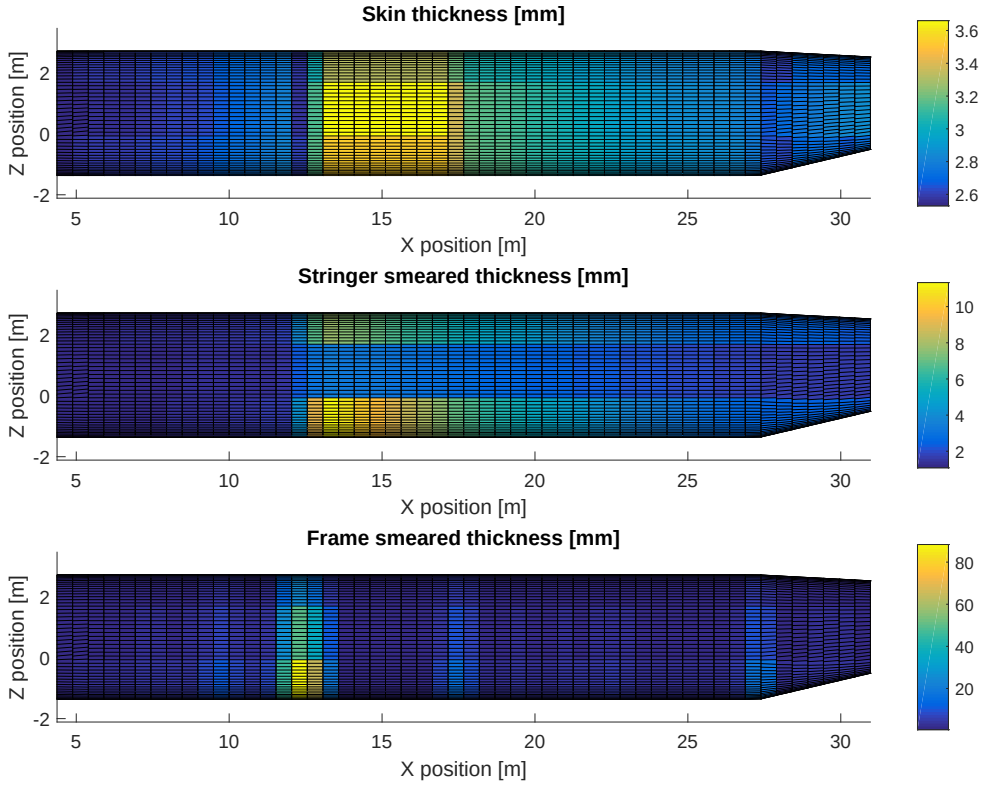

Figure 7.1: Composite Airbus A320-200 thickness distribution

Table 7.1: Estimated Composite Fuselage Mass

Aircraft	Mass [kg]	Weight Saving [%]
Airbus A320-200	7,790	19
Boeing 767-300ER	25,334	10
Boeing 727-200	7,584	15

in actual aircraft. Logically, the cargo floor mass is then sized inappropriately as well.
Finally, the composite fuselage mass is 7,790 kg and 25,334 kg for the A320 and Boeing 767, respectively, as can be seen in Table 7.1. The Boeing 727-200 fuselage is also included here for a better comparison of the weight saving obtained with composite material. Comparing the composite fuselage masses with the aluminium masses in Table 6.3, a weight saving of (on average) around 15 % is observed.

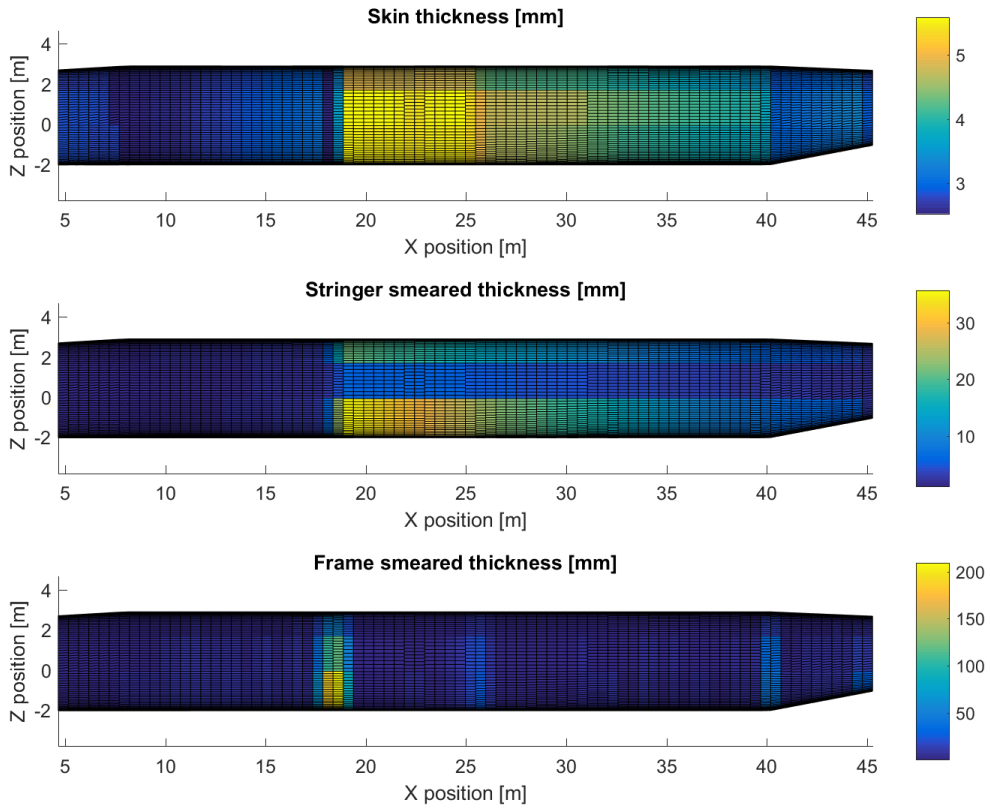

Figure 7.2: Composite Boeing 767-300ER thickness distribution

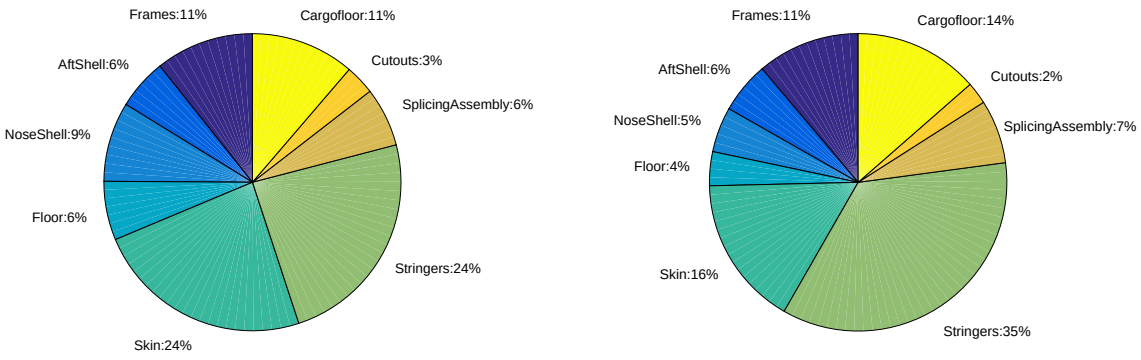

(a) Composite Airbus A320-200

(b) Composite Boeing 767-300ER

Figure 7.3: Weight breakdowns for composite fuselages

7.2. Oval Composite A320-200

Using the same dimensions as the conventional A320-200, but with a trapezoidal structure to obtain the oval cross-section and with composite material, the thickness distribution in Figure 7.4 is obtained. This distribution is almost identical to the one in Figure 7.1, except for that the skin thickness in the side arc is reduced, because the wall structure takes up some of the shear flow. The weight breakdown in Figure 7.5 is also almost identical to Figure 7.3a, but obviously a wall and ceiling are present. These are only slightly lighter than the passenger floor. Again the cargo floor forms a significant portion of the fuselage mass. The total fuselage mass was increased to 8,068 kg, which is a 3.6 % mass increase compared to the (conventional) composite fuselage.

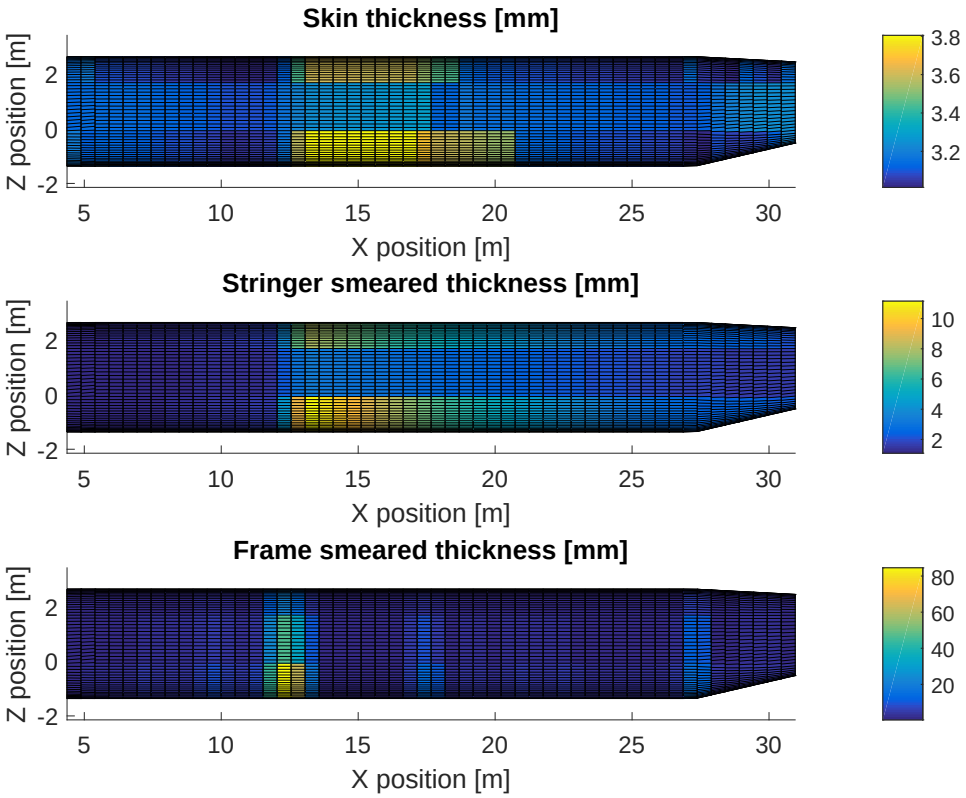

Figure 7.4: Oval, composite Airbus A320-200 thickness distribution

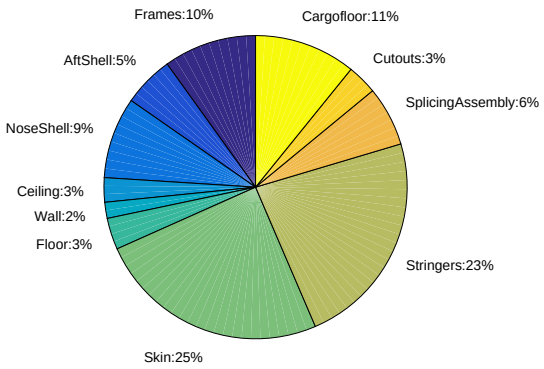

Figure 7.5: Oval, composite Airbus A320-200 weight breakdown

7.3. Wide Oval Boeing 767-300ER

By fitting in slightly more passengers, in a wider configuration and with the fuselage set to an oval configuration, an extra wide Boeing 767 was created. For this configuration, both aluminium and composite material were analysed consecutively and the results are presented and compared in this section.

As expected, the oval fuselage shows similar thickness distribution trends as the conventional fuselage. The composite fuselage in Figure 7.7 shows approximately identical skin thickness in the bottom and upper arc, while the side arc has a lower thickness. The latter is a result of the wall accounting for some of the shear flow. The upper and lower arc are probably mainly sized by pressure loads, which reduce the influence of shear flow. The stringer smeared thickness shows logical results and again the frame thickness is distributed just like in the conventional configurations.

The weight breakdown for the aluminium fuselage, see Figure 7.8a, shows that frames become a significant portion of the fuselage mass, being more than the skin and stringers together. Apparently, the oval shape induces large internal loads and moments in the frames. The weight breakdown for the composite fuselage in Figure 7.8b shows the same trend, albeit the frames contribute less to the total fuselage mass there. For both oval fuselages, the wall adds negligible weight and the ceiling contributes less than the floor.

The aluminium oval fuselage is estimated at 39,020 kg, while the empirical Torenbeek method estimates it at 18,189 kg. The empirical methods are unable to capture the deviating oval geometry and as such underestimate the fuselage mass.

For the composite oval fuselage a mass of 26,602 kg is estimated, which is less than the aluminium weight by 32 %.

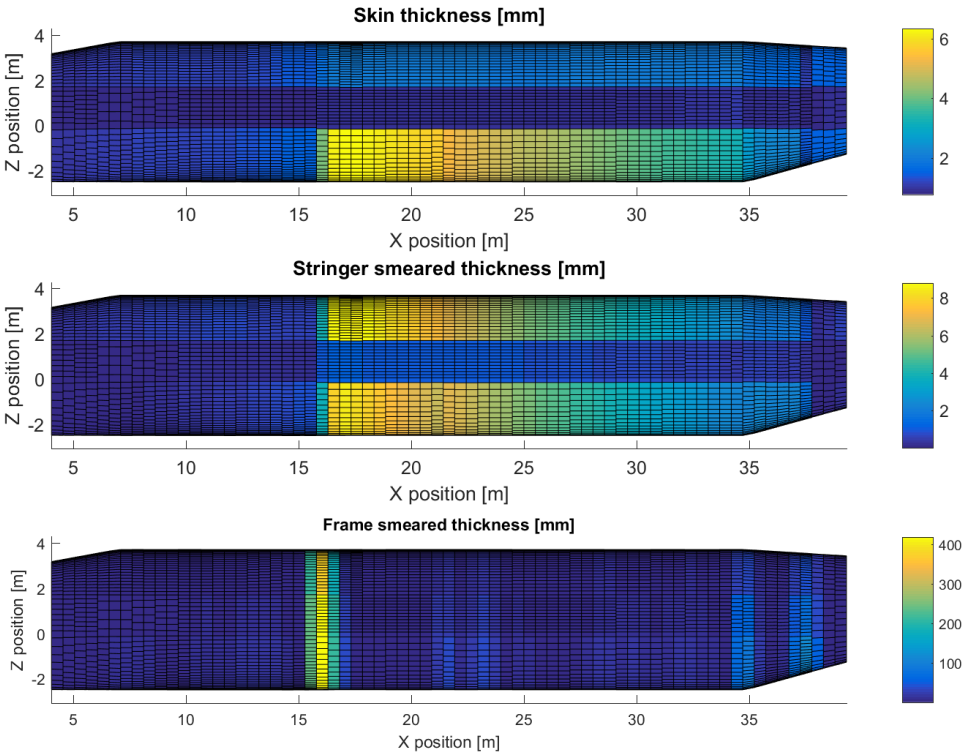

Figure 7.6: Oval, aluminium Boeing 767-300ER thickness distribution

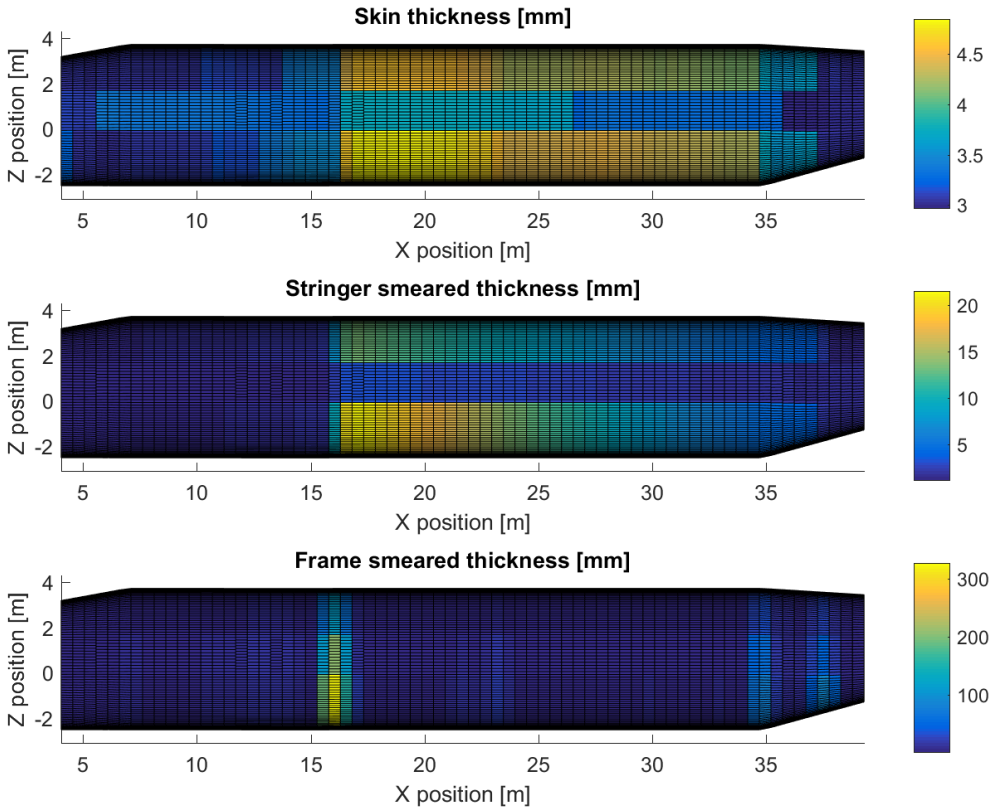

Figure 7.7: Oval, composite Boeing 767-300ER thickness distribution

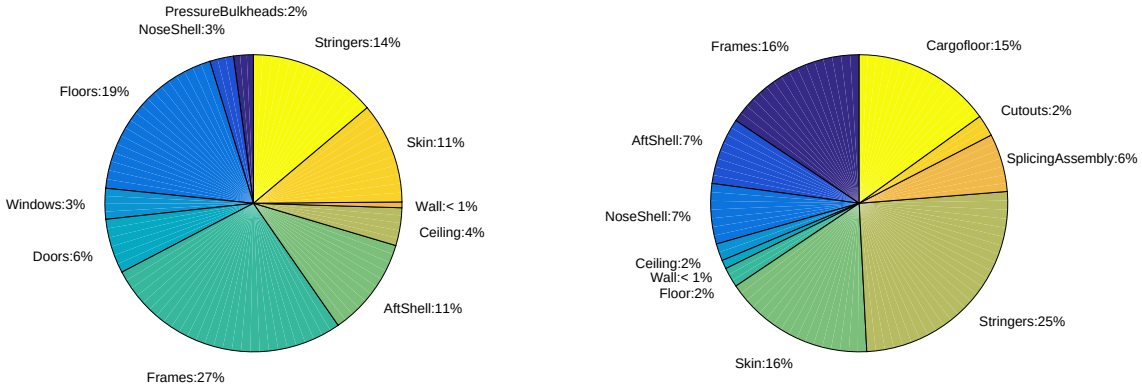

(a) Aluminium (b) Composite

Figure 7.8: Weight breakdowns for oval Boeing 767-300ER fuselages

7.4. Stiffened Trapezoid versus Sandwich Trapezoid

As a final case study, the composite, oval fuselages for the Airbus A320-200 and Boeing 767-300ER from the previous sections were taken. However, the ceiling and wall panels are now made as stiffened panels, instead of sandwich panels.

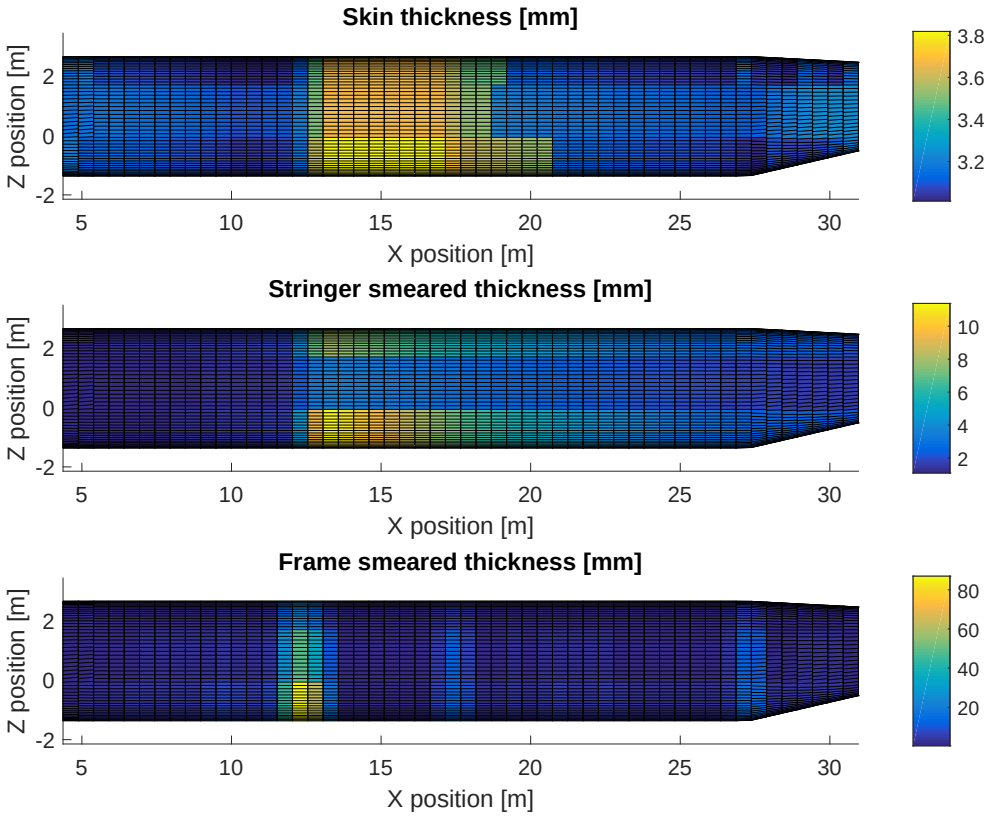

Figure 7.9: Stiffened trapezoid, oval Airbus A320-200 thickness distribution

Both Figure 7.9 and Figure 7.10 show that the stringer smeared thickness and frame smeared thickness distributions are unaffected by the transition to stiffened panels in the trapezoid (as compared to Figure 7.4 and Figure 7.7. However, the skin thickness is different along the side arc. The stiffened trapezoid wall carries less shear flow than the sandwich wall did, resulting in thicker side arc skins for the stiffened trapezoid concept. Additionally, the skins in the top and bottom arc are also thicker. Likely, the stiffened panels are thinner than the sandwich panels, reducing the section second moment of area, hence increasing direct stress due to bending.
Inspecting the weight breakdowns in Figure 7.11a and Figure 7.11b and comparing these to Figure 7.5 and Figure 7.8b, respectively, shows that the contributions to the total mass have not shifted significantly. On the other hand, the ceiling member does undergo a significant mass increase. The A320-200 fuselage mass is now estimated at 8,849 kg, which is 10 % more than its sandwich counterpart. The Boeing 767-300ER fuselage mass is now estimated at 28,146 kg, which is a weight increase of 5.8 % over its sandwich alternative. So having a stiffened trapezoid (excluding floor) definitely results in a heavier structure, but it is unclear as of yet this would be offset by the larger weight penalty involved with cutouts in sandwich panels (as opposed to cutouts in stiffened panels).

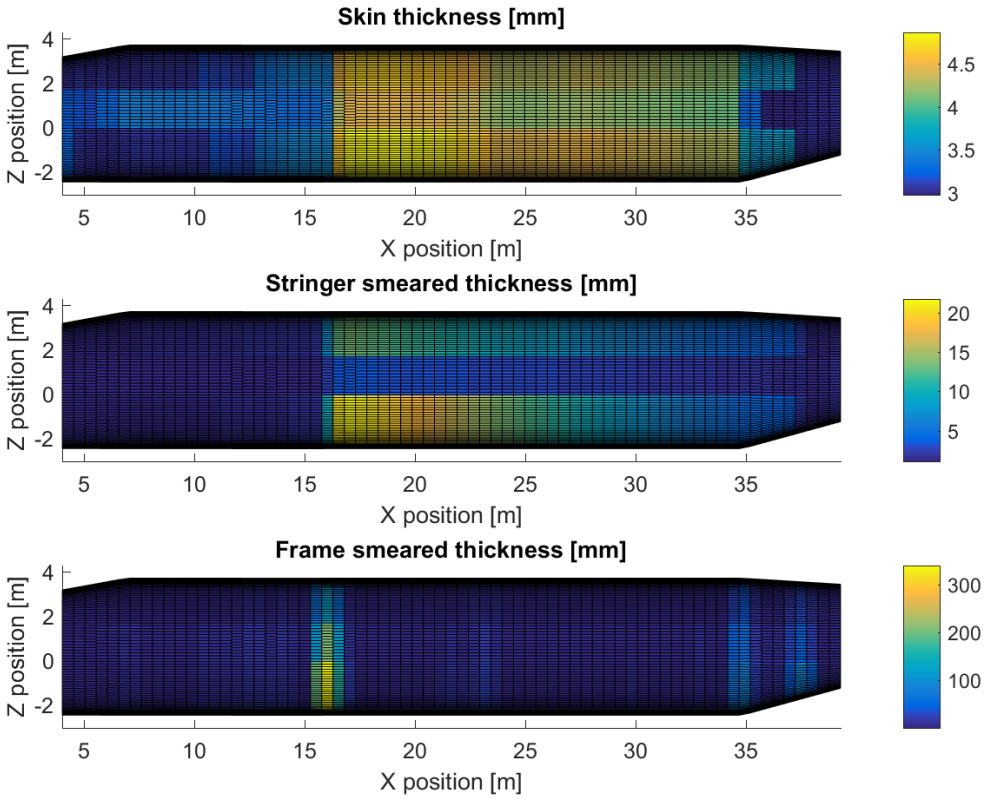

Figure 7.10: Stiffened trapezoid, oval Boeing 767-300ER thickness distribution

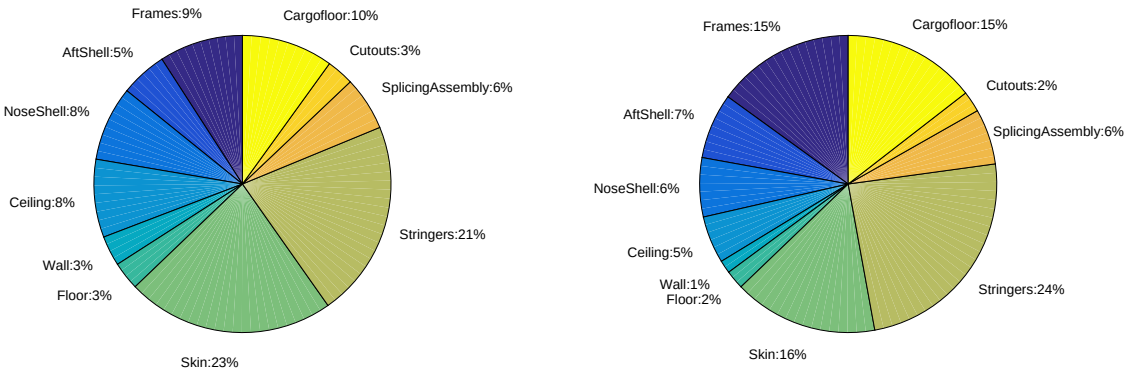

(a) Airbus A320-200 (b) Boeing 767-300ER

Figure 7.11: Weight breakdowns for oval composite fuselages with stiffened trapezoid

8

Conclusions and Recommendations

The goal for this thesis was to develop a semi-analytical weight estimation method for pressurized, composite, oval fuselages. This method was implemented into the FPP Initiator, written in Matlab. In doing so, the oval fuselage concept can be investigated in conceptual aircraft design of unconventional configurations, such as the blended wing body. These type of aircraft require a non-circular fuselage with an aerodynamic shape, for which the oval fuselage is one of few available concepts. With the help of this thesis work, composite oval fuselages may be investigated, following the current trend in aerospace industry towards composite materials.
The implemented approach was verified and validated on different aspects. It was concluded that the load cases and shear force and bending moment distributions may need revision. Pressurization loads in an oval fuselage section were compared to FEA results, and good agreement was obtained with errors less than one percent. Additionally, the implemented boom method showed good agreement with stresses predicted by FEA. It is therefore concluded that this method is implemented correctly and is able to satisfactorily predict internal stresses and shear flows.
Each composite panel is sized according to applied loads and the critical loads. Computation of these critical loads is therefore important and was compared to critical loads obtained from FEA. The findings are listed here:

- Shear buckling failure was found to be under-predicted by the implemented approach (i.e. the critical buckling load was overestimated) for panels with aspect ratio below 0.5. Scaling was used to compensate for this. For higher aspect ratios (up to 1), the opposite was found: a conservative shear buckling load was predicted.
- Deflection due to transverse pressure was compared with FEA and showed good agreement.
- Material failure due to tensile loads as predicted by the Tsai-Wu failure criterion seems to under-predict stresses as compared to FEA. Therefore, a non-conservative result is obtained. Investigation into different failure theories is in order.

Comparing the optimum found by the deterministic optimization approach outlined in section 3.5 with a genetic algorithm showed that the deterministic approach outperforms the GA for stringers, which is attributed to the brute-force approach adopted. For monolithic panels the GA performs better, which is attributed to the inherent inability of the deterministic approach to take into account all failure modes at once. Finally, sandwich panels were best designed by the deterministic approach, which produced lighter designs than the GA by a comfortable margin.
For aluminium fuselages, it was found that a similar fuselage mass fraction (i.e. the ratio of fuselage mass to MTOM) is predicted by the implemented approach as found in reality. Additionally, the weight breakdown is similar to a generic breakdown for passenger aircraft from literature. Inspection of thicknesses obtained from the implemented method shows satisfactory sizing of the primary structure. These observations were also made for composite and oval fuselage sizing. A weight saving of 10 to 20 % was obtained as compared to the aluminium counterparts. Oval fuselage sizing shows satisfactory results as well, but the cargo floor placement in the Initiator may need revision.

Concluding, the research question was answered and with that the thesis goal was attained. Methods similar to those used for conceptual sizing of conventional fuselages and materials may be used, but the effect of the oval geometry and varying stiffness of composite laminates has to be taken into account. Additionally, pressurization loads may be accurately predicted using the analytical solution for cylindrical cylinders when the oval cross-section does not change in the longitudinal direction. The sub-questions were answered in chapter 3, chapter 4 and chapter 5.

8.1. Recommendations

Several improvements can be made to the current method, and several recommendations for further research are presented in this section.

- In chapter 5 an attempt was made to find out the effect of the curvature of the oval fuselage pressure shell on the loads that form in this structure due to internal pressure. The finite difference method presented there can correctly approximate the hoop load, but the longitudinal load was probably incorrect. Due to time restrictions, no solution for this problem was found. However, by performing several FEA analyses of arbitrarily shaped pressure vessels and comparing these to the finite difference method might give more insight into what goes wrong. A working FD method can be implemented into the Initiator to better predict pressurization loads in the oval fuselage and therefore make the weight estimation more robust and accurate.
- The wing loads are introduced at one frame in the current method. However, for most aircraft, these loads are divided over two spars, so a better approximation may be obtained when the wing loads are introduced at two frames.
- So far, the oval fuselage concept has been studied in terms of its mass and in terms of feasibility concerning internal pressurization. However, crashworthiness is another important topic that dictates the feasibility of the fuselage concept. The crash structure might also induce a significant weight penalty and the oval shape of fuselage frames (if present at all) requires additional consideration. A possibility could be to employ frames that only span the bottom arc of the fuselage and support a transverse beam that in turn supports the passenger floor. Struts may be used for additional energy absorption. The trapezoidal structure should then carry the remaining loads.
- The load cases used in the current method might be incomplete, and a more detailed and complete set of load cases is advisable.
- Instead of the Tsai-Wu failure criterion, which is only accurate for single plies, the Puck criterion may be used. The Puck criterion is a physically based model, that does not rely on linear stress-strain relationships and accounts for multiple failure modes, either fiber failure (FF), or inter fiber failure (IFF) [28–31]. Moreover, the Puck criterion is the most widely accepted in aerospace industry [29], because disadvantages of both interactive and non-interactive failure theories are avoided; a distinction is made between fiber and matrix failure modes; non-linear stress and strain analysis is relied on; and it includes physically based action plane related fracture criteria [32]. It is therefore recommended to use this criterion instead.
- Modeling of a keel beam and the area around the wing-box carry-through structure may improve the weight estimation. Additionally, bulkheads should be sized using an analytical approach, since their weight seems to be underestimated in the current method.
- The presented frame analysis method does, apart from the shape, not take into account the trapezoidal structure. At the junctions with the trapezoidal members, forces have to be introduced in the frame that represent the trapezoid members. It is expected that these will reduce the loads in the frame, because the alleviate the internal bending moment.
- The boom method as implemented is valid for a single-cell cross-section, which is certainly not the case for the oval fuselage. Therefore, it should be extended by implementing the multi-cell theory.

A

Operation Manual

This manual explains how to perform several aspects of the weight estimation method outlined in this thesis. The first section discusses how to run the Initiator and get the fuselage weight results. Secondly, a description of how to run a new DOE for each type of composite member is provided, where it is also explained how to modify the used material. The third section continues by elaborating upon how to generate new surrogate models (using the newly created DOE results). Finally, the fourth section is a short explanation of the finite difference method presented in chapter 5.

A.1. Initiator

The Initiator is a Matlab program which can be obtained by using TortoiseSVN (or another SVN tool) and performing a checkout on the correct trunk. The details of these operations are not discussed here, since the URLs might change and working with SVN is beyond the scope of this thesis. Obviously, an installation of Matlab is also required. The version depends on new functionality added to the Initiator, but at the time of writing version 2015b or higher is recommended.

In Matlab, browse to the main folder of the Initiator. In the `CleanInputFiles` folder one finds .xml files containing settings specific to certain aircraft. Copy either an aircraft file and its corresponding settings file to the main folder, or type `restore` in the command window and press Enter. Now type `Initiator --interactive` in the command window, press *Enter*, then type the name of the aircraft for which to run the weight estimation and press *Enter* again. After the aircraft settings have been loaded, type `run FuselageWeightEstimation` and press *Enter*. The Initiator will now perform all tasks in order for it to run the fuselage weight estimation and then perform the weight estimation method. It terminates by displaying the resulting fuselage mass along with the empirical masses from Torenbeek, Raymer, Howe and Nicolai. Moreover, several plots have been displayed (if not, the Matlab property *DefaultFigureVisible* is set to 0). All results have been written to the aircraft file, so to examine the exact data one should look there.

A.2. Design of Experiments

The `CompositeDOE` folder contains all files needed to perform the design of experiments for panels, stringers and sandwich panels. The somewhat cumbersome process of modifying material properties is explained next. After that, an explanation of how to run the DOE follows.

For monolithic plates, locate the `optimizePlate.m` file in the `@Plates` folder. In there, there is a line

```
plate.mat = [137.9e9 11.7e9 4.82e9 0.29 0.1524e–3 1609];
```

which denotes the material properties E_x, E_y, G_{xy}, ν_{xy}, t_{ply} and ρ in the same units as Table 4.2. For the material strengths and other properties, locate the `createOptWorkspace_plate.m` in the same folder. Modify the necessary parameters and run this file from the command window. It will save a file to the `Opt_Settings` folder. Don't modify that filename.

For sandwich panels, modifying the material for the facesheets is identical to the procedure for monolithic panels, but now the code is located in `optimizeSandwich.m` and `createOptWorkspace_sandwich.m`,

respectively. To modify the core material, locate the `GenerateSandwichDatabase.m` file in the root folder. There are a few lines defining the core:

```
core.E = 131*10^6; % Pa
core.Gxz = 41.4*10^6; % Pa
core.Gyz = 20.7*10^6; % Pa
core.rho = 48.2; % kg/m^3
```

Finally, for the stringers, locate `createOptWorkspace_v2.m` in the `@Stringers` folder and modify the required properties. Also modify the line

```
mat = [137.9e9 11.7e9 4.82e9 0.29 0.1524e-3 1609];
```

in the `GenerateStringerDatabase.m` file, located in the root folder.
In the root folder, the three files `GenerateSandwichDatabase.m`, `GenerateStringerDatabase.m` and `GeneratePanelDatabase.m` will perform the design of experiments. Simply run the script and all necessary actions will be performed. Please note that depending on the amount of experiments and the computer used it may take several hours to days for it to complete! Moreover, the experiments will be run in a parallel pool, so much of the computer's resources will be used. It is therefore advised to either run the scripts on a computer that is not needed for other tasks, or change the `parfor` loops to normal `for` loops.
In each of the three files mentioned earlier, one finds the following two lines:

```
num = 30000;
x = lhsdesign(num,5);
```

This generates a matrix with 30,000 rows (the experiments) and 5 columns, with values ranging from 0 to 1. This is the Latin Hypercube Sampling. The amount of columns reflects the parameters used to specify the component dimensions and loads and does not need to be changed. However, the `num` variable may be set to any number preferred.
Since the sampling only returns numbers from 0 to 1, these need to be scaled to meaningful values. The variable `preds` does that:

```
preds = [0.3 0.12 0 0 0; ...
    0.8 0.8 2000 100 500];
```

The comments indicate which number is for which parameter, but the first row always is the minimum value and the second and last row the maximum. For dimensions meters are used as unit, for loads it's in either kN/m or kPa.
The last thing one may want to change is the filename where the results are written to. The last line in each *Generate* file can be modified:

```
save('plate_database', 'plateArray', 'plate_data', 'x', 'preds');
```

Change the first string in the `save` command to change the filename. The extension .mat does not have to be included.

A.3. Creating Surrogate Models

The surrogate models can be easily created by running the scripts located in the `ModelGeneration` folder. The main three files are:

1. `Plate_forecasting.m`
2. `Sandwich_forecasting.m`
3. `Stringer_forecasting.m`

However, before these files can use the newly created DOE data, copy the files created by the DOE into the current (`ModelGeneration`) folder. Then locate the *CreateExcel* scripts:

1. `CreateExcelPlate.m`
2. `CreateExcelSandwich2.m`

3. `CreateExcelStringer.m`

In each of these files the following two lines may be modified:

```
load('plate_database_final');
filename = 'plate_final_nondim.xlsx';
```

The first loads the DOE data, so make sure to edit this string to refer to the correct file. The second line defines the filename where the Excel file will be written to. It does not necessarily have to be changed; it will overwrite the current file if it wasn't. Otherwise, make sure to also edit the filename in the *forecasting* files in a line similar to:

```
ds = dataset('xlsfile', 'sandwich_data_nondim.xlsx');
```

With the Excel files created, the *forecasting* scripts can be executed without further editing. Each will create a collection of neural networks and linear regression models for the parameters of interest for each type of component. Additionally, new files are created that contain the neural networks for use in the Initiator. Copy these files (`plate_model.mat`, `stringer_model.mat` and `sandwich_model.mat`) to the `Opt_Settings` folder in the Initiator folder (and replace the existing ones, or better yet: rename those and copy the new files afterwards). If this operation needs to be performed multiple times, it may be advantageous to create a function and a setting in the Initiator that will load the correct neural networks depending on the new material setting. Then each file put in the `Opt_Settings` folder needs a unique name.

B

Explanation of Messages

The weight estimation method and member sizing methods may output some messages to the Matlab Command Window during runtime. A list of messages for each of these methods is provides below, accompanied by a description of what they mean and what the user should do.

B.1. Fuselage Weight Estimation

FuselageWeightEstimation assumes first cabin to be main cabin, i.e. this cabin lies on the floor of the trapezoid structure and its height is the trapezoid height The FWE always starts with this message and the user does not have to do anything with this, except for checking whether the cabins have been correctly declared in the aircraft settings file as stated by this message.

Warning: Discrepancy between fuel tank mass and total fuel mass of xxx kg This warning is common and means that the fuel mass that can geometrically fit in the fuel tanks is not equal to the fuel mass required for the harmonic mission. No action need be undertaken, since this message is only meant for informative purposes.

Scaling fuel tank mass with ratio of geometric fuel volume and total fuel mass Follow-up message of the previous message, again for information, meaning that the method assumes that all tanks are only filled up to the amount required for the harmonic mission.

Fuselage weight estimation scaling pax, cargo and fuel masses to match previous weight results Again a message only for informative purposes. What happens is that the amount of passengers, cargo and/or fuel is not equal to the amounts as specified for the harmonic mission. In this case the FWE scales these masses such that agreement is obtained.

Iteration x, Max Abs Deviation: xxx
Iteration x, Amount of deviating variables: xxx The iterative process of estimating the structural thicknesses is busy and provides the user with this information each iteration. The maximum absolute deviation of the design variables is shown, which gives an idea of how close to converging the method is. Additionally, the amount of variables that have a deviation larger than the tolerance from their previous value is provided.

Too large/small input value for stringer! Only for composite sizing this message may appear. When either a stringer dimension or load is provided to the neural network that is not within the limits of values used to generate the neural network, this message appears. It may or may not be a cause for errors in the weight estimation. A new neural network may be made which includes the out-of-bound values to solve this issue.

Too large/small input value for panel! Only for composite sizing this message may appear. When either a panel dimension or load is provided to the neural network that is not within the limits of values used to generate the neural network, this message appears. It may or may not be a cause for errors in the weight estimation. A new neural network may be made which includes the out-of-bound values to solve this issue.

Too large/small input value for sandwich! Only for composite sizing this message may appear. When either a sandwich panel dimension or load is provided to the neural network that is not within the limits of values used to generate the neural network, this message appears. It may or may not be a cause for errors in the weight estimation. A new neural network may be made which includes the out-of-bound values to solve this issue.

B.2. Panel Database Generation

Total time to complete p(i=xx/xx): xxx s Appears after each completed panel, giving the user an indication of how long it takes to size one panel. Since the loop is executed in parallel, the index/total indication is not in any particular order, so no conclusion may be drawn on the total completion of the database generation.

Axial loads can not be compressive (unless buckling calculation is adapted) This error message appears when a negative axial load is specified (i.e. N_x or N_y). Currently, the method only supports tension in these directions, and as stated, the buckling calculation should be modified when compression forces are required.

Warning no convergence in strength determination The Newton-Raphson method has not converged within a set amount of iterations, such that the critical loads computed are likely incorrect. When this happens, there is likely a bug leading to incorrect input for the `StrengthDetermination` function.

Execution stopped because initial laminate does not meet requirements Each ply addition function can produce this message, but it only appears when the initial laminate specified is invalid (according to the laminate stacking rules) or when there is a bug in the program.

For some reason a ply could not be added to the laminate Most of the ply addition functions can produce this message, meaning they failed in adding a ply to the laminate without violating the stacking sequence constraints. In general this should never happen, but if it does, a good first solution is to check the process selecting a ply addition function based on the most critical failure load.

B.3. Stringer Database Generation

Optimization routine finished... Warning! No optimum subdesigns could be found Because a given number of laminates is generated beforehand and all combinations are analyzed, it may happen that none can cope with the applied loads within the dimension bounds. Either increase `nogen` to increase the amount of laminates or increase `maxgendiff` to allow more difference in number of plies per member. Note that both these options increase computational time. As a final option, decrease the maximum loads for which to generate the database.

Warning no convergence in strength determination The Newton-Raphson method has not converged within a set amount of iterations, such that the critical loads computed are likely incorrect. When this happens, there is likely a bug leading to incorrect input for the `StrengthDetermination` function.

B.4. Sandwich Database Generation

The same or similar messages may occur as for the monolithic panels. Therefore, they are not repeated here.

C

Fuselage Weight Estimation Settings

FWESkinMaterial Set a material tag for the material to be used for skin sizing and failure analysis. Generally, `al2024t3` is set for conventional, aluminium aircraft. Set to `cfrp` to use fiber composite material.

FWEFrameMaterial Set a material tag for the material to be used for skin sizing and failure analysis. Generally, `al7075t6` is set for conventional, aluminium aircraft. Set to `cfrp` to use fiber composite material.

FWEFacingMaterial Set a material tag for the material to be used for skin sizing and failure analysis. Generally, `al2024t3` is set for conventional, aluminium aircraft. Set to `cfrp` to use fiber composite material.

FWECoreMaterial Set a material tag for the material to be used for skin sizing and failure analysis. For conventional, aluminium aircraft the value `honeycomb` is used, generally. For a composite fuselage, this setting is not used.

FWECargoFloorMaterial Set a material tag for the material to be used for skin sizing and failure analysis. Generally, `al2024t3` is set for conventional, aluminium aircraft. Set to `cfrp` to use fiber composite material.

FWEMinimumGageThickness Set the minimum thickness for metal components in m.

FWEPaxTransverseLoad An empirical estimate of the load passenger exert on the floor in Pa. Is by default set to 17 kPa.

FWECargoTransverseLoad An empirical estimate of the load cargo exerts on the cargo floor in Pa.

FWEBurstPressureSafetyFactor Safety factor for burst pressure load case.

FWEUseCabinAltitude Set to `true` to use a specified cabin altitude. Otherwise, the maximum differential pressure is used.

FWEMinimumCabinAltitude The minimum cabin altitude in m.

FWEMaximumCabinDifferentialPressure Maximum cabin differential pressure in psi. Used when a cabin altitude is not specified.

FWEMinimumCabinDifferentialPressure Minimum cabin differential pressure in psi. Used in burst and landing load cases.

FWELandingLoadFactor Load factor applied in landing load cases.

FWELandingGearLoadFraction Fraction of aircraft weight carried by landing gear during landing.

FWEStiffenerType Stiffener type for metal sizing. Available options: `z`, `hat`, `z-simple` and `z-simple-optim`.

PanelTypeFloor Optional setting. Only used for composite sizing. Set by default to `sandwich`, however, can be set to `stiffened`. Models the trapezoid floor either as a sandwich beam or as stiffened panels with cross-beams.

PanelTypeWall Optional setting. Only used for composite sizing. Set by default to `sandwich`, however, can be set to `stiffened`. Models the trapezoid wall either as a sandwich beam or as stiffened panels with cross-beams.

PanelTypeCeiling Optional setting. Only used for composite sizing. Set by default to `sandwich`, however, can be set to `stiffened`. Models the trapezoid ceiling either as a sandwich beam or as stiffened panels with cross-beams.

Bibliography

[1] R. H. Liebeck. Design of the blended wing body subsonic transport. *Journal of Aircraft*, 41(1):10–25, 2004.

[2] V. Mukhopadhyay. Structural concepts study of non-circular fuselage configurations. In *SAE/AIAA World Aviation Congress*, pages 1–13. AIAA, 1996.

[3] V. Mukhopadhyay, J. Sobieszczanski-Sobieski, I. Kosaka, G. Quinn, and G. N. Vanderpaats. Analysis, design, and optimization of noncylindrical fuselage for blended-wing-body vehicle. *Journal of Aircraft*, 41(4):925–930, 2004.

[4] V. Mukhopadhyay. Blended-wing-body fuselage structural design for weight reduction. In *46th Structures, Structural Dynamics and Materials Conference*, number April, pages 1–8. AIAA, 2005.

[5] V. Mukhopadhyay and M. R. Sorokach. Composite structure modeling and analysis of advanced aircraft fuselage concepts. In *AIAA Modeling and Simulation Technologies Conference*, number June, pages 1–14. AIAA, 2015.

[6] F. J. J. M. M. Geuskens, O. K. Bergsma, S. Koussios, and A. Beukers. Analysis of conformable pressure vessels: Introducing the multi-bubble. *AIAA Journal*, 49(8):1683–1692, 2011.

[7] V. Mukhopadhyay. Hybrid-wing-body vehicle composite fuselage analysis and case study. In *14th AIAA Aviation Technology, Integration and Operations Conference*, pages 1–12. AIAA, 2014.

[8] V. Mukhopadhyay. Hybrid wing-body pressurized fuselage modeling, analysis, and design for weight reduction. In *53rd AIAA/ASME/ASCE/AHS/ASC Structures, Structural Dynamics and Materials Conference*, number April, pages 1–14. AIAA, 2012.

[9] R. Vos and M.F.M. Hoogreef. Semi-analytical weight estimation method for fuselages with oval cross-section. In *54th AIAA/ASME/ASCE/AHS/ASC Structures, Structural Dynamics, and Materials Conference*, pages 1–15. AIAA, 2013.

[10] K. Schmidt and R. Vos. A semi-analytical weight estimation method for oval fuselages in conventional and novel aircraft. In *52nd Aerospace Sciences Meeting*, number January, pages 1–20. AIAA, 2014.

[11] S. de Smedt and R. Vos. Knowledge-based engineering approach to the finite element analysis of the oval fuselage concept. In *53rd AIAA Aerospace Sciences Meeting*, number January, pages 1–15. AIAA, 2015.

[12] R. Marissen. Two main challenges for the future composites technology, costs reduction and strength prediction. In *Tenth European Conference on Composite Materials*, pages 1–11, 2002.

[13] M. J. L. van Tooren. *Sandwich Fuselage Design*. PhD thesis, Delft University of Technology, 1998.

[14] J. Roskam. *Airplane Design Part V: Component Weight Estimation*. Darcorporation, 1985.

[15] Anon. Certification specifications for large aeroplanes. Technical Report September, EASA, 2007.

[16] T.H.G. Megson. *Aircraft Structures*. Elsevier, 4th edition, 2007.

[17] D. Howe. Blended wing body airframe mass prediction. *Journal of Aerospace Engineering*, 215(June):319–331, 2001.

[18] D.R. Polland, S.R. Finn, K.H. Griess, J.L. Hafenrichter, C.T. Hanson, L.B. Ilcewicz, S.L. Metschan, D.B. Scholz, and P.J. Smith. Global cost and weight evaluation of fuselage side panel design concepts. Technical report, NASA, 1997.

[19] B.W. Flynn, M.R. Morris, S.L. Metschan, G.D. Swanson, P.J. Smith, K.H. Griess, M.R. Schramm, and R.J. Humphrey. Global cost and weight evaluation of fuselage keel design concepts. Technical report, Boeing Commercial Airplane Group, 1997.

[20] R. Jones. *Mechanics of Composite Materials*. Taylor and Francis, 2nd edition, 1999.

[21] C. Kassapoglou. *Design and Analysis of Composite Structures: With Applications to Aerospace Structures*. Wiley, 2nd edition, 2013.

[22] I. van Gent and C. Kassapoglou. Cost-weight trades for modular composite structures. *Structural and Multidisciplinary Optimization*, 2013.

[23] E.F. Bruhn. *Analysis and Design of Flight Vehicle Structures*. Tri-State Offset Company, 1973.

[24] D. Ambur and M. Rouse. Design and evaluation of composite fuselage panels subjected to combined loading conditions. *Journal of Aircraft*, 42(4):1037–1045, 2005.

[25] W. Flügge. *Stresses in Shells*. Springer-Verlag, Berlin, 3rd edition, 1966.

[26] R. W. Johnson, L. W. Thomson, and R. D. Wilson. Study on utilization of advanced composites in fuselage structures of large transports. Technical report, NASA, 1985.

[27] E. Torenbeek. *Synthesis of Subsonic Airplane Design*. Delft University Press, Delft, 1982.

[28] A. Puck and H. M. Deuschle. Progress in the puck failure theory for fibre reinforced composites : Analytical solutions for 3d-stress. *Composites Science and Technology*, 62(3):371–378, 2002.

[29] G. Lutz. The puck theory of failure in laminates in the context of the new guideline vdi 2014 part 3. Technical report, VDI, 2014.

[30] M Knops. *Analysis of Failure in Fiber Polymer Laminates*, volume 0. Springer, 2008.

[31] H. M. Deuschle and A. Puck. Application of the puck failure theory for fibre-reinforced composites under three-dimensional stress: Comparison with experimental results. *Journal of Composite Materials*, 47(6-7):827–846, 2013.

[32] N. Kosmas. *Predicting Onset of Damage in Special Class of Laminates under Tension*. Master, Delft University of Technology, 2015.